

**LATERAL ORGANIZATION AND THERMODYNAMICS OF
COILED-COIL LIPOPEPTIDES
– IMPLICATIONS FOR DOCKING AND FUSION EFFICIENCY**

DISSERTATION

zur Erlangung des mathematisch-naturwissenschaftlichen Doktorgrades

„Doctor rerum naturalium“

der Georg-August-Universität Göttingen

im Promotionsprogramm Chemie

der Georg-August University School of Science (GAUSS)

vorgelegt von

Gesa Pähler

geboren in Berlin

Göttingen, 2012

Betreuungsausschuss

Prof. Dr. Andreas Janshoff
Institut für Physikalische Chemie, Georg-August-Universität Göttingen

Prof. Dr. Ulf Diederichsen
Institut für Organische und Biomolekulare Chemie, Georg-August-Universität Göttingen

Mitglieder der Prüfungskommission

Referent: Prof. Dr. Andreas Janshoff
Institut für Physikalische Chemie, Georg-August-Universität Göttingen

Korreferent: Prof. Dr. Ulf Diederichsen
Institut für Organische und Biomolekulare Chemie, Georg-August-Universität
Göttingen

Weitere Mitglieder der Prüfungskommission

Prof. Dr. Marina Bennati
Max-Planck-Institut für Biophysikalische Chemie

Prof. Dr. Burkhard Geil
Institut für Physikalische Chemie, Georg-August-Universität Göttingen

Prof. Dr. Kai Tittmann
Bioanalytik, Albrecht-von-Haller-Institut für Pflanzenwissenschaften

Prof. Dr. Mikael Simons
Cellular Neuroscience, Max-Planck-Institut für Experimentelle Medizin

Tag der mündlichen Prüfung: 07. November 2012

für Papa

„Es ist ein großer Vorteil im Leben,
die Fehler, aus denen man lernen kann,
möglichst früh zu begehen.“

Winston Churchill

Abstract

Specific cellular membrane interaction is a crucial point in nature as it facilitates key processes like cell-cell communication or membrane fusion. The latter one is highly controlled frequently mediated by the superfamily of SNARE proteins (soluble N-ethylmaleimide-sensitive factor attachment protein receptor) in eukaryotic cells. The definite mechanism behind this process is still poorly understood, but the coiled-coil formation of the SNARE core complex consisting of four α -helices seems to generate the fusogenic driving force. This offers the possibility to design a straightforward experimental setup to mimic the complex protein-mediated membrane-membrane interaction by using mere protein fragments or peptides attached to artificial lipid bilayers, which self-assemble into a coiled-coil structure.

In this work, three different sets of artificial coiled-coil forming peptides were synthesized and subsequently attached to maleimide containing phospholipids in membranes via an *in situ* coupling reaction generating a highly controllable functionalization protocol. Thus, secondary structure changes, kinetics as well as thermodynamic characteristics were monitored during coiled-coil formation in solution and on solid supported membranes with *e.g.* time-resolved ellipsometry, IR and CD spectroscopy. A distinct loss of entropy upon heterodimerization of peptides on surfaces was found. This could be correlated with a self-assembled lateral clustering of lipopeptides in membranes leading to translational immobilization of hybrid structures. Strikingly, these dense and highly ordered clusters, which act as obstacles for surrounding matrix lipids, undergo a slow but detectable reorganization process causing a partial dissolution of the found clusters upon coiled-coil formation. Furthermore, an increasing fusogenicity was shown, which was correlated to the degree of cluster formation.

Upon focusing on energetic and as well structural characteristics, the established model system gives the possibility to screen the docking and fusion ability of different coiled-coil forming peptides leading to an ideal mimic for SNARE mediated membrane fusion.

Zusammenfassung

Spezifische Zellmembran-Wechselwirkungen sind äußerst wichtig in lebenden Organismen, da hierdurch Schlüsselprozesse wie Zell-Zell-Kommunikation oder Membranfusion ermöglicht werden. Letzterer ist ein in hohem Maße kontrollierter Prozess, der in eukaryotischen Zellen häufig durch die Superfamilie der SNARE (engl. *soluble N-ethylmaleimide-sensitive factor attachment protein receptor*) Proteine vermittelt wird. Der Mechanismus hinter diesem Prozess ist bis heute nicht vollständig aufgeklärt. Jedoch kann davon ausgegangen werden, dass die Superhelixbildung (*coiled-coil* Struktur) des SNARE-Kernkomplexes, bestehend aus vier α -Helices, die fusogene Triebkraft generiert. Dies bietet die Möglichkeit eines einfachen experimentellen Zugangs, welcher die komplexe proteinvermittelte Membran-Membran Wechselwirkung nachstellt, indem ausschließlich Proteinfragmente oder Peptide an artifizielle Lipiddoppelschichten gebunden werden, welche ihrerseits eine *coiled-coil* Struktur ausbilden.

In dieser Arbeit wurden drei verschiedene Paare dieser superhelixbildenden Peptide synthetisiert und mittels einer *in situ* Kopplungsreaktion an maleimidhaltige Phospholipide in synthetischen Membranen verankert. Anschließend wurden Sekundärstrukturänderungen, kinetische und auch thermodynamische Eigenschaften während der *coiled-coil* Ausbildung sowohl in Lösung als auch an Lipidmembranen untersucht. Hierfür wurden etwa zeitaufgelöste Ellipsometrie, IR und CD Spektroskopie verwendet. Hierbei konnte ein deutlicher Verlust an Entropie während der Peptid-Heterodimerisierung auf Oberflächen gefunden werden, welcher mit einer lateralen Strukturierung, einer *Cluster*-Bildung, der Lipopeptide in der Membran in Zusammenhang gebracht werden konnte. Diese *Cluster*-Bildung führt zu einer translationalen Immobilisierung der hybriden Strukturen. Auffallend ist, dass die dichten und hochgeordneten *Cluster*, welche als Hindernis bezüglich der Mobilität der umgebenden Lipide wirken, einen langsamen Reorganisationsprozess durchlaufen, was in einer partiellen Auflösung der Strukturen durch die *coiled-coil* Bildung resultiert. Zusätzlich konnte eine verstärkte Fusogenität der Peptide gezeigt werden, welcher in Zusammenhang mit dem Grad der *Cluster*-Bildung steht.

Durch das Konzentrieren auf sowohl energetische als auch strukturelle Eigenschaften bietet das hergestellte Modellsystem die Möglichkeit verschiedene superhelixbildende Peptide hinsichtlich ihrer Fusogenität zu vergleichen, um die SNARE-vermittelte Membranfusion detailgetreu nachzuahmen.

List of Content

I	Introduction	1
I.1	Membrane-Membrane Interaction and Fusion	1
I.2	Coiled-coil Proteins as Motors for Membrane Fusion	3
I.3	Model Systems for Membrane Fusion in Biophysical Chemistry.....	5
II	Motivation - Establishing a Model System.....	7
III	Materials and Experimentals	9
III.1	Artificial Membranes Formed by Phospholipids.....	9
III.1.1	Phospholipids and their Phase Behavior.....	9
III.1.2	Chemically Modified Lipids	12
III.1.2.1	Maleimide Functionalized Lipids.....	12
III.1.2.2	Fluorescently Labeled Lipids	12
III.1.2.3	Cholesterol.....	13
III.1.3	Vesicle Preparation and Bilayer Formation	14
III.2	Coiled-coil Forming Peptides	15
III.2.1	Theory of Coiled-coil Formation	15
III.2.2	Solid Phase Peptide Synthesis.....	17
III.2.3	Purification of Peptides via RP-HPLC.....	21
III.2.4	Handling and storage of peptides	24
III.3	Lipopeptide Formation via <i>in situ</i> Coupling Reaction	24
III.3.1	Theory of Lipopeptide Formation	24
III.3.2	Experimental Procedures and Removal of Excess Peptide	26
III.3.2.1	Functionalization of Solid Supported Membranes	26
III.3.2.2	Functionalization of Vesicles.....	26

III.4	Further Materials.....	28
III.4.1	Fluorophores	28
III.4.1.1	Sulforhodamine B	28
III.4.1.2	Oregon Green 488 Maleimide	28
III.4.2	Buffers	29
IV	Instrumentation and Data Analysis	31
IV.1	Fourier Transform Infrared Spectroscopy (FT IR)	31
IV.1.1	Transmission and Attenuated Total Reflection FT IR Spectroscopy.....	31
IV.1.2	Analysis of Protein and Lipid Spectra	33
IV.1.3	Experimental Procedures	35
IV.1.3.1	Transmission FT IR Spectroscopy	35
IV.1.3.2	ATR-FT IR Spectroscopy	35
IV.2	Absorbance Spectroscopy with Ultraviolet and Visual Light.....	35
IV.2.1	Theory of UV/Vis and CD Spectroscopy	36
IV.2.2	Data Analysis	37
IV.2.2.1	UV/Vis Spectroscopy	37
IV.2.2.2	CD Spectroscopy.....	38
IV.2.3	Experimental Procedures	40
IV.2.3.1	UV/Vis Spectroscopy	40
IV.2.3.2	CD Spectroscopy.....	40
IV.3	Surface Plasmon Resonance Spectroscopy	40
IV.3.1	Theory.....	40
IV.3.2.	Data Analysis	42
III.3.3	Experimental Procedure	43
IV.4	Ellipsometry.....	44
IV.4.1	Theory, Setup and Analytical Workup.....	44
IV.4.2	Adsorption Isotherms.....	46

LIST OF CONTENT

IV.4.3	Experimental Procedures and Analysis.....	47
IV.5	Atomic Force Microscopy	48
IV.5.1	Theory of Imaging with Atomic Force Microscopy	48
IV.5.2	Experimental Procedures.....	49
IV.6	Fluorescence Recovery After Photobleaching	49
IV.6.1	Basic Principles and Data Analysis	50
IV.6.2	Mathematical Descriptions in FRAP Data Analysis	51
IV.6.3	Experimental Procedures.....	52
IV.7	Fusion Assays Based On Fluorescence Spectroscopy	53
IV.7.1	Dequenching Assays for Detection of Fusion	53
IV.7.1.1	Lipid Mixing Assay	55
IV.7.1.2	Content Mixing Assay.....	56
IV.7.2	Experimental Procedures.....	56
IV.7.2.1	Texas Red Self-Quenching Lipid Mixing	57
IV.7.2.2	Sulforhodamin B Content Mixing.....	57
V	Structural Analysis of Model System	59
V.1	Introduction	59
V.2	Secondary Structure Before and After Heterodimerization	60
V.2.1	Parallel Coiled-coil Formation.....	61
V.2.2	Antiparallel Coiled-coil Formation	64
V.3	Structural Analyses After <i>in situ</i> Coupling to a Lipid Bilayer	65
V.3.1	Membrane Thickness in Dependence of Cholesterol	65
V.3.2	Membrane Functionalization by <i>in situ</i> Coupling Reactions.....	67
V.3.2.1	Kinetic Analyses of Membrane Functionalization.....	67
V.3.2.2	Secondary Structure of Peptide Heterodimers on SSM.....	71
V.3.2.3	Specificity and Quantification of Lipopeptide Formation.....	75
V.4	Discussion.....	78

VI	Thermodynamics of Parallel and Antiparallel Coiled-coil Formation on Lipid Bilayers.....	79
VI.1	Introduction.....	79
VI.2	Thermodynamics of Pure Peptides in Solution and on Hydrogels	80
VI.3	Thermodynamics on Solid Supported Membranes.....	84
VI.3.1	Adsorption Isotherms.....	84
VI.3.2	Loss of Entropy	87
VI.4	Fusogenicity of Parallel and Antiparallel Coiled-coil Complexes.....	89
VI.5	Discussion	91
VII	Lateral Organization of Lipopeptides and the Impact on Heterodimerization	93
VII.1	Introduction.....	93
VII.2	Lateral Self-assembly of Lipopeptides in Solid Supported Membranes.....	94
VII.2.1	Lateral Mobility of Functionalized Membranes	95
VII.2.2	Quantification of Peptide Clusters by High Resolution Imaging	99
VII.3	Impact of Lipopeptide Clustering on Unbinding Forces	106
VII.4	Discussion	110
VIII	Summary and Discussion.....	113
	References.....	117
	Appendix.....	125
	Abbreviations	125
	List of Figures.....	127
	List of Tables	135
	Lebenslauf	137

I Introduction

A fundamental aim in biophysical chemistry is gaining insights into complex biological processes, wherefore model systems relying on bottom-up or top-down approaches emerged to be general strategies to strip down native systems to their essential features. In top-down approaches, whole cells are studied with a broad variety of methods to derive datasets from which interpretations concerning metabolic or signaling pathways can be made. Hereby, also the development of new hypotheses of regulatory mechanisms of cells is an important part of such studies. In contrast, in bottom-up approaches, the starting point is set by biological knowledge, which is already defined. Here, model systems with growing complexity are established and enhanced giving the possibility to focus on single molecules and components and their interaction, whereby the results are correlated with datasets derived from whole cell studies (1).

Especially, the concept of artificial cells gained a lot of interest since this model was first envisioned by Aleksandr Oparin in the 1920s. Here, bottom-up as well as top-down approaches are employed, both enabling a broad usage in therapeutic applications, *e.g.* target-specific drug delivery. To mimic the complex interplay of essential parts of cells employing bottom-up systems, molecular components are assembled, providing the possibility to build artificial cells which contain a specific geometry and are able to sense and transport biomolecules. In contrast to that, in the corresponding top-down approach, living cells are, for instances, introduced into biological systems for the production of specific proteins (2).

In this work, a model system will be introduced as a bottom-up approach with the aim of gaining insights in the complex field of protein-mediated membrane-membrane interactions up to membrane fusion (see Chapter I.1) (3). A particular focus is laid on coiled-coil proteins forming strong but transient connections between cell-cell borders, *i.e.* membranes (see Chapter I.2). Furthermore, an overview considering model system mediated membrane fusion is given in Chapter I.3.

I.1 Membrane-Membrane Interaction and Fusion

Eukaryotic cells are compartmentalized by biological membranes formed by a variety of lipids and proteins, which serve as dielectric barriers (4). Hereby, inner structures like organelles of the cells are separated from each other and the surrounding extracellular area. A controlled transport through those bordering structures up to complete merging of membranes is pivotal

for manifold processes such as exocytosis. Intracellular exocytotic pathways are crucial in trafficking and transport processes like the release of neurotransmitters. Besides, the developments during fertilization, tissue formation and viral infection heavily rely on intercellular membrane fusion events (5).

During the process of membrane fusion, two separated lipid bilayers need to come into close proximity followed by merging of the proximal monolayers, known as hemifusion, which subsequently can be expanded and opened to a fusion pore (see Fig. I.1) (6).

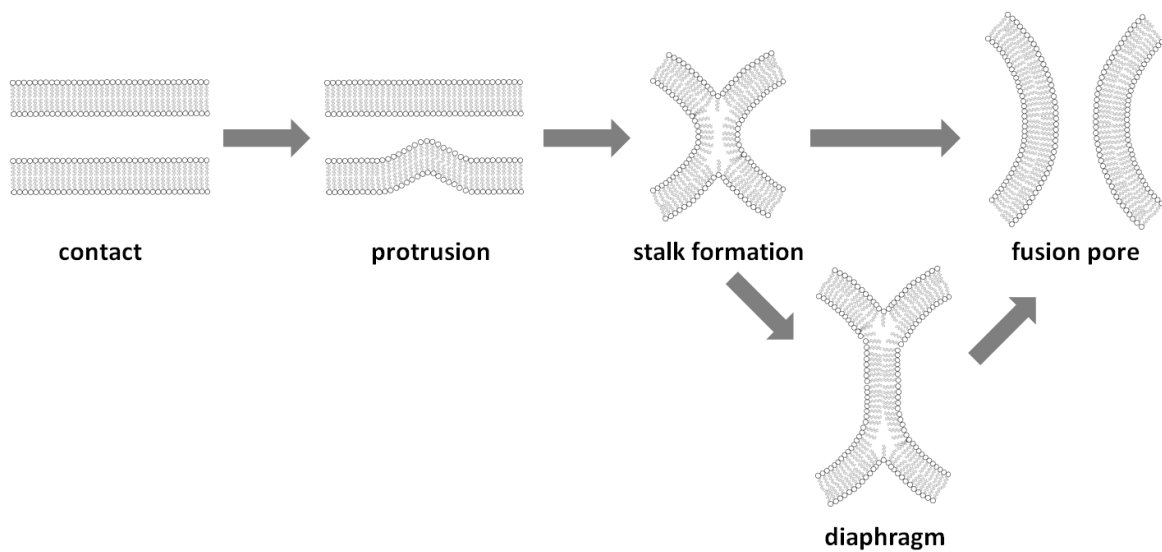


FIGURE I.1 Membrane topology during membrane fusion pathway. *From left to right:* Membranes come into close contact until a point-like protrusion is formed. Subsequently, a hemifusion stalk is formed, which can be either expanded to a hemifusion diaphragm or opened up to a full fusion pore directly.¹

The protrusion can be described as point-like, since hydration repulsion hinders membranes to come into close contact, which is reduced by a minimized contact area. In the stalk formation step, which forms the hemifused state, the hydrophilic and hydrophobic parts of the bilayer need to be destabilized to merge. This hemifused state, in which a stalk is generated and present, is highly transient but in 2009 Aeffner *et al.* were able to show this fusion intermediate by means of an X-ray scattering study (7). In general, two possible pathways after stalk formation are conceivable: a direct opening of a fusion pore or a detour attending the formation of an extended stalk, a so-called diaphragm. This stalk hypothesis was first described in 1984 (8) and revisited in 2002, demanding a free energy increase due to stalk formation and hemifusion of $13 k_B T$, whereas full fusion requires an energy up to $46 k_B T$ (9). Furthermore, in this theoretical study, it was shown that the two different pathways following stalk formation, *i.e.* enlargement

¹ Figure redrawn from: L.V. Chernomordik and M.M. Kozlov, *Nat. Struct. Mol. Biol.* **2008**, *15*, 675-683.

of stalk or the opening to a fusion pore, are both eminent possible. All these processes need to fulfill the mandatory conditions for successful fusion, accompanying a full merging of lipids and content, without the occurrence of leakage.

Since biological membranes are intrinsically stable, the three stages of contact, hemifusion and full fusion do not occur spontaneously but need to be mediated by energy supplying proteins (10, 11). The overall protein content in membranes is strongly dependent on the considered organelles and cell parts, but can be assumed to be in a range of 1:4 to 4:1 concerning the weight ratio of proteins to lipids (4). According to the fluid mosaic model derived from Singer and Nicolson in 1972, proteins and lipids in a membrane are considered as highly mobile like in a two dimensional fluid (12). However, membranes do not display a homogenous distribution, instead a distinct clustering and high degree of sorting into so-called domains and lipid rafts can be found (13). Inside those domains, also the membrane fusion mediating protein complexes can be enriched, resulting in a defined lateral organization (14). Hereby, the following highly controlled protein folding processes occur in a specific spatial distribution, whereas neither the folding nor the sorting mechanisms in exocytosis are fully understood yet.

I.2 Coiled-coil Proteins as Motors for Membrane Fusion

Coiled-coil motifs are formed by two or more α -helices wrapping around each other constructing a single, in most cases left-handed, superhelix. It is a widely employed structure in eukaryotic cells, present in proteins of neurons, muscle, hair, and skin (15). The strong but non-covalent and hence flexible connection of the formed coiled-coil structure makes it an ideal motif in dynamic processes, *e.g.* transport or membrane-fusion. Motor proteins like myosin, which is involved in muscle contractions and connected to actin filaments, and kinesin or dynein, two motor proteins responsible for transport processes along microtubule, all display a superhelical structure which enables their dynamic activities (4). Geometry and aggregation state, *i.e.* number of strands participating in bundle formation, are governed mainly by the amino acid sequence (16).

When it comes to membrane fusion, coiled-coil interactions are abundantly found to overcome the energy barrier. Enveloped viruses such as HIV (17) and influenza (18, 19) employ coiled-coil sequences as a central folding motif to produce membranes in close contact that eventually drive merging of bilayers and content mixing via a spring-load mechanism. In viral infection, the fusion machinery is completely located in the viral membrane. For exocytotic processes, which

are uninfected, both interacting membranes are decorated with parts of the fusogenic protein complex.

Among the most intricate fusion processes is the calcium stimulated exocytosis of synaptic vesicles to release neurotransmitters in the synaptic cleft involving a variety of proteins (SNAREs - soluble N-ethylmaleimide-sensitive-factor attachment protein receptors) assembling into a parallel-oriented ternary coiled-coil bundle (20). An eight heptad repeat segment is responsible for the highly stable coiled-coil motif (21, 22). Due to a zipper mechanism, the SNARE core complex formation brings membranes into close contact and therefore overcomes the hydration barrier, hence fusion can occur (23, 24). The interplay of the proteins syntaxin, synaptobrevin and SNAP25, which are generating the SNARE core coiled-coil complex, is depicted in Figure I.2 (22).

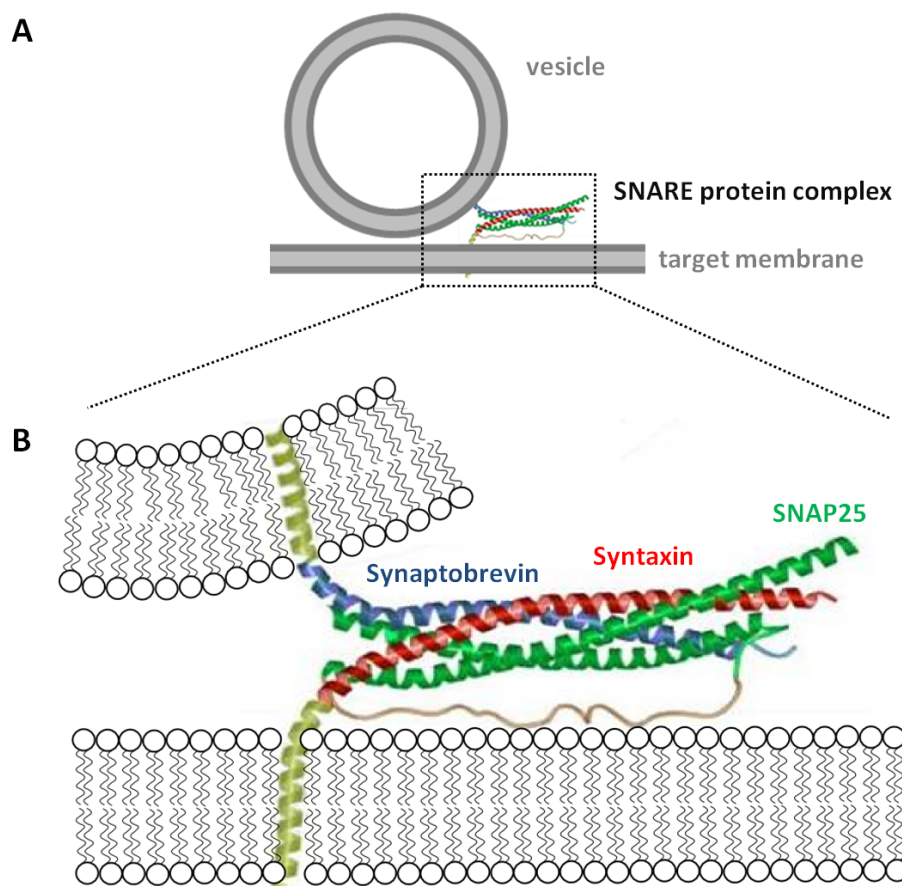


FIGURE I.2 SNARE mediated membrane fusion. (A) Schematic drawing of a SNARE mediated interaction of a vesicle with a target membrane. Enlarged drawing of SNARE protein complex (scattered box) is shown below. (B) Structure of the core complex consisting of syntaxin (*red*), synaptobrevin (*blue*) and SNAP25 (*green*) attached to bilayers via transmembrane domains (*yellow*).²

² Figure adapted from: R.B. Sutton, D. Fasshauer, R. Jahn, and A.T. Brunger, *Nature* **1998**, 395, 347-353.

Synaptobrevin and syntaxin are both anchored in membranes via a transmembrane domain, which show a propagation of the α -helical structure into both protein connected membranes upon coiled-coil formation, accomplishing the actual energy transfer (25). Synaptobrevin is located at the transmitter filled vesicle, therefore it is also known as VAMP (vesicle associated membrane protein). On the other hand, syntaxin builds its counterpart at the target membrane as well as SNAP25 (synaptosomal associated protein), which is contributing two helical strands to the SNARE core complex (26). Instead of syntaxin and synaptobrevin, SNAP25 does not exhibit a transmembrane domain but is solely anchored in the synaptosomal membrane via a palmitoyl side chain located in the center of the protein. Hence, the anchorage of SNAP25 can be considered as hybrid lipid-protein moiety.

The gain in free energy upon formation of coiled-coil strands is $35-50 k_B T$ - about $5-6 k_B T$ per heptad repeat - predominately due to the packing of the hydrophobic residues facing against each other (27). Considering the calculated energy needed for membrane fusion, one SNARE complex should be sufficient for membrane fusion, which could be shown in 2010 by van den Boogart and coworkers (28).

I.3 Model Systems for Membrane Fusion in Biophysical Chemistry

In the last years, a broad variety of minimal model systems were established to mimic membrane fusion in bottom-up approaches, accompanying DNA (deoxyribonucleic acid) (29-31), PNA (peptide nucleic acid) (32) or short peptides (33, 34) as recognition sequence. All those model systems have in common that the dimerization takes place in a zipper-like fashion as in native fusion proteins. The peptides are actually designed as short specific heterodimeric coiled-coil structures, whereas the DNA and PNA undergo similar superhelix formations while building up the double stranded structures.

A recurring question addressed by these studies, is the impact of employed anchorage in the lipid bilayer. Whereas Meyenberg *et al.* (34) anchored the recognition peptide sequence into the bilayer via a transmembrane protein linker derived from native SNARE proteins, Marsden *et al.* (33) employed a phospholipid anchor. Both were able to show significant lipid as well as content mixing, although an exact comparison concerning the fusion efficiency is not possible, since different normalizations of data were carried out. However, in a publication by McNew *et al.* it was shown, that the anchorage has a high impact on fusion efficiency, with transmembrane linkage clearly favoring bilayer merging over simple lipid anchoring (35).

Furthermore, the orientation of dimerized recognition sequences has a distinct effect on fusion efficiency. In the study carried out by Lygina *et al.* parallel and antiparallel heterodimerization induced by PNA recognition were compared, showing a higher fusion efficiency for PNA dimers exhibiting parallel binding (32). In contrast to the transmembrane anchorage used for the PNA attachment, the studies using DNA (31) were carried out employing solely a lipid linker for the membrane anchorage. In this study, only parallel DNA superhelices showed distinct fusion efficiency, while for the antiparallel heterodimerization only docking occurred. The defined alignment in a parallel and antiparallel manner was yet only possible for PNA and DNA, since for those structures the orientation is clearly defined by the Watson-Crick base pairing (4).

In this work, a versatile peptide model system that allows for specific formation of parallel and antiparallel coiled-coil structures was synthesized and characterized providing insights in kinetics, thermodynamics and structure of membrane fusion.

II Motivation - Establishing a Model System

Membrane fusion plays a pivotal role in processes that require transport of molecules that would otherwise not be capable of crossing the lipid bilayer (5, 36), whereas the initial adhesion between the opposing membranes is often generated by coiled-coil formation involving two or more amino acid strands (37). Hereby, membranes are brought into close contact and energy released upon protein oligomerization is transferred to the lipid bilayer to overcome the hydration barrier. In this work we will focus on a peptide model system, which is specific and gives the possibility to be varied concerning structure and geometry of coiled-coil formation. Hence, parallel and antiparallel heterodimerization with subsequent membrane-membrane interaction will be studied as well as the impact of different spacer moieties on peptide packing. Hereby, a successful functionalization of membranes by formation of hybrid lipid-peptide structures is a crucial step to control the complexity of employed system and to mimic the native-like membrane-membrane interaction. Furthermore, this work focuses on structural, thermodynamic and kinetic aspects during coiled-coil formation comparing experiments in solution and in the context of membranes.

The aim of this work is to design, compare and understand a set of minimal model systems mimicking SNARE mediated membrane fusion, not only in their coiled-coil forming characteristics, but especially in their thermodynamic and local aggregation behavior. Results from this minimized fusion complex are correlated with knowledge concerning native SNARE core complex formation, to gain insights in the complex protein-mediated fusion process. Additionally, a well understood and highly controllable fusogenic model system, gives rise to the possibility to specifically insert proteins into giant unilamellar vesicles (GUV) by fusion processes, which is an important step towards the successful build-up of artificial cells. Here, GUV could be generated with increasing complexity by a subsequent incorporation of proteins or building blocks of the cytoskeleton. Therefore, the impact of different components brought into cell-sized vesicles in a consecutive and well-controlled fashion can be studied in detail. Hereby, the applied bottom-up strategy starting from functionalized membranes towards artificial cells allows to control compositional as well as organization intricacy in a versatile fashion.

III Materials and Experimentals

We used a large variety of materials to mimic a membrane-membrane interaction with a model system consisting of coiled-coil peptides. In a bottom-up approach, the membrane of a cell was reduced to a single lipid bilayer consisting of various phospholipid mixtures, which could be fluorescently labeled with special modified lipids (see Chapter III.1). The functionalization with peptides was accomplished via an *in situ* coupling reaction of thiols to maleimide-modified lipids to form lipopeptides (see Chapter III.3). Therefore, peptides were specially designed and manually synthesized using solid phase peptide synthesis with subsequent purification by applying preparative reversed phase high pressure liquid chromatography (RP-HPLC) (see Chapter III.2).³

III.1 Artificial Membranes Formed by Phospholipids

In this work, artificial membranes composed of phospholipids were prepared. In Chapter III.1.1 basic principles of phospholipids and characteristics of lipid membranes will be described. Chapter III.1.2 focuses on chemically modified lipids, like those labeled with fluorophores or which were modified concerning their headgroup. Furthermore, cholesterol and its effects on phospholipid membranes will be shortly described. In Chapter III.1.3, the actual procedure for lipid handling is given.

III.1.1 Phospholipids and their Phase Behavior

In general, lipids are amphiphilic molecules containing a hydrophilic and a hydrophobic part. Due to their amphiphilic character, lipids show a tendency to aggregate in aqueous solutions, forming *e.g.* micelles, vesicles or bilayers that shield the hydrophobic residues from the aqueous phase. The shape of the lipid molecules defines the form of aggregation; hence cone-shaped lipids will form micelles while cylindrical molecules show a higher tendency for bilayer or vesicle formation. In this work, artificial membranes were produced as vesicle or as solid supported membrane (SSM) using phospholipids (see Fig. III.1). In both preparations, only the upper layer of a SSM and the outer layer of the vesicle, respectively, are accessible for further modifications. Since bigger and charged molecules are not able to pass through lipid

³ Chemicals used in this work were purchased in high purity grade and could be used without further purification.

bilayers, different solutions can be encapsulated in vesicle assays which are used to study fusion events. On the other hand, SSM enable a straightforward microscopic imaging down to molecular level. Furthermore, due to a thin water layer with a thickness of 1-3 nm between the lipid bilayer and substrate, characteristics like fluidity of a free membrane are preserved (38).

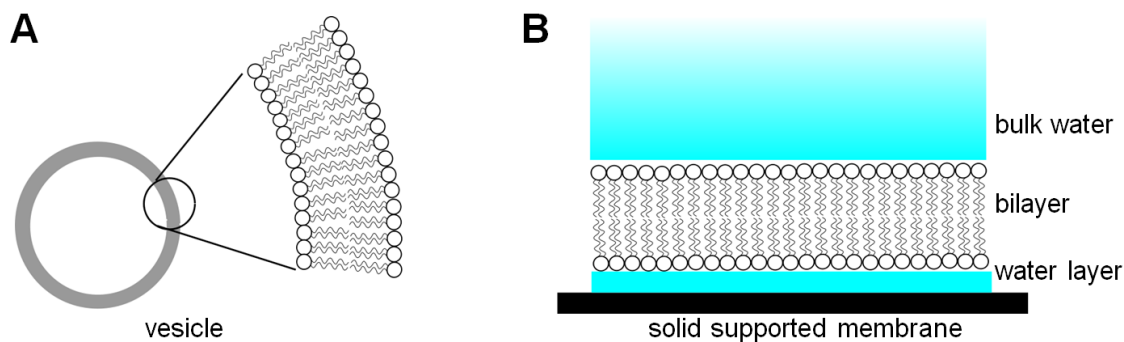


FIGURE III.1 Schematic drawing of an unilamellar vesicle (A) and a solid supported lipid membrane (B).

In phospholipids, the hydrophobic part is formed by two fatty acid chains, which are coupled to a glycerin backbone of the lipid via ester bonds. The third hydroxyl group of the glycerin backbone is coupled to a phosphate, which is bound to different alcohol functions and forms the hydrophilic headgroup of the phospholipid. The names of these molecules are usually abbreviated by a 4-letter code: at the third position of the abbreviation, a P is used for the phosphate group, while the first two letters refer to the esterified fatty acid chains and the last one refers to the alcohol. Possible headgroups are choline (PC lipids), serine (PS), ethanolamine (PE), glycerin (PG) or the sugar inositol (PI). The headgroup defines by its own carried charge the overall charge of the lipid, since the phosphate group is deprotonated under physiological conditions. This results in a net charge of zero for PC and PE lipids while PS, PG and PI lipids carry a negative charge.

Phospholipids are present in two different phases, the gel phase, also known as $L_{\beta'}$, and the fluid phase (L_{α}). In $L_{\beta'}$ phase, the lipids are tilted by 35° in comparison to the fluid phase. Furthermore, the lateral diffusion is slowed down by three orders of magnitude from $\approx 10^{-8} \text{ cm}^2/\text{s}$ to $\approx 10^{-11} \text{ cm}^2/\text{s}$ (39). The reason can be found in the molecular alignment of the fatty acid chains, which form a rigid all-trans conformation (see Fig. III.2).

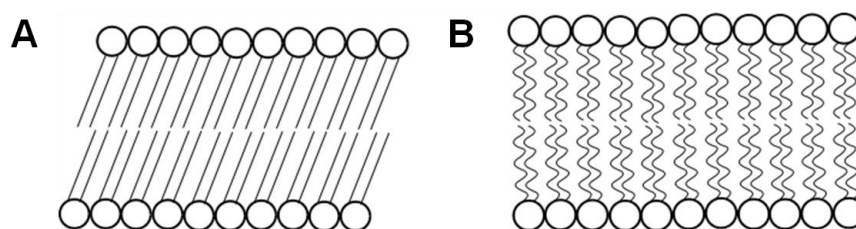


FIGURE III.2 Schematic drawing of fatty acid chain packing in (A) gel phase and (B) fluid phase lipid bilayers.

The phase transition temperature T_m is defined by the ionic interaction between the hydrophilic headgroups as well as by the character of the fatty acid chains present in the phospholipid. Fully saturated and relatively long alkyl chains enable a dense packing with more interactions between the hydrophobic residues; hence the phase transition temperature increases. In contrast, unsaturated fatty acid chains decrease the phase transition temperature due to their tilted geometry.

An overview of the phospholipids used in this work is given in table III.1 (all lipids were purchased from Avanti Polar Lipids, Alabaster, AL, USA):

Lipid	chemical name	saturation*	$T_m / ^\circ\text{C}^4$
DMOPC	1,2-dimyristoleoyl- <i>sn</i> -glycero-3-phosphocholine	14:1 - 14:1	n.a.
DΔPPC	1,2-dipalmitoleoyl- <i>sn</i> -glycero-3-phosphocholine	16:1 - 16:1	- 36
DOPC	1,2-dioleoyl- <i>sn</i> -glycero-3-phosphocholine	18:1 - 18:1	- 20
DEPC	1,2-dieicosenoyl- <i>sn</i> -glycero-3-phosphocholine	20:1 - 20:1	n.a.
POPC	1-palmitoyl-2-oleoyl- <i>sn</i> -glycero-3-phosphocholine	16:0 - 18:1	- 2
DPPC	1,2-dipalmitoyl- <i>sn</i> -glycero-3-phosphocholine	16:0 - 16:0	41
DOPE	1,2-dioleoyl- <i>sn</i> -glycero-3-phosphoethanolamine	18:1 - 18:1	- 16
POPE	1-palmitoyl-2-oleoyl- <i>sn</i> -glycero-3-phosphoethanolamine	16:0 - 18:1	25
DPPE	1,2-dipalmitoyl- <i>sn</i> -glycero-3-phosphoethanolamine	16:0 - 16:0	63

TABLE III.1 Abbreviated lipid names, chemical names, saturation of fatty acid chains and the phase transition temperature T_m of lipids used in this work. *) [(number of carbons in fatty acid chain):(number of double bonds)] ratio is given for alkyl chains at position 1 and 2.

⁴ Phase transition temperatures extracted from avantilipids.com (25. 07. 2012)

III.1.2 Chemically Modified Lipids

The phospholipids described in Chapter III.1.1 were used as matrix lipids, *i.e.* they served as surrounding material defining for example the fluidity of those molecules the experimental focus was laid on. The latter ones were mainly chemically modified lipids carrying receptor groups like maleimide or fluorophores (see below).

III.1.2.1 Maleimide Functionalized Lipids

Phospholipids with a maleimide-functionalized headgroup were used as receptor lipids for peptide attachment (see Chapter III.3). The double bond of the maleimide groups works as an acceptor in a Michael-addition with a cysteine residue of the peptide as donator (40). The maleimide modification is introduced to PE lipids using a cyclohexyl group as a spacer. Since fluid phase lipids and gel phase lipids are not miscible (41), two different phospholipids (DOPE and DPPE) were employed as matrix lipids to allow functionalization of both lipid phases. The full structures of the used lipids MCCDOPE (fluid phase; 1,2-dioleoyl-*sn*-glycero-3-phosphoethanolamine-N-[4-(*p*-maleimidomethyl)cyclohexane-carboxamide]) and MCCDPPE (gel phase; 1,2-dipalmitoyl-*sn*-glycero-3-phosphoethanolamine-N-[4-(*p*-maleimidomethyl)-cyclohexane-carboxamide]) are shown in Figure III.3, which were used in concentrations ranging from 1-10 mol%.

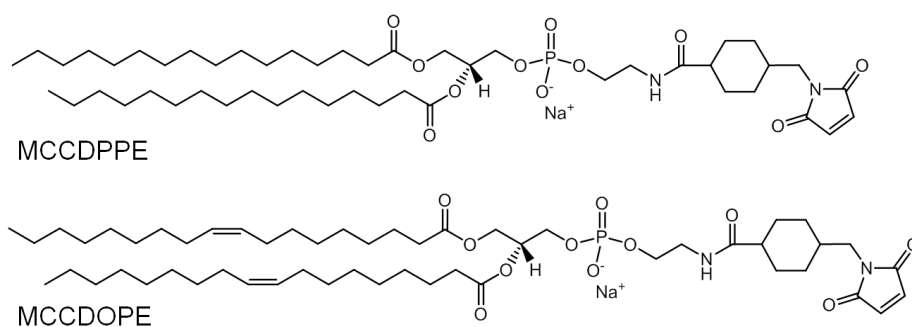


FIGURE III.3 Chemical structures of maleimide functionalized lipids MCCDPPE (gel phase) and MCCDOPE (fluid phase).

III.1.2.2 Fluorescently Labeled Lipids

Some experiments required fluorescently labeled membranes to enable microscopic or spectroscopic detection. Therefore, lipids were covalently bound to a fluorophore. Both lipids used in this work are in their fluid phase at room temperature, therefore located also in fluid phase membranes. Texas Red (Texas Red DHPE; Texas Red-1,2-dihexadecyl-*sn*-glycero-3-phosphoethanolamine, triethylammonium salt) is a very stable red fluorophore while BODIPY (β -

BODIPY 500/510 c12-HPC; 2-(4,4-difluoro-5-methyl-4-bora-3a,4a-diaza-s-indacene-3-dodecyl)-1-hexadecyl-*sn*-glycero-3-phosphocholine) emits green fluorescence and is easy to bleach, which makes it a suitable label for lateral diffusion studies (Invitrogen, Darmstadt, Germany). Their structures and their absorption and emission spectra are shown in Figure III.4.

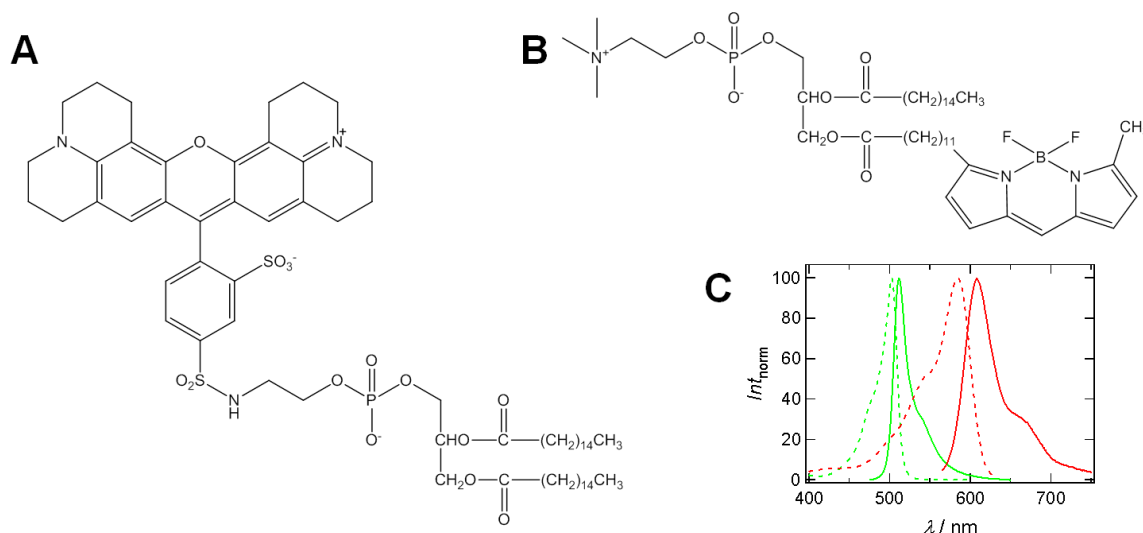


FIGURE III.4 Chemical structures of used lipid conjugated fluorophores Texas Red (A) and BODIPY (B) as well as their absorption and emission spectra (C). Spectrum of BODIPY is shown in green, Texas Red in red. Absorption line is represented by a dotted line, emission spectra is shown as solid line.

The fluorescently active groups were either attached to the hydrophilic headgroup, as in the case of Texas Red, or attached to the hydrophobic fatty acid residue (BODIPY). Since the fluorescently active moieties have a large structure, a potential influence on the lipid membrane cannot be definitely excluded and will be also dependent on the position of the employed fluorophore in the bilayer. Hence, for Texas Red with a large and partially charged headgroup unspecific adsorption might occur, while BODIPY might influence packing and therefore fluidity of the fatty acid moieties.

III.1.2.3 Cholesterol

Cholesterol is an important part of native plasma membranes since it modulates the stability of the lipid bilayer. Due to its small hydrophilic hydroxyl group and its bulky hydrophobic steroid moiety, it has a high influence on the packing density of fatty acid chains. For example, if sphingomyelin is present in unsaturated PC bilayers, an addition of 20-30 mol% cholesterol results in a phase transition to the liquid ordered L_o phase. Here, the lipids exhibit still a relatively high lateral mobility like in the fluid phase, but the acyl chains are more ordered and hence an extension of layer thickness is observed (39, 42).

III.1.3 Vesicle Preparation and Bilayer Formation

Lipid stock solutions ($c_{\text{lipid}} = 1\text{-}10$ mg/mL) were prepared in chloroform and transformed into lipid films by removal of the solvent in a nitrogen stream followed by 3 h drying in vacuum. Multilamellar vesicles (MLV) were produced by dissolving lipid films in buffer at a concentration of 1 mg/mL. Therefore, the lipid films were heated to a temperature above the highest T_m present in the lipid mixture and mixed several times, until a turbid solution was obtained. MLV were transformed into small unilamellar vesicles (SUV) by sonication (50 W, 0.4 s Puls, 30 min) in a vessel resonator (Sonoplus HD 2070, Bandelin, Berlin, Germany). Vesicle size was determined by DLS (dynamic light scattering, see Castorph *et al.* (43)), which showed that SUV have a diameter of 30-50 nm. If the MLV solution should be transformed into large unilamellar vesicles (LUV), extrusion (LiposoFast Extruder, Avestin, Ottawa, Canada) was applied. Here, the solution is pressed 31× through a porous polycarbonate membrane available with pore diameters ranging from 50-5000 nm. An advantage of this method is that vesicle size shows a relatively narrow distribution in comparison to vesicles prepared by sonication (44).

Solid supported membranes (SSM) were formed by spreading SUV on a hydrophilized surface at temperatures above phase transition of used lipids (45). Therefore, the surfaces were incubated with a SUV solution ($c_{\text{SUV}} \approx 0.1$ mg/mL) for at least 30 min at room temperature. If gel phase lipids were used, the sample was heated to 10-20 °C above the highest phase transition temperature present in the mixture for another 30-60 min. Afterwards, the formed SSM was thoroughly rinsed with buffer to remove excess vesicles.

In the following, hydrophilization protocols for the different substrates used in this work are described:

Mica is a sheet silicate mineral possessing very plain surfaces, what makes it a good substrate for AFM imaging. By removing the upper silicate layer with a simple strip of sticky tape, a freshly cleaved and hydrophilic surface is produced.

Silicon wafers were used in *e.g.* ellipsometry experiments. Native SiO_2 was removed from the surface by incubating the wafers in diluted hydrofluoric acid (1 % in H_2O ; 15 min). Afterwards, a controlled reoxidation was performed in $\text{NH}_3 / \text{H}_2\text{O}_2 / \text{H}_2\text{O}$ 1:1:5 at 70 °C for 15 min. The hydrophilized wafers were stored in water and could be used for two days. To intensify the effect of controlled reoxidation, O_2 -Plasma (1 min) can be used directly before usage of the wafers.

Glass (e.g. glass bottom dishes, MatTek Corporation, Ashland, MA, USA) was hydrophilized after cleaning with water and ethanol (*p.a.*) by incubating it in O₂-Plasma for 1 min.

III.2 Coiled-coil Forming Peptides

To mimic protein mediated membrane-membrane interaction, small peptides showing a self-assembly into heterodimeric coiled-coil structures were used. In this chapter, first an introduction to theory of coiled-coil forming peptides will be given focusing on orientation and stabilization of formed superhelices (see Chapter III.2.1). As a second focus synthesis and purification procedures will be explained for the peptide sequences used in this work (see Chapter III.2.2 and III.2.3).

III.2.1 Theory of Coiled-coil Formation

In biological systems, the driving force bringing membranes into close contact is often provided by coiled-coil formation; the aim in this work therefore was to produce a small but specific dimeric system build up of short peptide strands. Coiled-coils are common structural motifs in native proteins consisting of two or more α -helices wrapping around each other under formation of a left-handed superhelix. This additional torsion, also defined by the superhelical pitch length, leads to a decreased number of amino acids per turn of the helix, namely 3.5 (as compared to 3.6 in undistorted helices). Thus, the position relatively to the coiled-coil interface is repeated every seventh amino acid, e.g. every two turns, which is also known as heptad repeat. This repeat is usually referred to as $(a-b-c-d-e-f-g)_n$ and $(a'-b'-c'-d'-e'-f'-g')_n$, respectively, starting with a/a' at the N-terminus. The coiled-coil structure is stabilized by hydrophobic interactions between nonpolar amino acids at the positions a/a' and d/d' forming the core of a coiled-coil, and by ionic interactions between the amino acids at the positions e/e' and g/g' (see Fig. III.5). The remaining three positions b/b' , c/c' and f/f' are usually hydrophilic, since they form the backbone of the coiled-coil structure and work as boundary towards the aqueous area (46).

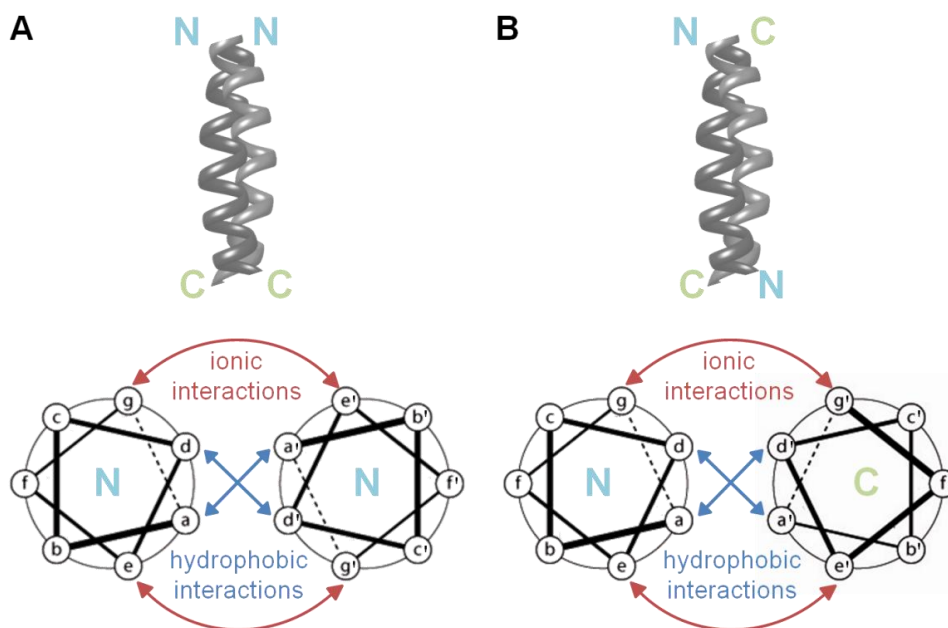


FIGURE III.5 Schematic representation of a parallel (A) and an antiparallel (B) dimeric coiled-coil. In the upper panel the relative positions of N- and C-terminus are shown; in the lower panel helical wheel diagrams are presented. One wheel represents one α -helical heptad repeat shown from the top, starting with N- or C-terminus, respectively, as indicated by the letter inside the wheel. The positions where ionic (red) and hydrophobic (blue) interactions are located are indicated with arrows.

In parallel dimeric structures, the interaction at the interface is found to be between a and a' residues and d and d' , respectively, while ionic interactions are located positions at g/e' and e/g' , respectively. This order is inverted for antiparallel dimeric coiled-coils: here, the stabilizing interactions are located at a/d' (d/a') and e/e' (g/g'), respectively. But in both cases one heptad repeat is not enough to stabilize a coiled-coil structure; hence, a serial connection of such elementary sequences comes into play. An important difference between parallel and antiparallel dimeric coiled-coil structures has its origin in the permanent dipole of α -helices (47). Since the peptide bond moiety presents a permanent dipole in N-direction, which is consistent over the whole helical structure, the N-terminus can be considered as slightly positively charged. Hence, in parallel coiled-coils, two equally charged termini are neighbored, while this is not the case in antiparallel coiled-coil structures.

In 2002 Litowski and Hodges designed a short but specifically interacting heterodimeric two-stranded coiled-coil either rich in glutamic acid (E-peptides) or lysine (K-peptides) used in this work and consisting of only three heptad repeats (48). The high stability and specificity of this model system is due to the employed amino acids in the peptides' recognition sequences: lysine (Lys, K), which is positively charged under physiological conditions, is at the positions e and g in the K-sequence, while the negatively charged glutamic acid (Glu, E) residues form its

counterparts in E-peptides. The amino acids exposed to the solvent are chosen to be alanine (Ala, A) at *c* and *b* positions to increase the overall helical propensity, while for the *f* position a charged amino acid with opposed charge to the *e* and *g* positions is introduced to increase water solubility and to reduce the overall net charge. Finally, leucine (Leu, L) and isoleucine (Iso, I) are occupying the hydrophobic positions *a* and *d* stabilizing with their residues the inner core complex. Furthermore, they define the packing direction concerning parallel and antiparallel dimerization, respectively. For the parallel case, it is well known that leucine residues are conserved at position *a* in the hydrophobic core, while β -branched amino acids like isoleucine can be found at position *d* (49). Thereby, a Leu-Leu interaction at the positions *a/a'* and a Ile-Ile interaction at *d/d'* form the hydrophobic core in “knobs-into-holes” manner, which defines the packing direction (50).

In this work, we broadened the well established model system described above by the possibility to produce parallel and antiparallel heterodimerization of peptide strands and furthermore investigated different spacer moieties between recognition sequence and membrane. Therefore, a set of three different E-K heterodimers was synthesized by the means of solid phase peptide synthesis and purified via RP-HPLC.

III.2.2 Solid Phase Peptide Synthesis

Solid phase peptide synthesis (SPPS) was introduced in 1963 by Robert Bruce Merrifield (51), wherefore he was awarded the Nobel prize in Chemistry in 1984.⁵ In this method an amine-functionalized polystyrene resin is used to which N-terminal protected amino acids are coupled using different activation reagents for speeding up reaction time. Actually, Merrifield developed the SPPS employing Boc-protecting groups, which was refined by Carpino and Han in the early seventies by introducing the Fmoc-strategy (52). The big advantage in SPPS is that side products and excess reactants can be easily removed from the reaction mixture by filtration. Afterwards, a deprotection step is carried out to remove the N-terminal Fmoc-moiety and the next amino acid building block can be coupled, until the desired peptide is formed (see Fig. III.6).

⁵ Nobelprize.org: www.nobelprize.org/nobel_prizes/chemistry/laureates/1984/index.html (20. 07. 2012)

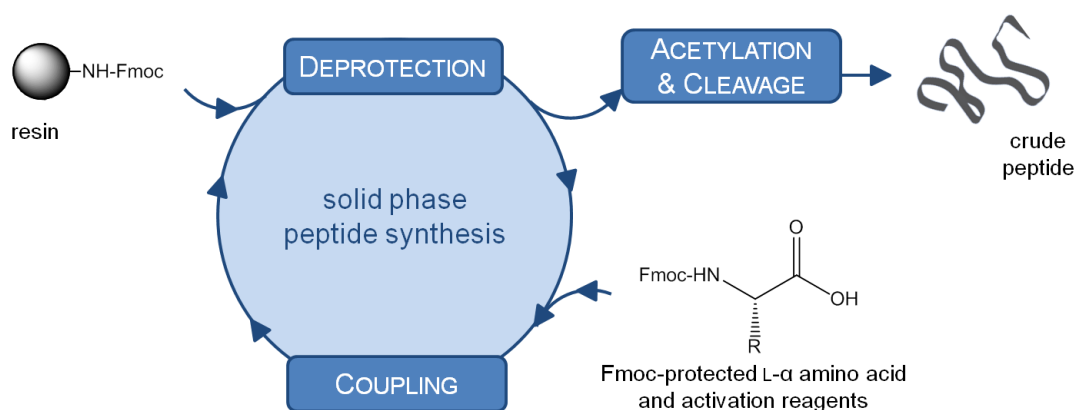


FIGURE III.6 Schematic presentation of reaction sequences applied in solid phase peptide synthesis. For each amino acid a new coupling step followed by a deprotection is carried out.

In this work, Fmoc-protected L- α amino acids were used with the activation reagents HBTU (2-(1H-Benzotriazole-1-yl)-1,1,3,3-tetramethyluronium-hexafluorophosphate) as an activated ester and DIEA (*N,N*-Diisopropylethylamine), also known as *Hünig's Base*, as non-nucleophilic base (53). HBTU forms an acyluroniumester with the free carbonyl function of the added amino acid and hence enables the formation of a new peptide bond (54). As solid phase, a Rink Amide MBHA resin LL was applied, a 4-methylbenzhydrylamine polystyrene derivatized with norleucine and a Fmoc-protected modified Rink Amide linker (see Fig. III.7). The LL indicates a low loading rate of the solid phase, which enables the synthesis of relatively long peptides due to minimization of steric hindrance; hence, less interactions between neighboring peptide chains can occur (all chemicals for SPPS were purchased from Novabiochem, Darmstadt, Germany).

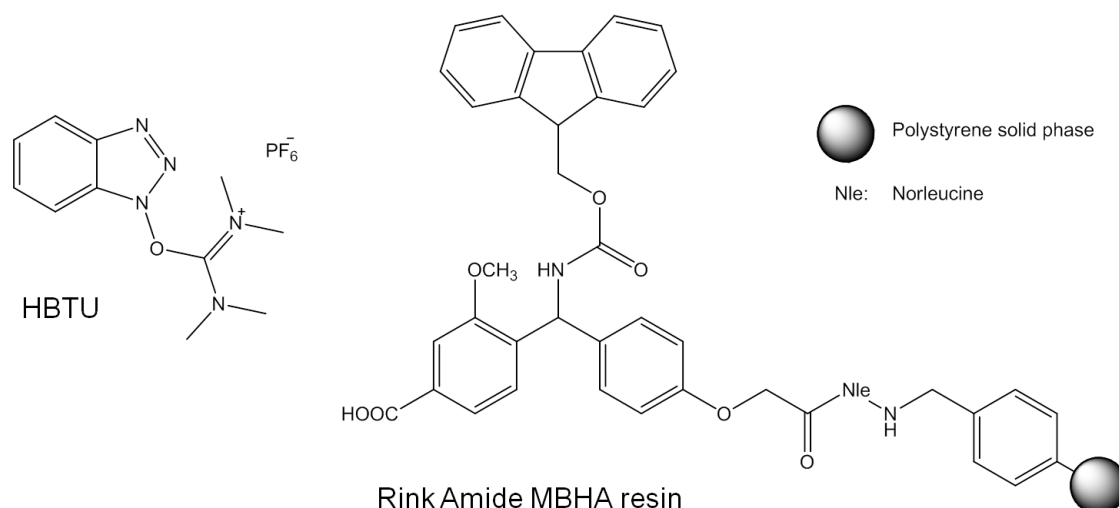


FIGURE III.7 Chemical structures of activation reagent HBTU and of Rink Amide MBHA resin.

The usage of a Rink Amide linker at the resin causes an amidation at the C-terminus, while the N-terminal amino acid is capped in a final coupling reaction by the means of an acetylation using

acetic anhydride in DMF. Afterwards, the cleavage step is carried out where the crude product is detached from the resin while additionally all side-chain protecting groups are removed from the peptide. In this work, a mixture of trifluoroacetic acid (TFA) with small amounts of water, triisopropylsilane (TIS), and 1,2-ethanedithiol (EDT) serving as scavengers is applied as cleavage cocktail, with the latter one preventing the formation of disulfide bridges between cysteine residues present in the peptide sequence. The reaction conditions of deprotection, coupling reaction, acetylation, and cleavage are shown in Figure III.8:

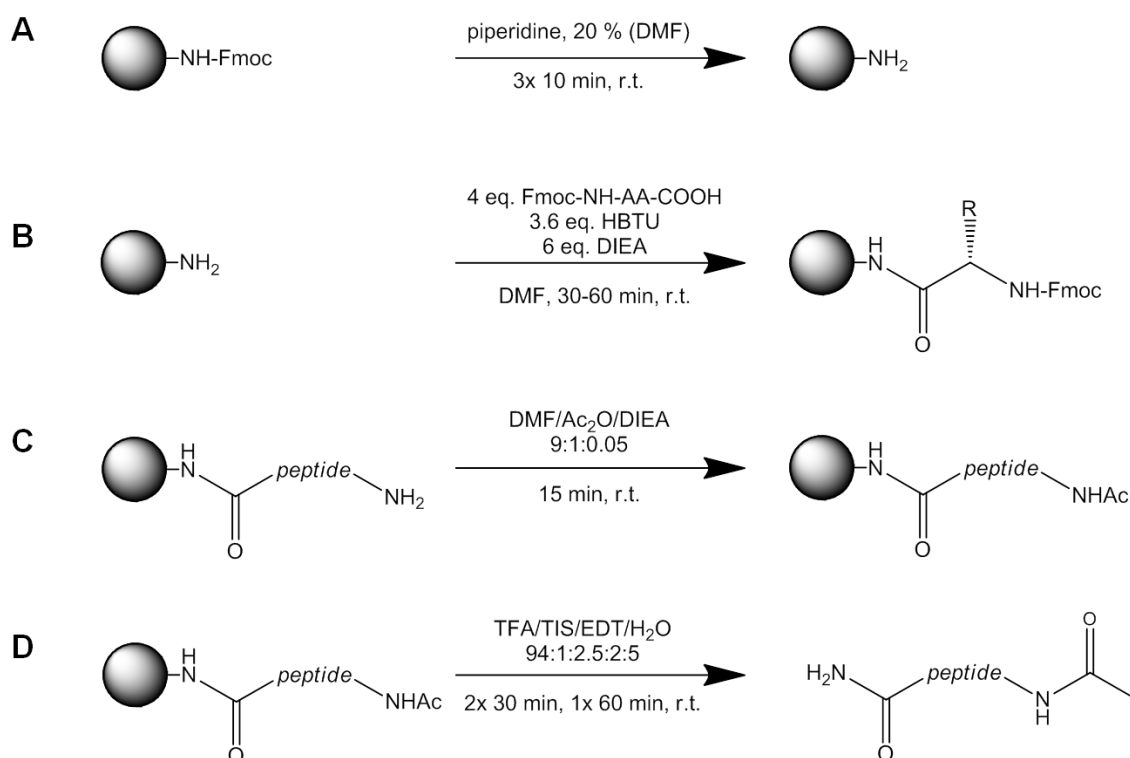


FIGURE III.8 Reactions carried out in SPPS. (A) Deprotection (removal of Fmoc protecting groups); (B) coupling reaction of amino acid building blocks; (C) acetylation of N-terminal amino group; (D) cleavage of crude peptide from the polystyrene resin and removal of all side-chain protecting groups.

The complete SPPS is carried out at room temperature with DMF as solvent in a constantly shaken vial (Wrist Action Laboratory Shaker model 75, Burrell, Pittsburgh, USA) to ensure sufficient mixing of the polystyrene beads with the reagents. The resin is swollen in DMF to enlarge the presented surface area and hence enable the accessibility of the functional moieties. All reactants are added in solution and between each step of the reaction the resin is thoroughly rinsed in the vial to remove potential side products, excess reactants, and impurities. After each coupling reaction, a ninhydrin staining (*Kaiser Test*) was done to check for coupling efficiency (55). In case of detection of free amino groups (blue coloration in *Kaiser Test*), the coupling step was repeated. After cleavage, the crude peptide is precipitated using ice-cold diethyl ether,

filtered, redissolved in a mixture of H₂O / AcCN / TFA 99:1:0.1, and finally lyophilized (ALPHA 1-2 LD plus, Christ, Osterode am Harz, Germany).

Employing this protocol, a set of three different coiled-coil forming peptide pairs was synthesized: K3Cys, and E3Cys, their analogs with inverted sequences *i*-K3Cys and *i*-E3Cys, as well as their PEGylated analogs *i*-K3PEG and *i*-E3PEG (for detailed amino acid sequences see Table III.2).⁶


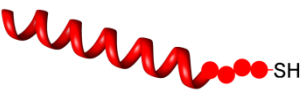


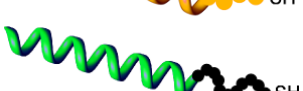
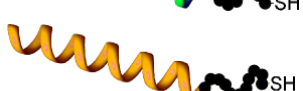
peptide		N-Terminus	Sequence	C-Terminus
	K3Cys	Ac-WG-	(KIAALKE) ₃	-GGGGC-NH ₂
	E3Cys	Ac-	(EIAALEK) ₃	-GWGGGC-NH ₂
	<i>i</i>-K3Cys	Ac-WG-	(EKLAAIK) ₃	-GGGGC-NH ₂
	<i>i</i>-E3Cys	Ac-	(KELAAIE) ₃	-GWGGGC-NH ₂
	<i>i</i>-K3PEG	Ac-WG-	(EKLAAIK) ₃	-G(PEG) ₁₁ C-NH ₂
	<i>i</i>-E3PEG	Ac-	(KELAAIE) ₃	-GW(PEG) ₁₁ C-NH ₂

TABLE III.2 Schematic drawings, names and primary sequences of peptides. N-terminus is acetylated, C-terminus amidated.

The used recognition sequences are inspired by Litowski and Hodges (48) and consist of a three heptad repeat building block which ensures a specific heterodimeric coiled-coil formation. Leucine (Leu, L) and isoleucine (Ile, I) stabilize the formed heterodimeric coiled-coil with hydrophobic interactions at the interface of the two peptide strands, while the ionic interaction between the amino acids at the positions *e* and *g* is given by lysine (Lys, K) and glutamic acid (Glu, E), respectively. The usage of latter mentioned amino acids as well as the trimer of heptad repeats leads to the abbreviated names E3 and K3 for the employed recognition sequences.

All peptides carry a C-terminal cysteine (Cys, C) residue, enabling a lipopeptide formation via an *in situ* coupling reaction to maleimide functionalized lipids (see Chapter III.3) (40). Due to this reason, 3-4 glycine (Gly, G) residues are included as a spacer between the actual recognition sequence and the C-terminus, to enable a certain range of mobility and minimize steric hindrance after attachment of peptides to a membrane. In the PEGylated sequence, instead of

⁶ *i*-E3PEG and *i*-K3PEG were synthesized by Maike Noster during her bachelor's thesis

the several glycine residues, a polyethylene glycol oligomer consisting of 11 monomers is introduced. This PEGylation was achieved during synthesis by the usage of Fmoc-NH-PEG₁₁-COOH as a building block, which could be coupled equivalently to an amino acid during coupling reaction. Furthermore, each peptide was doped with tryptophan (Trp, W) as a fluorescence marker.

III.2.3 Purification of Peptides via RP-HPLC

For purification of crude peptides, reversed phase high pressure liquid chromatography (RP-HPLC) was applied. In this technique, a hydrophobic stationary phase is combined with an eluent displaying a linear decreasing polarity. Hence, polar analytes elute first, followed by more hydrophobic molecules. The name “reversed phase” has historical reasons, because the first HPLC techniques were introduced with hydrophilic stationary phases, hence the polarity in RP-HPLC is reversed. Those hydrophilic stationary phases consisted mostly of silanol groups, which are nowadays chemically modified with *e.g.* alkyl chains to enable hydrophobic interactions.

In Figure III.9 a schematic setup of the employed RP-HPLC (L-6200A Intelligent Pump and L-4200 UV/Vis Detector, Merck-Hitachi, Darmstadt, Germany) is shown. Two solvent mixtures consisting mainly of water and acetonitrile (AcCN) RP-A and RP-B (solvent A: H₂O / AcCN / TFA 99:1:0.1; solvent B: H₂O / AcCN / TFA 10:90:0.05) are mixed gradually using a valve and a pump. Hereby, a linear decreasing polarity is achieved by steadily increasing the amount of RP-B resulting in increasing concentrations of acetonitrile in the mixture. Trifluoroacetic acid (TFA) serves as an ion pairing agent (56). Furthermore, it suppresses the interaction of peptides with residual free silanol groups on the stationary phase.

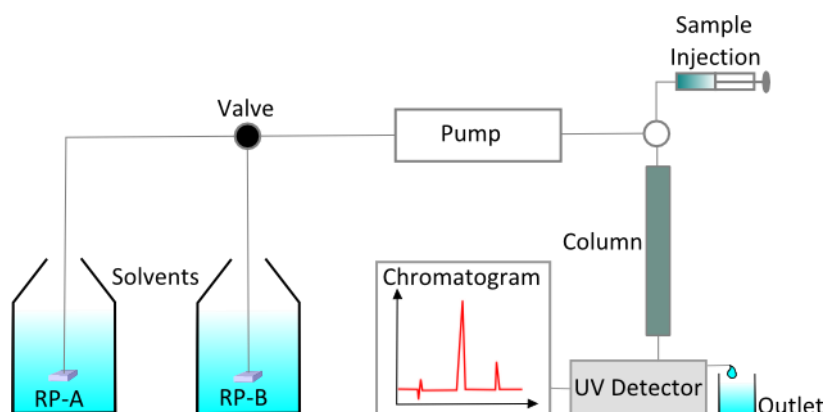


FIGURE III.9 Schematic drawing of RP-HPLC setup. The sample is injected to the HPLC and eluted with the solvent mixture. Peptides can be identified in a chromatogram using a UV detector at $\lambda = 220$ nm, the wavelength of absorbance for peptide bonds.

Peptides were purified with RP-HPLC using Grace Vydac C18 columns. Here, the stationary phase is modified with long alkyl chains (C18) serving for the high hydrophobicity. First, a preparative column (Grace Vydac, Protein and Peptide C18, 22 mm × 250 mm) was used which could be loaded with up to 30 mg of crude peptide and was operated with a flow rate of 8 mL/min. For final determination of purity, an analytical column (Grace Vydac, Protein and Peptide C18, 4.6 mm × 250 mm) with a maximum load capacity of 1 mg and a flow rate of 1 mL/min was employed. Identification of peptides was achieved via ESI-MS and HR-MS analysis (electro spray ionization and high resolution mass spectrometry, Apex IV, Bruker Daltonics, Billerica, MA, USA).

All peptides were purified following the same general procedure for RP-HPLC. First, a broad gradient of RP-B ranging from 20-80 % was applied to identify the raw elution time of the analyte. Afterwards, the gradient was adjusted with the aim to have an increase of not more than 20 % of RP-B in the defined elution time of 20 min. Since E3Cys and *i*-E3Cys, as well as K3Cys and *i*-K3Cys, respectively, consist of the same amino acids and therefore exhibit identical sizes and net charges, they would only show different elution times if different folding in the secondary structure would be present. Since this is not the case, identical purification protocols could be applied.⁷ PEGylation increased the polarity of the peptides in comparison to the glycine spacer, therefore the amount of RP-B for elution needed to be reduced⁸. The final gradients used for the different peptides are given in table III.3:

<i>t</i> / min	E3Cys / <i>i</i> -E3Cys		K3Cys / <i>i</i> -K3Cys		<i>i</i> -E3PEG		<i>i</i> -K3PEG	
	RP-A / %	RP-B / %	RP-A / %	RP-B / %	RP-A / %	RP-B / %	RP-A / %	RP-B / %
0	52	48	67	33	60	40	70	30
20	35	65	52	48	32	58	55	45
21	0	100	0	100	0	100	0	100
30	0	100	0	100	0	100	0	100
31	52	48	67	33	60	40	70	30
39	52	48	67	33	60	40	70	30

TABLE III.3 Linear polarity gradients used in RP-HPLC for peptide purification. First line names the peptides the gradient was applied to. Amounts of RP-A (H₂O / AcCN / TFA 99:1:0.1) and RP-B (H₂O / AcCN / TFA 10:90:0.05) are given in volume percentage. 0-20 min: linear polarity gradient; 21-30 min: cleaning of stationary phase; 31-39 min: preparation of stationary phase.

⁷ E3Cys was synthesized in cooperation with Cornelia Panse, PhD student (AG Diederichsen, Göttingen)

⁸ *i*-E3PEG and *i*-K3PEG were purified by Maike Noster during her bachelor's thesis

All peptides were dissolved in the starting gradient mixture to give a final concentration of 10 mg/mL. This solution was then injected onto the column (2 mL; 20 mg of crude peptide) and the aimed fractions were collected within the linear polarity gradient (see Fig. III.10 A). Afterwards, a cleaning step was introduced ($t = 21-30$ min, 100 % RP-B) to elute all residues from the column. The last 8 minutes, the column was incubated with the starting gradient mixture, to prepare the RP-HPLC for a further purification run. The acetonitrile present in the collected fractions was removed using a rotary evaporator followed by lyophilization. The purity of the product was determined with analytical RP-HPLC (linear gradient: 20-80 % RP-B, 20 min) (see Fig. III.10 B), furthermore the product was identified by ESI-MS.

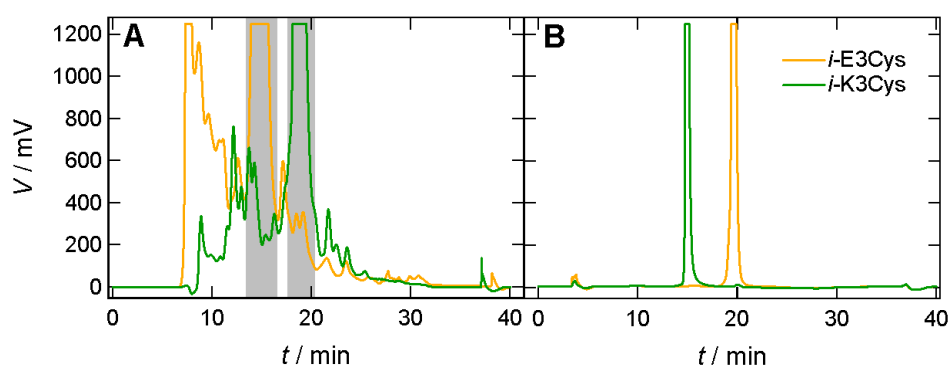


FIGURE III.10 Purification of *i*-E3Cys (yellow) and *i*-K3Cys (green) by (A) preparative RP-HPLC with a linear polarity gradient (see table III.3). Collected fractions are highlighted in grey. (B) Purity control determined with analytical RP-HPLC.

The retention times t_R for the analytical RP-HPLC (20-80 % RP-B, 20 min), the determined purity (integration of product peak) and the main peak in ESI-MS ($[M+H]^+$) of the synthesized peptides are presented in table III.4:

	E3Cys	K3Cys	<i>i</i> -E3Cys	<i>i</i> -K3Cys	<i>i</i> -E3PEG	<i>i</i> -K3PEG
t_R / min	19.6	14.0	19.4	14.7	22.0	20.4*
purity / %	94	93	96	95	69	94
m/z ($[M+H]^+$)	2840.5	2894.7	2840.5	2894.7	3269.8	3322.9
M_{calc} / g/mol	2839.5	2893.7	2839.5	2893.7	3270	3324

TABLE III.4 Retention times t_R and determined purity from analytical RP-HPLC (20-80 % RP-B, 20 min; * for *i*-K3PEG: 30-45 % RP-B, 20 min), m/z ratio for $[M+H]^+$ ion determined from ESI-MS (HR-MS), and calculated molar weight of synthesized peptides.

III.2.4 Handling and storage of peptides

All peptides used in this work were stored in dried state at - 20 °C. To allow for better handling, aliquots in small reaction vials were prepared. Therefore, peptides were dissolved in RP-A (H₂O / AcCN / TFA 99:1:0.1) to give stock solutions of 1 mg/mL. Afterwards, reaction vials were filled with the volume equivalent to 10-100 nmol of peptide. Finally, the reaction vials were dried over night in a vacuum concentrator (Concentrator 5301, Eppendorf, Hamburg, Germany) and stored at - 20 °C. Peptides used for IR measurements were lyophilized 5× with 0.05 M HCl to replace trifluoroacetate counterions at peptide backbone with chloride ions (57) and then portioned into small aliquots, using 0.05 M HCl as solvent. All peptide aliquots prepared in that way could be dissolved in buffer by mixing the reaction vial for 30 s after adding the desired volume of solvent.

III.3 Lipopeptide Formation via *in situ* Coupling Reaction

A lipopeptide is a hybrid formed of a peptide moiety and a lipid residue, using the latter one as an anchor in lipid bilayers. Since hybrid lipopeptide structures are large moieties, they are usually difficult to incorporate directly into vesicles or membranes, hence we applied an *in situ* coupling reaction, which allowed us to prepare lipopeptides to already formed lipid structures. In Chapter III.3.1 the basic principle of this reaction is explained, while in III.3.2 the actual experimental procedure is described.

III.3.1 Theory of Lipopeptide Formation

The peptides in this work all bear a C-terminal cysteine moiety which allows the coupling to lipid bilayers. Therefore, headgroup modified phospholipids, containing a maleimide residue, were used as receptor lipids (MCC phospholipids, see Chapter III.1.2). The lipopeptide is formed via an addition of the sulfide moiety to the double bond of the maleimide function, under formation of a new covalent carbon-sulfur bond (40). An advantage of this method is that the formed hybrid structure is accessible for successive reactions, like coiled-coil formation (see Fig. III.11).

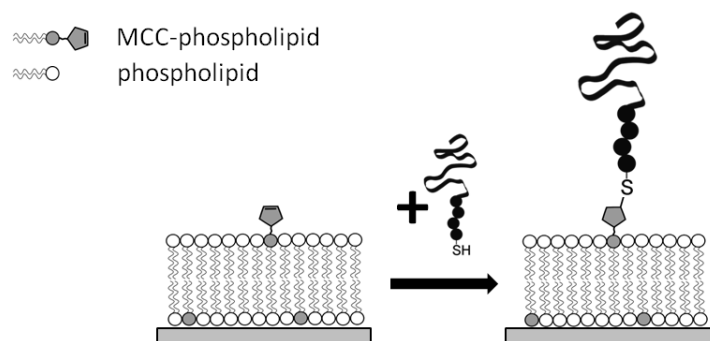


FIGURE III.11 Schematic drawing of *in situ* coupling reaction between MCC-phospholipid and cysteine-containing peptide on a SSM (solid supported membrane).

The reaction can be carried out at room temperature in aqueous solutions like buffers, however in this work it turned out that the presence of ions is crucial ($c \geq 20$ mM). Considering that employed peptides as well as employed anchor lipids both are charged at physiological pH, this is probably due to the shielding effect of present ions. The mechanism of the *in situ* coupling reaction follows a Michael addition. This reaction actually requires the addition of a base, which deprotonates the Michael donor producing a soft nucleophile as reagent. In our case, the reaction can be carried out at neutral conditions (pH 6.8), because the sulfide moiety of the cysteine residue is already partially deprotonated ($pK_s(\text{Cys-SH}) = 8.14$).⁹

In Figure III.12 the chemical structures of the resulting lipopeptides, namely the hybrids formed of MCCDOPE with *i*-K3Cys and *i*-K3PEG, respectively, are shown below.

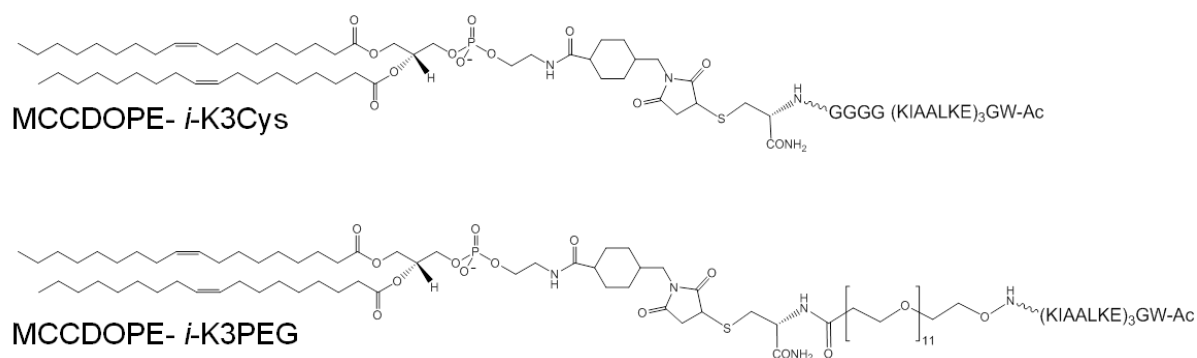


FIGURE III.12 Chemical structures of hybrid lipopeptides formed of MCCDOPE as lipid moiety with *i*-K3Cys and *i*-K3PEG, respectively.

⁹ CRC Handbook of Chemistry and Physics, Ed. D.R. Lide, 85th Ed., CRC Press, Boca Raton, FL, 2005.

III.3.2 Experimental Procedures and Removal of Excess Peptide

In general, *in situ* coupling reaction was carried out using a high excess of peptide, namely 3-10 eq. in comparison to the offered amount of receptor lipids. Therefore, after successful formation of lipopeptides, residual free peptides had to be removed from the sample. The procedures, considering the two different used lipid preparations, are explained in the following section.

III.3.2.1 Functionalization of Solid Supported Membranes

Solid supported membranes (SSM) were functionalized after successful bilayer spreading. After removal of the excess vesicles by rinsing, the peptide was added in buffer to the SSM in a concentration of 25-70 μM , considering the amount of receptor lipids in the spreaded SSM. In general, the used buffer was PB 6.8 (50 mM Na_2HPO_4 , pH 6.8), but could be replaced by any buffer used in this work without further modifications of the functionalization protocol. However, the *in situ* coupling reaction was not feasible in pure water; a small amount of salt was needed ($c \geq 20$ mM). After an incubation time of 1 h for K-peptides and 2-3 h for E-peptides, the SSM was thoroughly rinsed with buffer to remove excess peptide. If the SSM was functionalized with a complete coiled-coil structure, the second peptide was added to the surface in the same concentration (25-70 μM). The incubation time can be shortened to 30 min, until excess peptide is removed by thoroughly rinsing the sample.

III.3.2.2 Functionalization of Vesicles

For the functionalization of vesicles (SUV or LUV) 25-50 μM of peptide was added to the vesicle solution (0.25-0.50 mg of lipid) to give a final volume of 1 mL. The lower amount of peptide in comparison to SSM functionalization can be explained by the lower concentration of receptor lipids in the membrane. A maximum of 3 mol% of MCCDOPE was used for vesicle functionalization, because higher peptide coverage leads to vesicle aggregation and precipitation due to the highly charged surfaces. After an incubation time of 1 h for K-peptides and 2-3 h for E-peptides, excess peptide was removed by size exclusion column chromatography (SEC) using sephadex NAP-25 columns (illustra, GE Healthcare, Solingen, Germany) (see Fig. III.13). This method also allows a buffer exchange of the solution surrounding the vesicles.

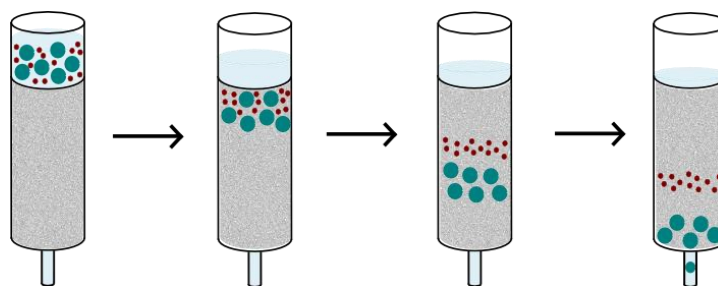


FIGURE III.13 Principle of size exclusion chromatography (SEC) applied for vesicle purification. The grey filling is the stationary phase, the blue phase on top depicts the employed elution buffer. Vesicles are shown in dark blue, small molecules (e.g. excess peptides or buffer ingredients) which were removed are shown as red dots.

In SEC, smaller particles like excess peptides or buffer ingredients can interact with the porous stationary phase, while bigger particles like vesicles cannot diffuse into the pores and hence elute faster. Thereby, the column is washed with 30-50 mL of buffer in which the vesicles finally should be present to remove all impurities and to equilibrate the column. Afterwards, the reaction mixture of vesicles and peptides ($V = 1$ mL) is added and allowed to sink into the stationary phase. The dead volume of the used column is 2.5 mL, thus after loading the sample onto the gel, another 1.5 mL buffer is added and again allowed to sink, whereupon the final elution step is carried out by adding 2.5 mL of solvent to the column. From this point on, fractions are collected until 2.5 mL are eluted. If fluorescently labeled vesicles were used, the detection of the fraction with the analyte can be done visually; otherwise UV/Vis absorbance spectroscopy can be employed. Here, the fractions with the peptide-labeled vesicles are identified by focusing on the absorbance of the peptide bond ($\lambda = 190$ -230 nm). For lipopeptide-decorated vesicles in this work, elution started after ≈ 1 mL and lasted until a volume of about 1 mL was collected (see Fig. III.14).

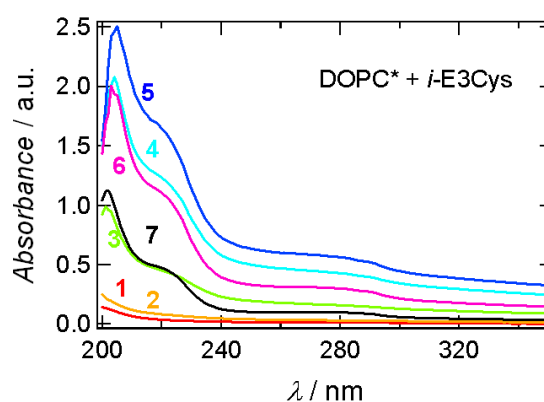


FIGURE III.14 UV/Vis absorption spectra of *i*-E3Cys labeled vesicles. The eluted 2.5 mL were collected in 8 fractions (8th not shown here). The highest concentration of peptide coupled to SUV was found in fractions 4-6.

III.4 Further Materials

Additional materials were applied in this thesis: the chemicals described here were used as detection agents, like the fluorophores mentioned in Chapter III.4.1, or solvent, namely the buffers described afterwards (see Chapter III.4.2).

III.4.1 Fluorophores

III.4.1.1 Sulforhodamine B

Sulforhodamine B (SRB; $M = 558.67$ g/mol; 2-(3-diethylamino-6-diethylazaniumylidene-xanthen-9-yl)-5-sulfo-benzenesulfonate) is a small water-soluble molecule which exhibits red fluorescence (purchased at Sigma-Aldrich, Seelze, Germany) (see Fig. III.15). An advantage of this dye is that its fluorescence activity is pH independent within a range of pH 3-10. The absorption takes place at $\lambda = 565$ nm, while the emission can be detected at $\lambda = 585$ nm. In this work, it was applied as a dye used in content fusion assays, *i.e.* sulforhodamin B (SRB) was encapsulated in vesicles. A potential fusion, correlated to vesicle size, could be detected because SRB exhibits a linear concentration quenching following a Stern-Volmer equation (see Chapter IV.7 and eq. IV.21), with a Stern-Volmer constant $K_{SV} = 990$ M⁻¹ (58).

III.4.1.2 Oregon Green 488 Maleimide

Oregon Green 488 Maleimide (OG488; $M = 463.35$ g/mol; Invitrogen, Darmstadt, Germany) exhibits a green fluorescence with an absorption maximum at $\lambda = 496$ nm and an emission at $\lambda = 524$ nm (see Fig. III.15).

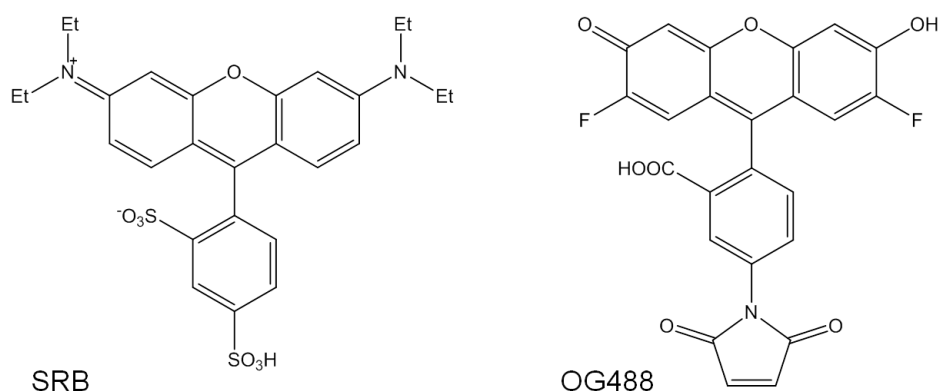


FIGURE III.15 Chemical structures of Sulforhodamin B (SRB) and Oregon Green 488 maleimide (OG488).

As sulforhodamin B, OG488 shows a pH insensitive fluorescence in physiological pH range. It was used in this thesis to carry out a subsequent peptide-labeling to already formed coiled-coil structures on membranes, which is possible due to its maleimide moiety (compare with Chapter III.3). Furthermore, it is not photostable enabling studies considering lateral dynamics carried out with fluorescence recovery after photobleaching experiments (FRAP).

III.4.2 Buffers

All experiments were usually carried out in buffered solutions. A buffer is an aqueous solution containing a weak acid with its corresponding base and therefore stabilizes a specific pH range. In some experiments carried out with IR spectrometer, the aqueous solution was replaced by D₂O to avoid interference signal derived from hydroxyl functions. In this case, only small amounts of salt were added, hence no buffered solution was present. A list of used solvents is given in table III.5, which were all filtered ($\phi_{\text{pores}} = 0.2 \mu\text{m}$) and degassed before usage:

name	composition	pH	application
PB 6.8	50 mM Na ₂ HPO ₄	6.8	standard buffer
HEPES 7.4	20 mM HEPES 150 mM KCl	7.4	vesicle fusion assay (content mixing)
HEPES 7.4 +SRB	20 mM HEPES 20 mM Sulforhodamine B 130 mM KCl	7.4	vesicle fusion assay (content mixing, encapsulated in vesicles)
D ₂ O ^{NaCl/KCl}	50-120 mM NaCl or KCl	n.a.	IR spectroscopy

TABLE III.5 Name, composition, pH and application of employed working solutions.

IV Instrumentation and Data Analysis

Several methods common in biophysical chemistry were employed in this thesis which enabled us to draw a complete picture of peptide-peptide, peptide-membrane, and also peptide-mediated membrane-membrane interactions. Hereby, spectroscopic based methods emerged as useful approaches. IR (see Chapter IV.1) and UV/Vis spectroscopy (see Chapter IV.2), named after their characteristic employed wavelength ranges, namely infrared (IR), ultraviolet (UV), and visual (Vis) light, as well as the extension of the latter one, CD spectroscopy (circular dichroism; see Chapter IV.2), were applied to obtain structural insights of the samples. Furthermore, surface plasmon resonance spectroscopy (SPR; see Chapter IV.3) was used to access the thermodynamics and kinetics of peptide-peptide recognitions. Membrane characteristics like height and mobility changes or fusion could be determined by means of time-resolved ellipsometry (see Chapter IV.4), high resolution imaging by atomic force microscopy (AFM; see Chapter IV.5), fluorescence recovery after photobleaching (FRAP, see Chapter IV.6), and fluorescence based fusion assays (see Chapter IV.7).

IV.1 Fourier Transform Infrared Spectroscopy (FT IR)

This spectroscopic method allows addressing the interaction of light in mid-infrared (IR) range ($\lambda = 2.5\text{-}25\ \mu\text{m}$) with matter. Due to different setup arrangements, solution or surface based analysis can be carried out. In Chapter IV.1.1, a brief introduction into the theory is given, while in IV.1.2 the data analysis concerning the employed materials is explained. A detailed experimental description can be found in Chapter IV.1.3.

IV.1.1 Transmission and Attenuated Total Reflection FT IR Spectroscopy

The absorption of light in the mid-IR range excites vibrations of atoms and atom groups along their bonds, which is employed in IR spectroscopy. The improvement of this technique by Fourier transformation (FT) allows for shortened measuring times which improves the signal-to-noise ratio dramatically (*Multiplex or Fellgett advantage*). Furthermore, due to the fact that no polarizer or monochromator is needed in the setup, the number of slits in the light path is reduced and therefore the energy throughput is increased (*Throughput or Jacquinot advantage*) (59). In FT IR spectroscopy, the absorption for specific wavelengths is carried out simultaneously by the means of a Michelson interferometer and afterwards Fourier transformed, which allows

the spectral presentation of data (60). This actually increases the spectral resolution for FT IR spectroscopy setups in comparison to dispersive setups, since this internal wavelength calibration is achieved via a stable HeNe laser (*Connes advantage*). Also, due to the setup geometry, where the sample is located behind the interferometer, stray light is reduced and can be neglected in this technique (59).

Two different setups to carry out FT IR spectroscopy were employed in this thesis: a transmission measurement cell for fluids, where the IR beam gets through a sample solution, and a measurement cell which takes advantage of the attenuated total reflection (ATR) of the IR beam (see Fig. IV.1).

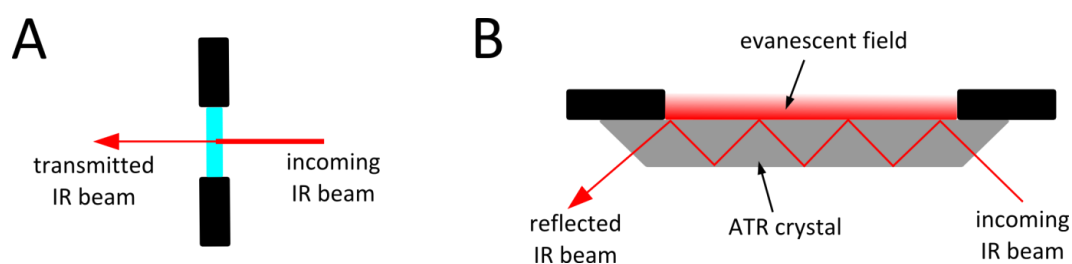


FIGURE IV.1 Schematic drawing of IR beam path in (A) transmission FT IR and on a (B) ATR crystal with formation of an evanescent field. Red line indicates IR beam which is total reflected at the ATR crystal.

In transmission FT IR spectroscopy, the absorption due to the present molecules in the sample is detected, hence the peak heights and area are correlating with the amount of chromophores. In ATR-FT IR, only the molecules in the evanescent field are excited. The total reflection of the IR beam is due to the high refractive index of the ATR crystal, usually consisting of Germanium, Diamond or zinc selenide. The evanescent field propagates with exponential decaying intensity from the ATR crystal surface in the measurement chamber exhibiting a specific penetration depth d_p (see eq. IV.1).

$$d_p = \lambda \cdot \left[2\pi n_1 \sqrt{\sin^2 \theta - \left(\frac{n_2}{n_1} \right)^2} \right]^{-1} \quad (\text{IV.1})$$

Here, the refractive indices n_1 of the ATR crystal and n_2 of the sample are related to the angle of incidence θ . Furthermore, it is obvious that the penetration depth scales linearly with the used wavelength λ ; thus for the spectral presentation of the data, an ATR correction has to be carried out applying the supplier's software OPUS (Bruker Optics, Ettlingen, Germany). In the setup used in this thesis the penetration depth can be calculated to be $\approx 1 \mu\text{m}$. Therefore, molecules which are close to the surface of the refracting material are detected with higher intensity, resulting in

the advantage that overlaying solvent molecules are contributing to the spectra with lower intensity, as long as the ATR crystal is fully covered with sample material.

IV.1.2 Analysis of Protein and Lipid Spectra

Generally, IR active molecules need to have a changing dipole, *e.g.* a permanent or an oscillating dipole, where the latter one has its origin in a non-symmetrical moiety. In this thesis, phospholipids and peptides were analyzed (for reviews concerning this topic see (61, 62)). Those rather large molecules exhibit several IR active groups, however, for lipids the stretching vibrations in the range of 2800-3050 cm^{-1} (see Fig. IV.2) and for peptides the amide I band (1600-1700 cm^{-1}) are the most prominent ones.

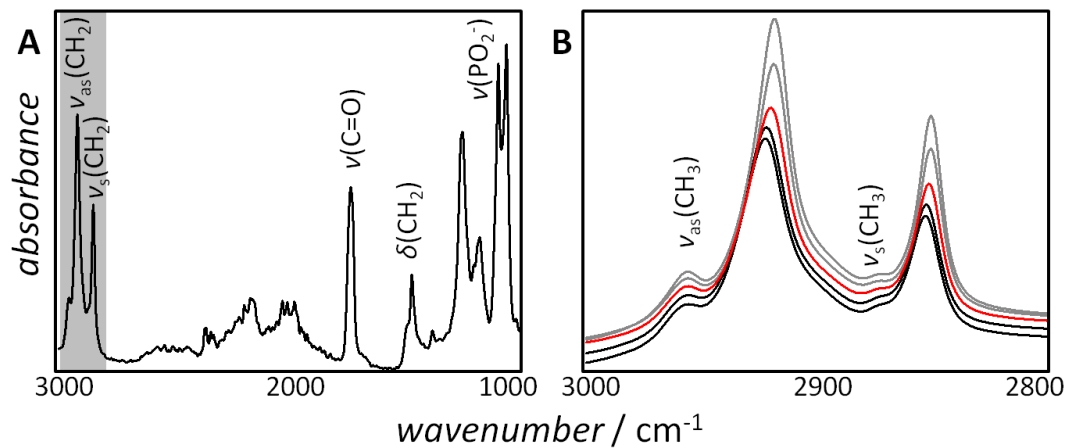


FIGURE IV.2 ATR-FT IR spectra of lipids with its characteristic vibrations. (A) POPC at room temperature with marked stretching vibrations ν and bending vibrations δ . Area highlighted in grey depicts stretching vibrations sensitive to the lipid phase. (B) DPPC in a temperature range of 34-50 °C. Red spectrum is recorded at $T_m(\text{DPPC}) = 42$ °C, black spectra are collected at $T > 42$ °C, and grey spectra are collected at $T < 42$ °C. Stretching vibrations of $-\text{CH}_3$ moieties are marked here due to better visibility.

Besides carbonyl and phosphate moieties, phospholipids display high IR absorbance due to the alkyl chains of fatty acid residues. Here, a bending vibration δ can be found ≈ 1500 cm^{-1} whereas asymmetrical and symmetrical stretching vibrations (ν_{as} and ν_{s}) are present in the range of 2800-3050 cm^{-1} (see Fig. IV.2). The latter one is sensitive to the gel- to fluid-phase transition, as the packing density has an influence on the position of the peak maxima (see Fig. IV.2, B). It can be seen that the terminal $-\text{CH}_3$ moieties are not influenced by temperature changes, but the main peaks originating from the alkyl chains $-\text{CH}_2-$ shift by 2.5 cm^{-1} to higher wavenumbers while heating a sample and crossing the phase transition temperature (63).

Peptides and proteins generally show lots of IR active bonds, but here the focus lies on the most prominent amide I band existing in a range of 1600-1700 cm^{-1} (64). Since this signal has its origin in the stretching vibration of the carbonyl moiety, which are participating in secondary structure stabilization, this peak is sensible to conformation changes (see Fig. IV.3).

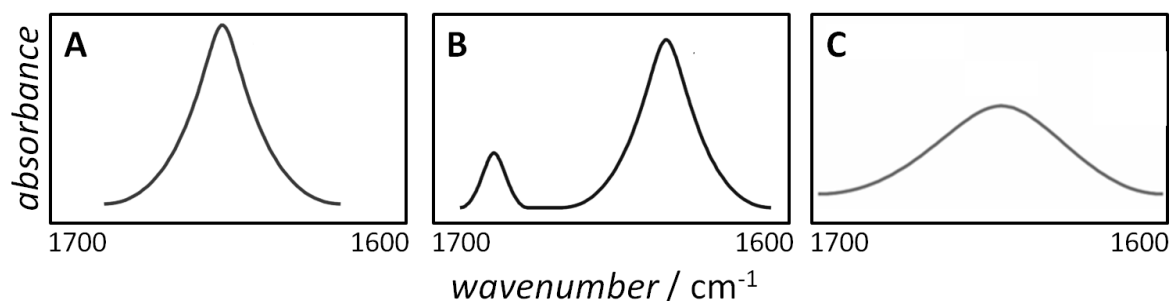


FIGURE IV.3 Schematic drawings of amide I band in FT IR spectra consisting of (A) α -helix, (B) β -sheet, and (C) random coil.

While mainly α -helical structures display a sharp peak with a maximum at $\approx 1652 \text{ cm}^{-1}$, random coils show a broadened spectrum with a local maximum shifted to lower wavenumbers ($\approx 1645 \text{ cm}^{-1}$). In contrast, β -sheets present a splitted amide I band, where two peaks with maxima at $\approx 1630 \text{ cm}^{-1}$ and $\approx 1680 \text{ cm}^{-1}$ occur. With the supplier's software, a fit function can be applied to measured peptide and protein spectra to determine the percentage of according secondary structures and the amount of sample in the measurement cell (QUANT2 analyses, OPUS, Bruker Optics, Ettlingen, Germany). Here, the experimental data is compared to an internal calibration data set. Since calibration data is recorded with aqueous solutions in a transmission FT IR cell, results from experimental data which were collected differently can be only applied for qualitative comparisons and should not be handled as quantitative outcome.

In coiled-coil proteins and peptides, the peak maximum is shifted to lower wavenumbers in comparison to simple α -helical structures (65). Furthermore, those bands exhibit a special pattern because the actual main peak is consisting of at least three separable bands which can be isolated by applying a deconvolution (66, 67). Therefore, a second derivative of the spectral data is formed with the supplier's software to define the peak positions (OPUS, Bruker Optics, Ettlingen, Germany), followed by rebuilding the main amide I band by fitting multiple Gaussian functions with their maxima at the defined locations (Origin 8.0 Pro, OriginLab Corporation, Northampton, MA, USA).

IV.1.3 Experimental Procedures

Peptides used for IR measurements were lyophilized 5× from 0.05 M HCl to replace trifluoroacetate counterions at peptide backbone with chloride ions (57). All experiments were carried out in D₂O containing ≈ 50 mM of salt, *e.g.* NaCl. Spectra were acquired using a Vertex 70 FT IR (Bruker Optics, Ettlingen, Germany) spectrometer equipped with a MCT (mercury cadmium tellurium) detector at a resolution of 2 cm⁻¹. Measurement times for background and data were generally set to 0.5 min.

IV.1.3.1 Transmission FT IR Spectroscopy

Applied measurement cell was a flow-through AquaSpec micro transmission cell with a path length of 7 μm. Samples were dissolved and injected to the cell. The actual volume of sample in the measurement cell is ≈ 5 μL, however for the injection procedure 30-50 μL are needed. QUANT2 analyses can be applied to the data to determine secondary structure percentages or protein concentrations with high accuracy, since the internal calibration data is collected with similar setups. After measurement, the cell was rinsed with buffer, water and finally dried as good as possible by injecting air.

IV.1.3.2 ATR-FT IR Spectroscopy

Peptide-functionalized SSM were measured in a closed fluid chamber using a ZnSe ATR IR crystal coated with a thin layer of Si (BioATR II, Bruker Optics, Ettlingen, Germany). First, background spectra were collected to ensure a stable baseline. Then, SUV solutions ($c_{\text{lipid}} = 1 \text{ mg/mL}$) are injected onto the ATR crystal and incubated for 30 min above phase transition temperature of lipids present. After rinsing, peptides were added ($c_{\text{peptide}} = 50\text{-}100 \text{ μM}$) and incubated on the formed SSM for 1 h. ATR-FT IR measurements were carried out with sample volumes of 10-30 μL and after each step, measurement cell was rinsed 10× with 10-30 μL buffer to remove excess material. The measurement cell can be also used as a flow-through setup; therefore a pump with in- and outlet was connected and rinsing steps were carried out for at least 5 min.

IV.2 Absorbance Spectroscopy with Ultraviolet and Visual Light

UV/Vis spectroscopy is a very basic analytic method, which determines the absorption of a sample in the ultraviolet to visual light range. This method enables the measurement of protein concentrations, while its dichroic counterpart, the circular dichroism (CD) spectroscopy

focuses mainly on structural analysis of protein and peptides samples. In the first part of this chapter (IV.2.1), a short introduction to the theoretical setup is given, while then the main focus lies on data analysis (IV.2.2). The experimental procedures are given in Chapter IV.2.3.

IV.2.1 Theory of UV/Vis and CD Spectroscopy

In absorption spectroscopy, light is guided through the sample and the amount of absorbed light is defined, which can be described with the law of Lambert-Beer (see eq. IV.2) (60):

$$A = \lg \frac{I_0}{I} = \varepsilon cd \quad (\text{IV.2})$$

Hereby, the absorbance A is defined as logarithmic ratio of irradiated light intensity I_0 and transmitted light intensity I . It can be further described as the product of path length d , chromophore concentration c , and the sample specific extinction coefficient ε .

The basic setup of absorption spectrometers is given in Figure IV.4 and consists necessarily of a light source, a monochromator, and a detector. The light source emits wavelengths between $\lambda = 200\text{--}1100$ nm, which are separated with the monochromator. The sample absorbs energy as a function of its containing chromophores. The remaining transmitted light intensity is finally detected.

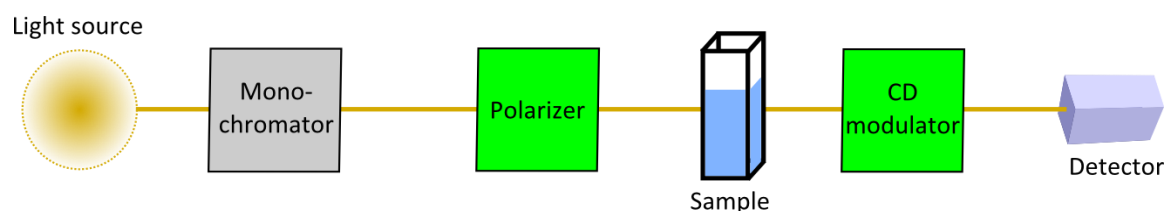


FIGURE IV.4 Scheme of an absorption spectrometer. In UV/Vis spectroscopy only light source, monochromator, sample, and detector are connected in series, while for a CD spectrometer the green marked polarizer and CD modulator are added to the setup.

In CD spectroscopy, the setup is extended by a polarizer and a CD modulator. Since circular dichroism refers to the different absorption of right- and left-circular polarized light, the emitted unpolarized light from the light source has to be transformed. Therefore, the polarizer works like a filter where only linear polarized light can pass through. In the CD modulator, a $\lambda/4$ -plate is used to produce circular polarized light. By rotating the $\lambda/4$ -plate right- and left-circular polarized light is generated.

If chiral chromophores are present in the sample, left- and right-circularly polarized components of emitted light will be absorbed differently. Chirality is due to the covalently linked structure, the overall orientation of the molecule or the placement in an asymmetric environment (68, 69). Since the peptide bond in proteins exhibits an optical activity, and stabilizes the folding of proteins, CD spectroscopy is employed for secondary structure analysis (70). The difference $\Delta\varepsilon = \varepsilon_L - \varepsilon_R$, actually called circular dichroism, is the determined parameter. However, in experimental setups the ellipticity θ is measured (see eq. IV.3):

$$\theta = \ln 10 \frac{180^\circ}{4\pi} (\varepsilon_L - \varepsilon_R) \cdot c \cdot d \approx 33^\circ \cdot \Delta\varepsilon \cdot c \cdot d \quad (\text{IV.3})$$

IV.2.2 Data Analysis

By the means of UV/Vis spectroscopy, concentrations can be determined employing the law of Lambert-Beer, provided that an extinction coefficient is known. How ε can be estimated for protein and peptide samples is described in the following section. Afterwards, it will be explained how CD spectroscopy provides an insight into secondary structure determination as well as kinetic information.

IV.2.2.1 UV/Vis Spectroscopy

Following the law of Lambert-Beer, a concentration c can be calculated from the measured absorbance A with a given path length d and a defined extinction coefficient ε , whereupon the path length is usually known from the geometry of the employed cuvette. In Table IV.1 absorbance maxima λ_{\max} and extinction coefficients for chromophores used in this thesis are summarized (60, 71):

chromophore	$\lambda_{\max} / \text{nm}$	$\varepsilon / \text{M}^{-1} \text{cm}^{-1}$
peptide bond	190 ($\pi \rightarrow \pi^*$)	7000
	220 ($n \rightarrow \pi^*$)	100
tryptophan	219	47000
	280	5500
cysteine	280	125

TABLE IV.1 Summarized absorbance maxima λ_{\max} and corresponding extinction coefficients ε for chromophores used in this thesis (60, 71).

The peptide bond itself shows a specific absorbance at 220 nm, which makes it a suitable wavelength just for identifying peptide moieties by the means of absorption spectroscopy.

Furthermore, the peptides used in this thesis are all marked with tryptophan as a spectroscopic probe. For an exact concentration determination, the absorption at $\lambda = 280$ nm is employed. For peptides and proteins, a specific extinction coefficient can be estimated as long as the primary sequence is known, because ϵ for a sample consisting of different chromophores is equal to the sum of present extinction coefficients. In proteins and peptides the only absorbing moieties at 280 nm are tryptophan, tyrosine, and cysteine with extinction coefficients presented in eq. IV.4 (71).

$$\epsilon_{280nm} = n_{Trp} \cdot 5500M^{-1}cm^{-1} + n_{Tyr} \cdot 1490M^{-1}cm^{-1} + n_{Cys} \cdot 125M^{-1}cm^{-1} \quad (IV.4)$$

Since in all synthesized E- and K-peptides, employed in this thesis the number of chromophores can be given with $n_{Trp} = n_{Cys} = 1$ and $n_{Tyr} = 0$, their specific molar extinction coefficient is calculated to be $5625 M^{-1}cm^{-1}$.

IV.2.2.2 CD Spectroscopy

The determined ellipticity θ (see eq. IV.3) is usually converted to the mean residue weight ellipticity $[\theta]_{MRW}$, which is normalized to the number of optical active residues in the sample (see eq. IV.5):

$$[\theta]_{MRW} = \frac{\theta \cdot M}{10 \cdot c \cdot d \cdot N_{aa}} \quad (IV.5)$$

Due to historical reasons, this normalization is not accomplished under consideration of SI-units, hence the parameters has to be given in specific units to calculate a correct $[\theta]_{MRW}$ (in $\text{deg} \times \text{cm}^2 \times \text{dmol}^{-1}$):

- θ : ellipticity / mdeg
- M : molar weight / $\text{g} \times \text{mol}^{-1}$
- c : concentration / $\text{mg} \times \text{mL}^{-1}$
- d : path length / cm
- N_{aa} : number of amino acids present in sample

The measured spectra of different proteins display characteristic curves which depend on their secondary structure (see Fig. IV.5) and were subsequently analyzed by fitting the data employing *DichroWeb*, an online analysis database for CD spectra (72, 73). Within this server, several common empirical algorithms can be accessed and applied for the secondary structure calculation. These algorithms usually base upon reference sets, comparing CD spectra of

proteins with known structure. In this work, all spectra were analyzed with good accuracy using the K2d algorithm (74). An additional advantage of *DichroWeb*, beside the access to various analysis databases, was the user-friendly interface which enabled the input of data without time-consuming pre-analysis processing and conversion of data.

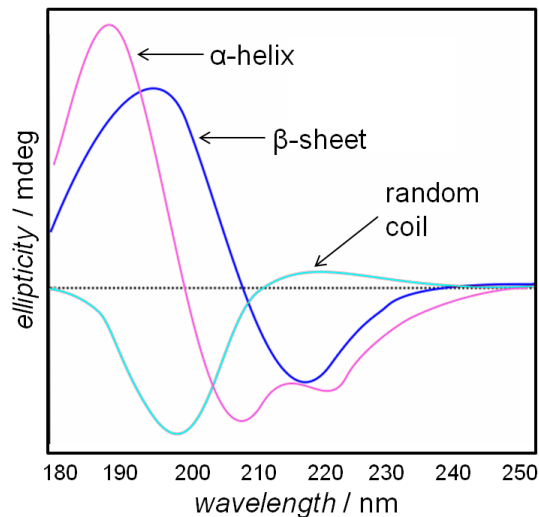


FIGURE IV.5 Schematic drawing of CD spectra from proteins with mainly α -helical (pink), β -sheet (blue) and random structure (light blue). Scattered line indicates ellipticity of 0.¹⁰

In this thesis especially the α -helical content of peptides and proteins was of interest, hence we focused mainly on the local maximum at around 190 nm and the two local minima at 208 nm and 220 nm. The latter one can be also used to determine a kinetic constant, namely the dissociation constant K_D , of dimeric coiled-coil complexes by dilution experiments. Here, successively reducing a known peptide concentration c leads to a dissociation of assemblies, which results in the special case for coiled-coil forming peptides in a corresponding decrease of the α -helix content (75). The change in ellipticity at 220 nm $[\theta]_{220nm}$ is described by eq. IV.6:

$$[\theta]_{220nm} = \frac{1}{4c} \left([\theta]_{mon} \sqrt{K_D^2 + 8cK_D} - \sqrt{[\theta]_{cc} K_D^2 + 8cK_D} + K_D ([\theta]_{cc} - [\theta]_{mon}) + 4[\theta]_{cc} c \right) \quad (IV.6)$$

Besides the dissociation constant K_D as the fit parameter, the ellipticity for a monomeric unfolded peptide ($[\theta]_{mon}$) and the maximum ellipticity for a complete coiled-coil structure ($[\theta]_{cc}$) need to be specified, which can be achieved by fitting or by extracting the relevant data from appropriate CD spectra.

¹⁰ Figure redrawn from <http://mach7.bluehill.com/proteinc/cd/cdspec.html> (02. 08. 2012)

IV.2.3 Experimental Procedures

For both measurements, glass cuvettes were employed. While for UV/Vis spectroscopy, the path length was 10 mm, in CD spectroscopy a smaller cuvette with 1 mm path length was used.

IV.2.3.1 UV/Vis Spectroscopy

Buffer solution served as a reference and cuvettes were rinsed with buffer and sample solution was filled in. Afterwards, absorbance was measured at fixed wavelength ($\lambda = 280$ nm) for concentration estimation experiments. Otherwise a spectra ranging from ≈ 200 -600 nm was collected. Measurements were carried out using an UV/Vis spectrometer Cary50 (Varian, Darmstadt, Germany).

IV.2.3.2 CD Spectroscopy

Peptides were dissolved in PB 6.8 (which was measured as background sample) and concentrations were checked via UV/Vis spectroscopy as described above. Measurements were carried out using a JASCO-810 spectrometer (Gross-Umstadt, Germany). Spectra were accumulated (3 \times), averaged and background corrected (data range $\lambda = 190$ -250 nm; scanning speed 10 nm/min; data pitch 0.1 nm) with peptide concentrations ranging from 1-100 μ M. For dilution experiments, 60-100 data points at fixed wavelength were collected and averaged (75).

IV.3 Surface Plasmon Resonance Spectroscopy

The surface plasmon resonance spectroscopy technique, short SPR spectroscopy, was employed with a single wavelength setup, hence no spectra are recorded. Otherwise, it enabled the collection of time-dependent processes used for kinetic analysis of binding studies (for review see Homola *et al.* 1999 (76)). The theory and the corresponding data analysis behind the technique are shortly described in Chapter IV.3.1 and IV.3.2 while in IV.3.3 a detailed experimental description is given.

IV.3.1 Theory

In SPR spectroscopy, surface plasmons are produced at the boundary layer of thin metal surface and the analyte. For this purpose, light is totally reflected using a prism resulting in an evanescent field which excites surface plasmons at the metal layer (see Fig. IV.6).

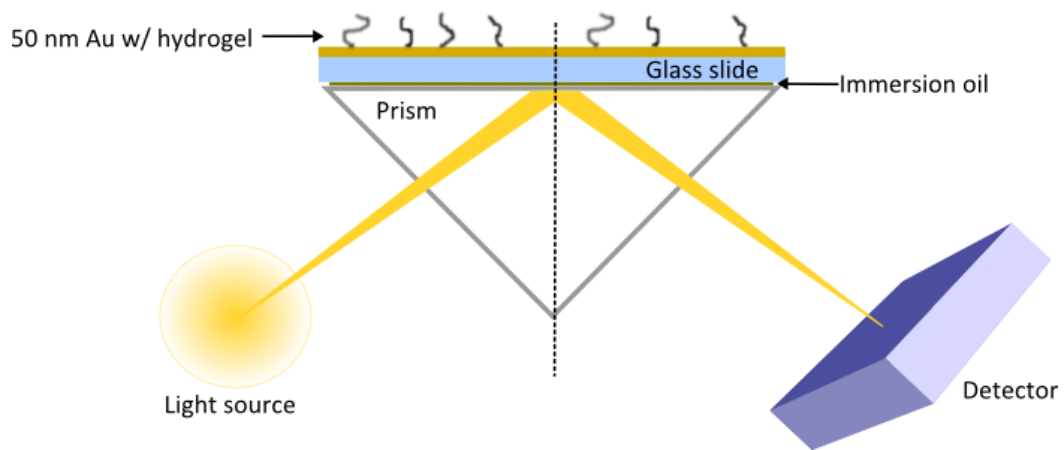


FIGURE IV.6 Schematic drawing of a setup used in surface plasmon resonance (SPR) spectroscopy experiments.

The light from the source has a wavelength of 780 nm and is reflected at the used biosensor chip interface, which is in our setup a glass slide covered with a 50 nm gold layer and fixed on the prism with immersion oil. Upon reflection, the light containing a minimum at a specific angle of reflectivity is detected. When now material is brought into contact with the gold surface, this changes the dielectric permittivity and an angular shift occurs. Furthermore, the refractive index of the sample close to the gold surface is affected, which can be determined as relative change in index of refraction, short RIU, also often referred to as response units.

In our setup, the gold covered chip was functionalized with a wide-meshed hydrogel, where the analyte was coupled to. This hydrogel swells in buffer until a thickness of up to 200 nm is reached and therefore intensity of SPR signal is enhanced. Furthermore, a parallel measurement of reference and sample is enabled due to special separated measurement chamber geometry.

In SPR experiments, a flow cell setup is employed, with the actual measurement chamber connected to a computer controlled valve system. In a kinetic experiment carried out by such a flow setup, the response of the SPR signal is collected in a time-dependent manner, while a binding partner is added to the system resulting in an increase of response during association phase (see Fig. IV.7).

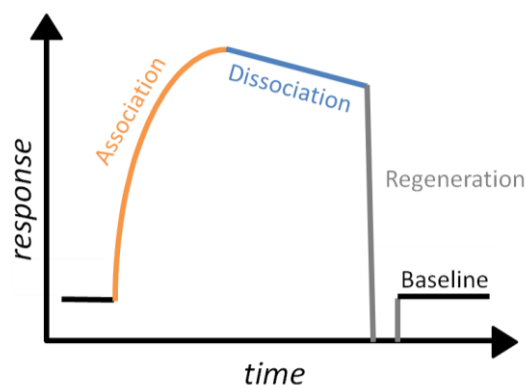


FIGURE IV.7 Schematic drawing of signal recorded in SPR spectroscopy while association and dissociation of an analyte, followed by a regeneration step until baseline is reached again.

At the end of association phase, a buffer flow is directed over the surface, resulting in a dissociation phase, which is characterized by a decrease of SPR signal. After a regeneration phase and a recovery of a stable baseline, another association-dissociation cycle can be carried out.

IV.3.2. Data Analysis

Since with SPR, association and dissociation phases of molecular interaction are monitored, on- and off-rates of binding processes, k_{on} and k_{off} , can be determined. In this work, the association of peptide while coiled-coil formation could be best described by a double exponential fit to determine τ_a (see eq. IV.7) and dissociation phase is fitted with an exponential fit yielding the time constant τ_d (see eq. IV.8).

$$I = I_0 + A_a \exp\left(\frac{-(t-t_0)}{\tau_a}\right) + A_b \exp\left(\frac{-(t-t_0)}{\tau_b}\right) \quad (IV.7)$$

$$I = I_0 + A_d \exp\left(\frac{-(t-t_0)}{\tau_d}\right) \quad (IV.8)$$

The applied functions both display an offset in their abscissa as well as in their ordinate. Hence, the detected intensity of the SPR signal I and time t are normalized concerning the starting point by determination of the parameters I_0 and t_0 . With A as specific additional fit parameter, time constants τ_a , τ_b , and τ_d are defined in this analysis step. The second, slower time constant τ_b determined by the double exponential function can be neglected, since only the first time constant τ_a exhibits solely adsorption processes whereas the slower one is affected by

desorption processes. Using the peptide concentration c of added solution and the fitted time dependencies, binding rates can be calculated (see eq. IV.9 and IV.10):

$$k_{off} = 1/\tau_d \quad (IV.9)$$

$$k_{on} = \frac{(\tau_a)^{-1} - k_{off}}{C_{peptide}} \quad (IV.10)$$

The final dissociation constant K_D is defined by the ratio of dissociation- and association-rate constants k_{off} and k_{on} (see eq. IV.11).

$$K_D = \frac{k_{off}}{k_{on}} \quad (IV.11)$$

Day *et al.* could show 2002 that K_D values determined from measurements in solution and with SPR are in good accordance (77), due to attachment of the probes to a wide-meshed hydrogel. Therefore, in SPR experiments, the sample retains most of its rotational entropic properties and its diffusional freedom (78); therefore the measurement can be in principle treated like a solution based method.

III.3.3 Experimental Procedure

SPR (SR7000DC, Reichert Life Sciences, Seefeld, Germany) measurements were done on a chip, coated with a dense cystamine derivatized bioinert hydrogel matrix consisting of carboxymethyl dextran (THC1000M, XanTec Bioanalytics, Düsseldorf, Germany). Before starting of the experiment, the thiol moieties in the hydrogel had to be reduced and activated, which is described below. All solutions applied had to be filtered through a 0.2 μm porous membrane and degassed. The measurement chamber in the SPR spectrometer divides the used chip into two measurements chambers, which are connected in series, providing the possibility to carry out a reference experiment simultaneously with the actual measurement. K-peptides, being positively charged at the used pH and therefore adherent to surface - which enables binding - were immobilized by disulfide coupling using the following procedure:

- 1) System was rinsed with running buffer (0.1 M phosphate, pH 8.0), the sensor chip was mounted and equilibrated for 10 min in running buffer.
- 2) Reduction buffer (100 mM DTT (dithiothreitol) in running buffer) followed by activation buffer (10 mM pyridyl disulfide in phosphate buffer / ethanol 4:1) was injected to the

system, each step lasting at least 20 min. Between and after these two steps, system was rinsed with running buffer.

- 3) Now the surface is rinsed with water and subsequent with coupling buffer (2 mM sodium acetate, pH 4.0). Afterwards, a K-peptide solution is dissolved in coupling buffer and washed through solely one of the two measurements chambers (20-30 min), which are otherwise connected in series. Here, a significant increase of the detection signal should be observed.
- 4) Capping buffer (1 mM mercaptoethanol and 1 M NaCl in 0.1 M coupling buffer, pH 4.2) is washed through both parts of the measurement chamber, to block remaining thiol groups.

After successful immobilization of K-peptides, E-peptides dissolved in PB 6.8 were added in different concentrations (1-50 μM) and association and dissociation phase were monitored for 300 s each. All binding constants were calculated from at least four different concentrations. Association and dissociation were both monitored for 300 s. Since the E/K complex is not dissociating completely through rinsing, the surface had to be regenerated by washing the system with 10 mM NaOH.

IV.4 Ellipsometry

An ellipsometer is a non-invasive and sensitive measurement technique employing interactions with polarized light, invented in 1945 by Alexandre Rothen based on theories of Paul Drude (79). It enables the determination of thin layer thicknesses in a time-dependent manner. In Chapter IV.4.1 the theory and modeling of this instrument will be briefly explained, afterwards (IV.4.2) adsorption isotherms accessible with this tool are presented. Finally, in Chapter IV.4.3 detailed experimental procedures are given.

IV.4.1 Theory, Setup and Analytical Workup

In this work, a Null-ellipsometer was employed for detection of thin layer thicknesses. Hereby, elliptic polarized light is partially reflected and refracted at a Si-surface in dependence of deposited layers. The ellipticity of the irradiated light is specifically adjusted for every single data point so that always linear polarized light is radiated after reflection and refraction at the sample (see Fig. IV.8) (80).

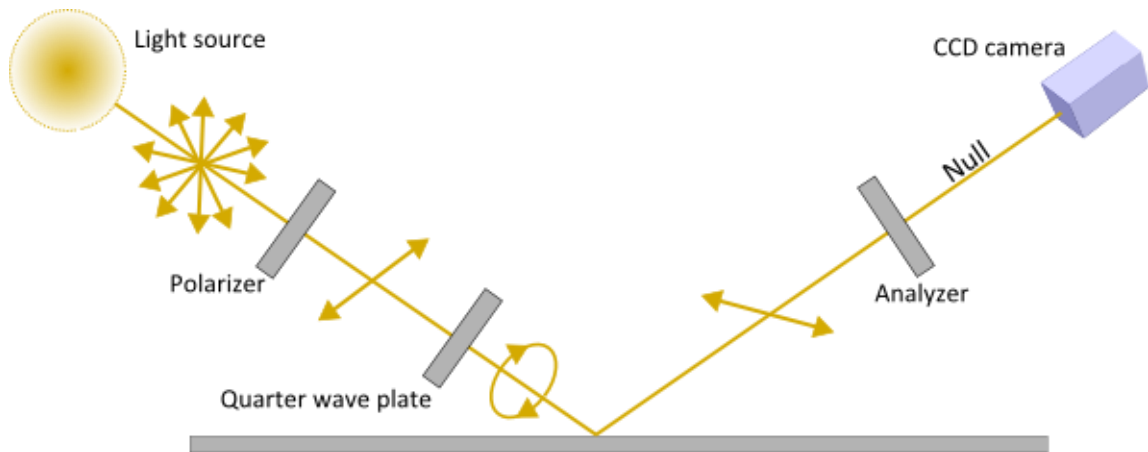


FIGURE IV.8 Schematic drawing of a setup used in a null ellipsometer like it was employed in this work.

In the setup applied in this work, a Nd:YAG laser emits unpolarized and monochromatic ($\lambda = 532 \text{ nm}$) light which is afterwards transformed to linear polarized light (polarizer). After passing through a $\lambda/4$ -plate (quarter wave plate), elliptic polarized light is reflected and refracted at the sample surface in this way that linear polarized light is produced. After passing through an analyzer, which is set to an intensity minimum (“Null”), the light is detected with a CCD camera (charge coupled device camera). The angles applied for the $\lambda/4$ -plate, the polarizer, and the analyzer, are specifically adjusted for every single data point and are used for the calculation of the ellipsometric angles *del* (Δ) and *psi* (Ψ). Those angles are directly related to the ratio ρ of occurring reflectivities perpendicular and parallel to the plane of incidence (see eq. IV.12):

$$\rho = \tan\Psi \cdot \exp^{-i\Delta} \quad (\text{IV.12})$$

For thin layers ($< 50 \text{ nm}$) *del* is linearly decreasing with increasing layer thickness, which is not the case for the angle *psi* (see Fig. IV.9). Hence in some cases the height of deposited layers can be estimated by exclusively using the angle *del* with sufficient accuracy. Hereby, a decrease of 1° *del* is linear related to an increase in layer thickness of $\approx 0.9 \text{ nm}$.

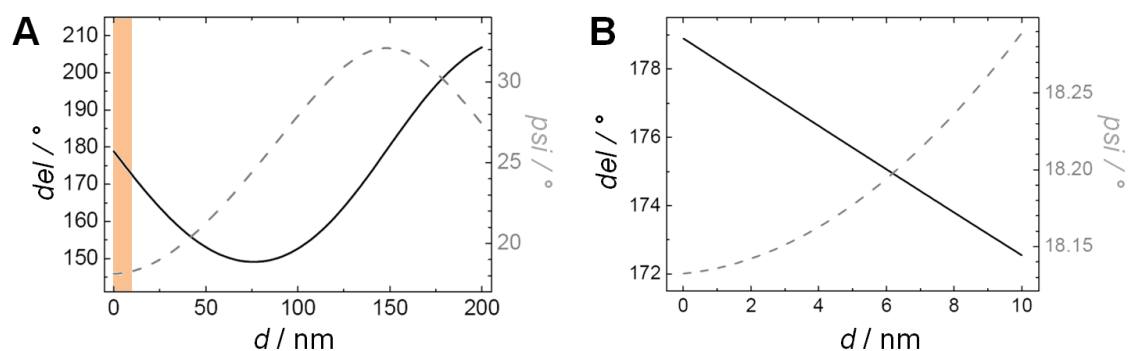


FIGURE IV.9 Simulated dependency of del and psi to layer thickness d in a range of 0-200 nm (A) and a zoom in (orange marked area in A) for thin layers with a thickness of 0-10 nm (B).¹¹

The constant fitting of del and psi and the resulting layer thickness determination is accomplished while measurement with high accuracy applying different modeling procedures. Because at four different angle combinations of polarizer, $\lambda/4$ -plate, and analyzer a “Null” can be adjusted (see Table IV.2), del and psi are able to be determined by carrying out one-zone nulling to up to four-zone nulling procedures, respectively. Kinetic measurements were collected by using simple one-zone nulling procedures to enable a fast time-dependent monitoring, while for precise layer thickness determinations the four-zone nulling procedure was accomplished.

	polarizer P	$\lambda/4$ -plate	analyzer A	del	psi
zone 1	$(-45)^\circ - 135^\circ$	45°	$0 - 90^\circ$	$270^\circ - 2P$	A
zone 2	$135^\circ - 45^\circ$	45°	$(-90)^\circ - 90^\circ$	$90^\circ - 2P$	$-A$
zone 3	$45^\circ - (-135)^\circ$	-45°	$0^\circ - 90^\circ$	$90^\circ + 2P$	A
zone 4	$(-135)^\circ - 135^\circ$	-45°	$(-90)^\circ - 0^\circ$	$270^\circ + 2P$	$-A$

TABLE IV.2 Angles of polarizer, $\lambda/4$ -plate, and analyzer for “Null” adjusting and their dependencies to determined del and psi .

For calculation of height from obtained angles del and psi , an optical model was employed, which contained the specific refractive index of sample material. Therefore, each layer was assumed to be a thin film showing a full coverage. For lipids and peptides, a refractive index of 1.5 was used (81).

IV.4.2 Adsorption Isotherms

Thermodynamic values like dissociation constant K_D can be determined employing ellipsometry by carrying out adsorption isotherms. Hereby, the intensity, in this case the layer thickness h , is measured in a concentration dependent manner. Especially for coiled-coil

¹¹ Figure adapted and modified from Dissertation of Simon Faiss, Mainz, Germany, 2007.

formation on SSM an adsorption process can be assumed, hence theories of Langmuir and Bragg-Williams can be employed for fitting procedures (82). Therefore, the following equations IV.13 representing a Langmuir isotherm and IV.14 for a Bragg-Williams isotherm are used:

$$\Delta h = \frac{h_{\max} \cdot K_D^{-1} \cdot c}{1 + K_D^{-1} \cdot c} \quad (\text{IV.13})$$

$$c = K_D \frac{h/h_{\max}}{1 - h/h_{\max}} \exp \left[\chi \left(1 - 2 \frac{h}{h_{\max}} \right) \right] \quad (\text{IV.14})$$

Both models are suitable for reversible reactions following a monolayer adsorption, which can be assured in the case of coiled-coil formation described here. However, the Langmuir equation neglects a possible interaction of adsorbed molecules, which can be provided by the usage of the Bragg-Williams isotherm. Here, the cooperativity parameter χ is introduced, reflected in the sigmoid shape of the isotherm (see Fig. IV.10).

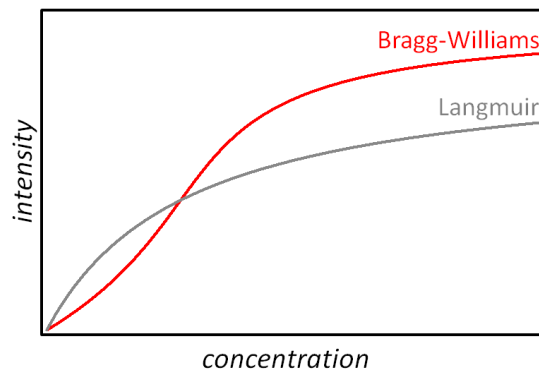


FIGURE IV.10 Exemplarily presentations of isotherms following a Langmuir equation (grey) and a Bragg-Williams equation (red).

With $\chi = 0$ the Bragg-Williams equation is reduced to the Langmuir equation, with $\chi > 0.5$ a significant sigmoid shape of resulting curve is found.

IV.4.3 Experimental Procedures and Analysis

Experiments were performed using an imaging ellipsometer EP³-SW from Accurion (Göttingen, Germany) as described previously (81). Measurements were carried out in PB 6.8 in a closed fluid chamber with a fixed angle of incidence of 60°. Lipid bilayers were spreaded from a SUV solution with a concentration of 0.1 mg/mL on hydrophilized Si wafers with a size of commercially available glass slides. For *in situ* coupling reaction of E-peptides, a concentration of 100-120 μM was used, while for coupling reaction of K-peptides 50-60 μM were sufficient. Before

and after each step, buffer was rinsed through the measurement cell for at least 5 min to remove excess material. If adsorption isotherms should be determined, the concentration of added peptide was slowly increased, with each concentration incubated on the SSM for at least 10 min and without rinsing steps in between. Data was collected with one data point each 10 s applying one-zone nulling measurements. Before and after new layer formation, a four-zone nulling measurement was carried out, followed by a suitable modeling to determine the layer thickness. Conversion of kinetic data displaying angle $\Delta\theta$ against time occurred by assuming the linear relationship $1^\circ \Delta\theta \approx 0.9 \text{ nm}$ at a refractive index of $n = 1.5$.

IV.5 Atomic Force Microscopy

The atomic force microscope (AFM) was first described in 1986 as a modification of the scanning tunneling microscope (83). It enables the imaging of samples in air as well as in solution in the nanometer regime. In Chapter IV.5.1, the theory of the employed AFM and its imaging modes are explained while in Chapter IV.5.2 the experimental procedure is described.

IV.5.1 Theory of Imaging with Atomic Force Microscopy

In atomic force microscopy (AFM) a small tip attached to a cantilever is scanned over a surface to detect topographic as well as mechanic characteristics of the sample. Hereby, a laser is focused on the cantilever tip and its deflection is detected via a 4-quadrants photodiode (see Fig. IV.11, A) (60).

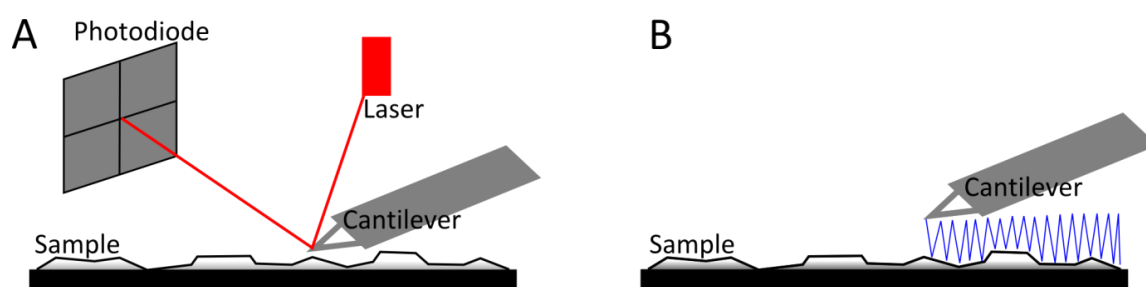


FIGURE IV.11 (A) Schematic drawing of laser reflection on cantilever tip and detection at 4-quadrants photodiode. (B) Schematic presentation of tapping mode for imaging.

Both, cantilever and sample are moved relatively to each other applying piezo elements, whereupon the sample is moved in x-y direction and the cantilever in its height (z-direction).

In Figure IV.11 B, the imaging mode employed in this thesis is presented. Since soft materials like lipid bilayers and peptides were analyzed, tapping mode (also called intermittent-contact mode) was preferred to image those samples instead of the more rigid contact mode, because less force F , described by Hook's Law (see eq. IV.15) is applied to the surface.

$$F = k \cdot z_f \quad (IV.15)$$

Hereby, k is the spring constant of the employed cantilever whereas z_f described its deflection. While contact mode, the cantilever is permanently connected to the surface and its deflection and hence the relative force applied to the sample is kept constant. In intermittent-contact mode, the cantilever is excited with its resonance frequency and therefore scans the surface in a permanently oscillating manner. Hereby, short contact times of tip and sample prevent a damaging of the surface. Furthermore, by measuring the phase shift between exciting and resulting oscillation frequency, material characteristics like rigidity or viscosity of the sample can be resolved.

IV.5.2 Experimental Procedures

AFM images of peptide functionalized SSMs were acquired in liquid using tapping mode of a Nanowizard II atomic force microscope (JPK Instruments, Berlin, Germany). Gold coated MSCT cantilever (Bruker AXS, Camarillo, CA, USA) exhibiting nominal spring constants of 0.05 N/m were employed for imaging by the means of intermittent content mode in PB 6.8 at room temperature using mica as solid support. Bilayer spreading and peptide coupling as well as coiled-coil formation was accomplished as described in Chapter III.1.3 and III.3.2.1. Image processing was accomplished with the supplier's software (JPK SPM Data Processing, JPK Instruments, Berlin, Germany), however grain analysis was carried out employing the open-source software Gwyddion (84).

IV.6 Fluorescence Recovery After Photobleaching

Fluorescence recovery after photobleaching (FRAP) provides the possibility to determine lateral mobility of labeled lipids in membranes. It can be utilized for a whole cell approach as well as for model systems, as in this work. In Chapter IV.6.1 the basic principle and in IV.6.2 the analytical workup is described, while in the following section IV.6.3 a detailed working procedure is presented.

IV.6.1 Basic Principles and Data Analysis

The determination of lateral mobility can be achieved by experiments employing fluorescence recovery after photobleaching (FRAP) (60). Hereby, a fluorescently labeled probe is partially bleached by a strong laser pulse. Afterwards the recovery of the fluorescence intensity in the specific ROI (region of interest) is collected with time. Since unbleached fluorophores diffuse back into the focused ROI, information about the lateral mobility of the sample can be achieved. A second ROI is introduced to define the unspecific bleaching of the background intensity (see Fig. IV.12, A and B).

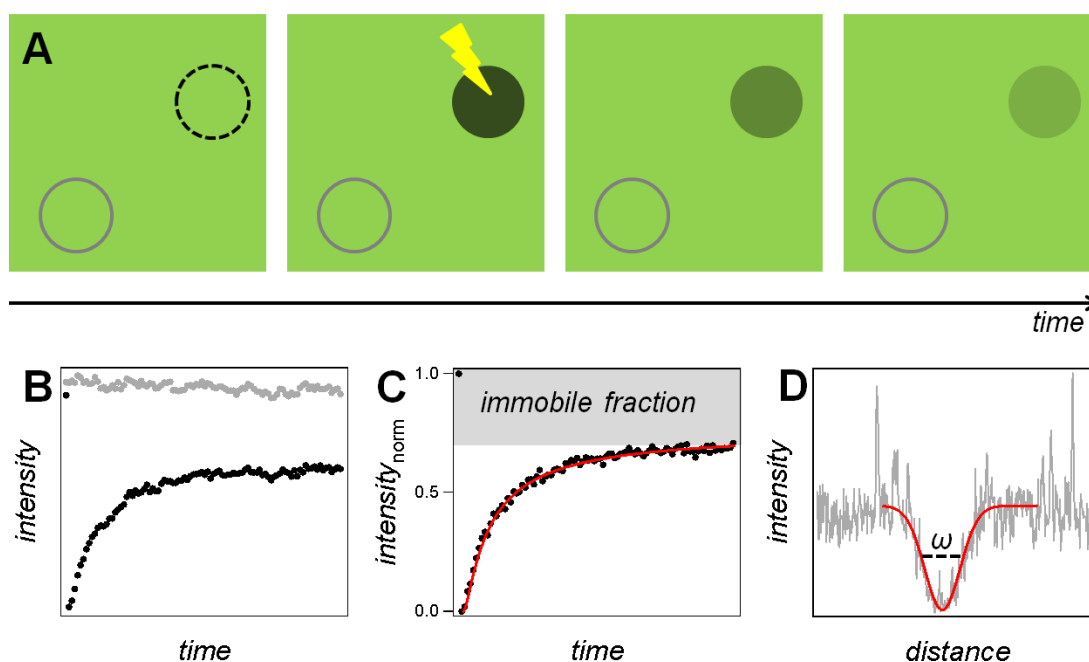


FIGURE IV.12 Schematic presentation of a FRAP experiment and subsequent analytical workup. (A) Time-resolved image series, starting with unbleached image with definition of two ROIs. The black ROI is bleached (2nd image) and the recovery of fluorescence intensity is collected with time (3rd and 4th image). (B) Determined fluorescence intensity for bleached ROI (black) and unbleached reference ROI (grey). (C) Normalized fluorescence recovery curve (black) with Axelrod fit function (red) and immobile fraction marked in grey. (D) Determination of ROI size by fitting Gaussian function (red) and defining half-width ω to intensity profile along bleached ROI (grey).

The two determined time courses of bleached intensity and background intensity can be normalized, resulting in a recovery curve starting at a maximal intensity of 1 before bleaching occurs, while the bleach event is characterized by an intensity of 0 (see Fig. IV.12, C). Even with $time \rightarrow \infty$, the intensity will not reach the maximum of 1 again, since a specific amount of bleached fluorescence probes are irreversibly destroyed. Furthermore, in most samples an additional immobile fraction can be determined, *i.e.* the lateral diffusion is hindered; hence no complete recovery is observed and the mobile fraction is $< 100\%$. This mobile fraction F_{mob} was

determined by the supplier's software of the fluorescence microscope used for data acquisition (ZEN, Carl Zeiss GmbH, Jena, Germany) using eq. IV.16:¹²

$$F_{mob} = \frac{I_{\infty} - I_0}{I_{prebleach} - I_0} \quad (IV.16)$$

Hereby, the intensities $I_{prebleach}$ (before bleaching) and I_0 , which is captured directly after the bleach pulse are related to I_{∞} , the intensity reached in equilibrium with $time \rightarrow \infty$.

The actual diffusion coefficient D was determined using a script written in Igor Pro (Wave Metrics, Wavemetrics, Tigard, OR, USA) considering the theoretical approaches of Axelrod and Soumpasis, which will be described in the following section (85, 86).

IV.6.2 Mathematical Descriptions in FRAP Data Analysis

Within the employed Igor Pro template, the diffusion coefficient D is defined by the half-width ω of the bleaching spot and the characteristic diffusion time τ_D (see eq. IV.17):

$$D = \frac{\omega^2}{4\tau_D} \quad (IV.17)$$

While the size of the ROI is defined by the used laser beam described with a Gaussian beam providing ω via a Gaussian fit to the intensity profile through the bleach spot (see Fig. IV.12, D), the diffusion time τ_D can be extracted using the Igor script employing eq. IV.18:

$$F_k(t) = \frac{qP_0C_0}{A_0} \sum_{n=0}^{\infty} \frac{(-K)^n}{n!} \left[1 + n \left(1 + \frac{2t}{\tau_D} \right) \right]^{-1} \quad (IV.18)$$

Hereby, $F_k(t)$ is the fluorescence intensity observed at time t , with n as time increments, starting at $t=0$, which is the time bleaching occurs. Furthermore, a constant factor is used in the equation, which is related to C_0 , the original concentration of fluorophores, P_0 , describing the laser power, A_0 as attenuation factor of beam during observation of recovery, and q , the product of all quantum efficiencies of absorption and emission. In the used Igor tool, this term is combined to the variable I_{max} . The function above is a series solution from eq. IV.19 shown below and valid for all t and K , which can be described as amount of bleaching. K is equivalent to the

¹² Zeiss.de: [www.zeiss.de/C1256D18002CC306/0/3B3915C40E420C4AC125724B002675E4/\\$file/45-0060_e.pdf](http://www.zeiss.de/C1256D18002CC306/0/3B3915C40E420C4AC125724B002675E4/$file/45-0060_e.pdf) (01. 08. 2012)

term $\alpha T I(0)$, where T is the duration of the bleach pulse with intensity $I(0)$, and α as a rate constant derived from bleaching kinetics.

$$F_k(t) = \frac{q}{A} \int I(r) \cdot C_k(r, t) \cdot dr^2 \quad (\text{IV.19})$$

Here, the fluorophore concentration C_k is defined as a function of position r and time t , which follows a first order kinetic. Furthermore, the intensity of the Gaussian beam $I(r)$ is given as a function of position, which can be also described by eq. IV.20, and is related to the ROI size and its half-width ω :

$$I(r) = \frac{2P_0}{\pi\omega^2} \exp\left(\frac{-2r^2}{\omega^2}\right) \quad (\text{IV.20})$$

IV.6.3 Experimental Procedures

FRAP experiments were carried out on glass (MatTek Dishes, Ashland, MA, USA), which was hydrophilized before spreading in an O_2 -Plasma (2×1 min) (see Chapter III.1.3). For bilayer formation, SUV were added and incubated on glass in a final concentration of $c_{\text{SUV}} = 0.1$ mg/mL in PB 6.8. If required, coupling reaction to produce lipopeptides and coiled-coil formation was carried out after rinsing of SSM as described in Chapter III.3.2. Membranes were made of fluid phase lipid POPC doped with 10 mol% MCCDOPE.

Two fluorescently active moieties were employed to determine the lateral mobility of the membrane and the coiled-coil structure, respectively (see Fig. IV.13).

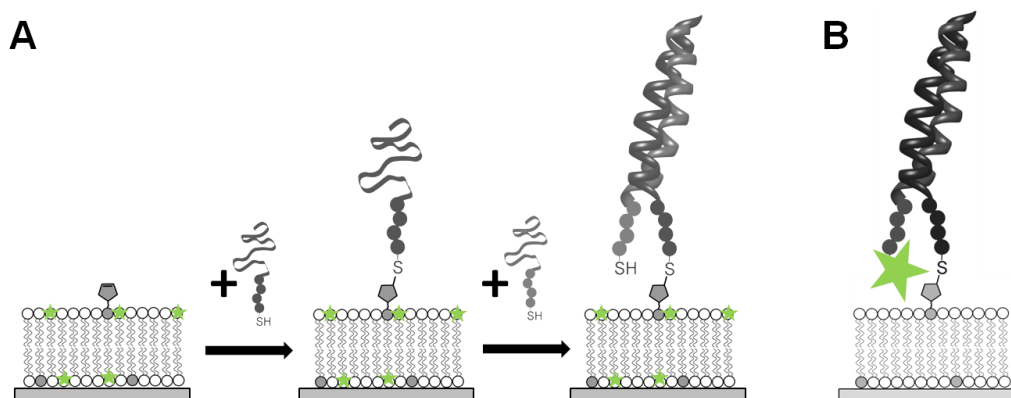


FIGURE IV.13 Schematic drawing of different labeling procedures. (A) BODIPY lipid (green) is introduced in a concentration of 1 mol% to the SSM. Afterwards, peptides can be added to form lipopeptides and coiled-coil heterodimers. (B) Complete coiled-coil structure is labeled by the means of coupling an OG488 moiety (green) to remaining cysteine groups.

This enabled us to determine the specific lateral mobility of the bilayer and the complete coiled-coil coupled to MCC-lipids. For SSM labeling, BODIPY (see Chapter III.1.2) was introduced to the bilayer in a concentration of 1 mol%. The completed coiled-coil heterodimers were fluorescently activated by adding an Oregon Green 488 maleimide moiety (OG488, see Chapter III.4.1), which coupled to the remaining cysteine group of the second peptide. The reaction could be carried out *in situ* with a fluorophore concentration of $c_{\text{OG488}} = 30 \mu\text{g/mL}$ and an overnight incubation at 4-8 °C. Excess material was removed by rinsing the sample with buffer. Since no unspecific interaction of OG488 with SSM could be detected, BODIPY labeled membranes were used as a reference.

FRAP experiments were carried out using an upright confocal laser scanning microscope (CLSM) equipped with a water immersion objective with 63× magnification (LSM710, Zeiss, Jena, Germany). For fluorescence excitation and bleaching an Argon laser ($\lambda_{\text{ex}} = 488 \text{ nm}$) was used. Time-elapsd CLSM images ($\approx 1 \text{ frame/s}$) were analyzed with a program written in Igor Pro (Wavemetrics, Tigard, OR, USA) to obtain lateral diffusion constants.

IV.7 Fusion Assays Based On Fluorescence Spectroscopy

Full fusion events require the proof of successful lipid and content mixing without any detectable leakage (10). Therefore, several fusion assays employing fluorescence spectroscopy were developed over time, using FRET (Förster Resonance Energy Transfer) as well as dequenching effects for detection. In this work, two different dequenching assays were used to characterize the fusogenicity of the synthesized lipopeptides, one for lipid mixing (see Chapter IV.7.2) and one for content mixing (see Chapter IV.7.3). The basic principles of the detection are presented in Chapter IV.7.1, while in IV.7.4 a detailed description of the preparative work is given.

IV.7.1 Dequenching Assays for Detection of Fusion

In bulk fusion assays based on fluorescence spectroscopy, usually two different vesicle populations are mixed resulting in fluorescence intensity changes upon successful lipid or content mixing. In this work, dequenching assays were employed with one vesicle population labeled with a fluorophore in a self-quenching high concentration, while the other vesicle population remains unlabeled (see Fig. IV.14). Depending on the type of fusion assay, membrane based fluorophores or water soluble fluorophores, which are enclosed in the vesicle lumen, are

used. Mixing and fusion of the vesicle populations results in dilution of the fluorophore, detectable by an increasing fluorescence intensity.

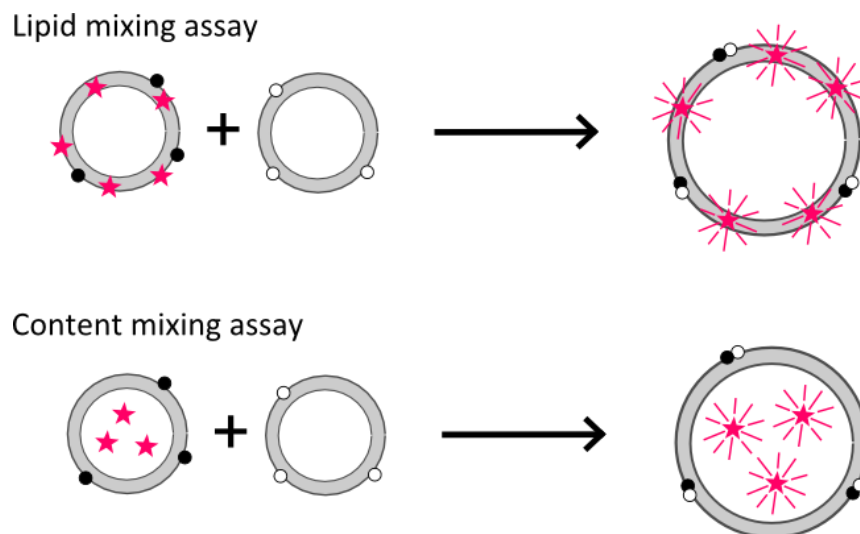


FIGURE IV.14 Schematic presentation of lipid and content mixing dequenching assays. Black and white points indicate fusion-mediating moieties. Quenched fluorophores are represented by pink stars, fluorescently active fluorophores are marked as bright stars.

Quenching of fluorescently active molecules is characterized by a decrease of fluorescence intensity without destroying the molecule. Therefore, the excited state of the fluorophore has to undergo processes like energy transfer, internal conversion or collisions with quencher molecules, to emit energy in a non-radiative process (60). In our assays, quenching is due to the high concentrations of the fluorescently active molecules, which can be often described by the mechanism of dynamic quenching. Hereby, molecules collide and the energy is finally transferred into thermal energy (58).

To quantify the quenching process, the Stern-Volmer equation can be used (eq. IV.21). Therefore, a quenched (F_{quenched}) and unquenched, maximal intensity (F_{max}) is measured, whereby a quenching constant K_{SV} can be determined which is dependent on the quencher concentration $[Q]$.

$$\frac{F_{\text{max}}}{F_{\text{quenched}}} - 1 = K_{SV} \cdot [Q] \quad (\text{IV.21})$$

IV.7.1.1 Lipid Mixing Assay

Lipid mixing was analyzed by a Texas Red self-quenching assay (87). Hereby, the membrane shell of one vesicle population is doped with 10 mol% of fluorescently labeled lipid Texas Red (see Chapter III.1.2), while the other vesicle population is solely consisting of fluorescently inactive molecules.

To determine the quenching mechanism of Texas Red in SUV, a series of vesicles were prepared with an amount of fluorescent dye ranging from 1-10 mol%. Afterwards, the fluorescence intensity was measured before and after disruption of vesicles, providing the possibility to quantify quenching by a Stern-Volmer plot (see Fig. IV.15). In the concentration range of interest for our experiments (5-10 mol%), the curve is linearly with sufficient accuracy; hence K_{SV} can be determined from the slope of a linear regression to the data.

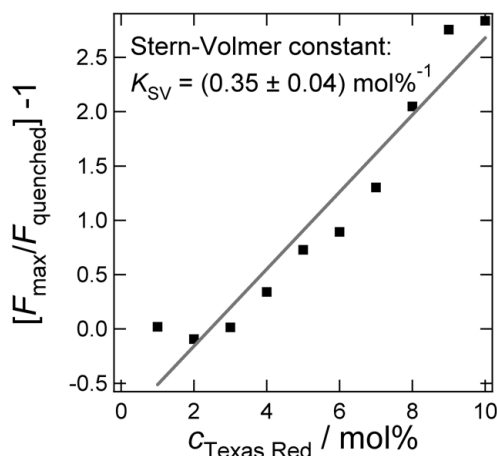


FIGURE IV.15 Stern-Volmer plot for Texas Red quenching in DOPC vesicles. F_{quenched} is fluorescence intensity in intact vesicles, F_{max} the intensity after disruption of SUV with detergent (SDS, $c = 0.2\%$). Points correspond to measured data; grey line shows a linear fit. Stern-Volmer constant K_{SV} was determined from the slope.

For normalization, we consider 100% fusion as a one-to-one mixture of used vesicle populations; that means that exactly one labeled vesicle fuses with one unlabeled vesicle. Assuming that the two interacting liposomes possess the same size, membrane mixing results in a twofold dilution, since the membrane area of the new vesicle doubles. As a consequence, starting with 10 mol% Texas Red as membrane dye for lipid mixing, 100% fusion results in 5 mol% Texas Red.

Finally, using this concentration for the diluted fluorophore and the resulting K_{SV} , the ratio

$F_{\max}/F_{\text{quenched}} - 1$ after 100 % fusion can be calculated and used for normalization of fluorescence

data as a reference value, resulting in this case to 1.75 for $F_{\max}/F_{\text{quenched}} - 1$.

One of the drawbacks of the here presented dequenching fusion assay is that hemifusion and fusion are not distinguishable because solely lipid mixing is detected, without any information of the participating membrane leaflets.

IV.7.1.2 Content Mixing Assay

For content mixing assays, a water-soluble, fluorescently active molecule, which is not able to cross the lipid bilayer, was enclosed in the vesicle lumen of one of the two prepared SUV populations. In this work, SRB was used as fluorescence marker (see Chapter III.4.1) which is at 20 mM in a self-quenching concentration (34, 88).

For normalization of fusion, we consider 100 % with a one-to-one mixture of vesicles, as we did for lipid mixing. However, while the membrane surface doubles in our assays, the volume enclosed by the fused vesicles increases by a factor of $2^{3/2} \approx 2.8$, which is due to the different scaling of radii concerning area (r^2) and volume (r^3). Therefore, upon mixing of one labeled and one unlabeled SUV, the starting concentration of SRB (20 mM) is diluted to ≈ 7 mM. Using the Stern-Volmer constant $K_{SV} = 990 \text{ M}^{-1}$ published by Plant *et al.* (58), the normalization can be done analogue to lipid mixing experiments. This results in a reference value of 6.93 for

$F_{\max}/F_{\text{quenched}} - 1$, which equals 100 % fusion.

The determination of stable baselines before fusion starts gives a hint that actual no leakage occurs, which would result in a consistent increase of fluorescence intensity; hence, full fusion can be proven by this dequenching assay.

IV.7.2 Experimental Procedures

For detailed description of vesicle preparation, lipopeptide formation and removal of excess peptides, see Chapter III.1.3 and III.3.2. Fluorescence spectroscopy experiments were carried out on a FluoroMax-4 (Horiba Scientific, Unterhaching, Germany). In both experiments, the detergent SDS (sodium dodecylsulfate) was added in a final concentration of ≈ 0.2 % to determine the maximum fluorescence intensity.

IV.7.2.1 Texas Red Self-Quenching Lipid Mixing

For Texas Red self-quenching experiments, SUV preparation and subsequent lipopeptide formation as well as the measurement were carried out in PB 6.8. Both vesicle populations contained 1-3 mol% MCCDOPE; population 1 contained 10 mol% Texas Red, and was functionalized with K-peptides. Population 2 was functionalized with E-peptides. Excess peptide was removed by column chromatography using sephadex NAP-25 columns (illustra, GE Healthcare, Solingen, Germany). For the actual measurements, excitation wavelength was set to $\lambda_{\text{ex}} = 582 \text{ nm}$ (slit 1 nm), while emission was detected at $\lambda_{\text{em}} = 606 \text{ nm}$ (slit 3 nm) over time. First, the labeled SUV population was placed in the spectrometer and measured until a stable baseline was reached. Then, the second SUV population was added and the increase in intensity was detected.

IV.7.2.2 Sulforhodamin B Content Mixing

For content mixing LUV were prepared by extrusion (size: 100 nm). Vesicle population 1 was prepared in HEPES 7.4+SRB and hence contained sulforhodamin B (SRB) in a self-quenching concentration of 20 μM (88). Also subsequent lipopeptide formation was carried out in SRB containing buffer to avoid osmotic stress. Population 2 was prepared in HEPES 7.4 with isoosmolar salt concentration, to give the unlabeled SUV. Excess peptide and SRB in surrounding buffer was removed by column chromatography using sephadex NAP-25 columns and HEPES 7.4 as running buffer (illustra, GE Healthcare, Solingen, Germany). The absorption and excitation of SRB takes place at $\lambda_{\text{ex}} = 565 \text{ nm}$ (slit 1 nm), while the emission can be detected at $\lambda_{\text{em}} = 585 \text{ nm}$ (slit 5 nm). For the actual experiment, the SRB containing SUV were diluted with HEPES 7.4, placed in the spectrometer and measured until a stable baseline was reached before adding the second unlabeled vesicle population. To trigger fusion, Calcium was added to a final concentration of $c_{\text{Calcium}} = 8 \text{ mM}$.

V Structural Analysis of Model System

In this Chapter, the minimal model system for coiled-coil formation employed in this thesis will be described. To assure its functionality, it is crucial to proof the α -helical structure of coiled-coil complexes in solution (Chapter V.2) as well as on lipid bilayers (Chapter V.3). In the following Chapter membrane properties (V.3.1) as well as the *in situ* coupling reaction to form lipopeptides will be presented (V.3.2).

V.1 Introduction

The coiled-coil forming minimal model system employed in this thesis is based on the three heptad repeat containing sequences named E and K, which were first described in 2002 by Litowski and Hodges (48). The high specificity of their heterodimerization renders them ideal systems for various approaches in biophysical chemistry. For instance, they were used by Shlizerman *et al.* for the build-up of molecular electronic devices (89), while Apostolovic and Klok investigated the pH-sensitivity of their heterodimerization (90). The authors showed by CD spectroscopy and analytical ultracentrifugation that E-peptides form homotrimeric coiled-coils under acidic conditions. In a follow-up paper, they suggested the possibility of E/K interaction as mediators for drug carriers, where the drug and carrier polymer are linked via coiled-coil motifs (91). After uptake into a living cell, drugs can be released from the carrier due to peptide unfolding induced by internal pH differences in endosomes. In another approach, the group of Matsuzaki applied this heterodimeric coiled-coil as a motor for a labeling technique involving membrane receptors of living cells by attaching the E-sequences to prostaglandin receptors which afterwards formed heterodimers with fluorescently labeled K-peptides (92).

In 2010 Marsden *et al.* applied these structures for mimicking SNARE-mediated membrane-membrane interaction (33). They formed hybrid structures containing a lipid anchor, a spacer made of PEG units and the actual recognition sequences, which were incorporated in vesicles to induce membrane fusion. Based on their findings, we enhanced the described model system by the possibility to form parallel and antiparallel coiled-coil structures and analyzed the impact of different spacer moieties.

In this chapter, we first analyze the coiled-coil formation of the three sets of different peptides, which is an important prerequisite for further experiments. Besides secondary structure studies by the means of CD spectroscopy, IR spectroscopy is employed to prove the existence of the

superhelical structure in coiled-coil complexes. Additionally, the membrane functionalization carried out by an *in situ* coupling reaction is studied in detail (see Fig. V.1).

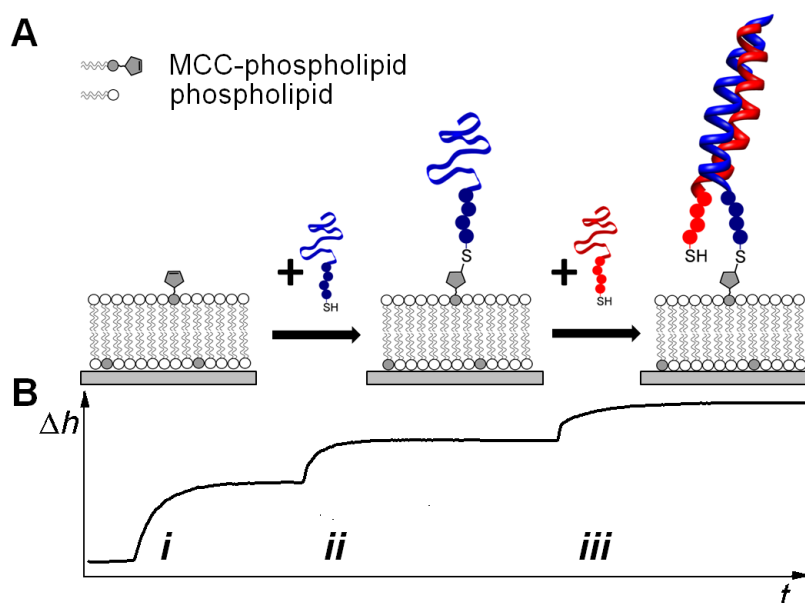


FIGURE V.1 (A) Schematic drawing of *in situ* coupling reaction between MCC-phospholipid and cysteine-containing peptide followed by coiled-coil formation on a SSM (solid supported membrane). (B) Corresponding height increases for processes displayed in A (*i* = spreading of SSM; *ii* = *in situ* coupling reaction; *iii* = coiled-coil formation).

The formation of lipopeptides is analyzed with respect to kinetic properties and specificity. Therefore, time-resolved height measurements carried out by the means of ellipsometry are powerful tools to follow the coupling reaction. Furthermore, we will demonstrate that the formation of lipopeptides does not affect the successive heterodimerization on a membrane surface.

V.2 Secondary Structure Before and After Heterodimerization¹³

During coiled-coil formation due to heterodimerization of peptides, significant changes in secondary structure should be observed. In this chapter, solely peptides in solution are analyzed by means of CD and IR spectroscopy concerning their coiled-coil formation. We propose that heterodimerization takes place under formation of parallel (V.2.1) and antiparallel (V.2.2) coiled-coil structures, due to the inversion of employed recognition sequence. The employed peptides are synthesized presenting an isoleucine residue at *a* position and lacking at

¹³ Parts of this Chapter are published in Gesa Pähler, Cornelia Panse, Ulf Diederichsen and Andreas Janshoff "Coiled-coil formation on lipid bilayers-implications for docking and fusion efficiency", *Biophysical Journal* **2012**, *103*, 2295-2303.

d position while parallel heterodimerization. Since it is well known, that isoleucine as a β -branched amino acid is favored for the α position in coiled-coil structures (49), it can be assumed that if mixing of an inverted peptide sequence with a corresponding non-inverted one results in the formation of a coiled-coil structure, the antiparallel orientation is build.

V.2.1 Parallel Coiled-coil Formation

We investigated coiled-coil formation of E- and K-peptides in solution by means of CD spectroscopy. Therefore, following peptides and their mixtures were analyzed: K3Cys and E3Cys, *i*-K3Cys and *i*-E3Cys as well as *i*-K3PEG with *i*-E3PEG (see Fig. V.2). Each set of heterodimeric peptides showed a clear increase of α -helical content upon mixing, indicated in the spectra by the maximum around 190 nm and the two distinct minima at 208 nm and 220 nm. Previous studies showed that the intensities of the two mentioned minima are virtually equal for coiled-coil motifs, while for single stranded α -helices the ratio of $[\theta]_{220\text{nm}}/[\theta]_{208\text{nm}}$ is reduced to about 0.86 (93). Our calculated ratios (see table V.1, last row) for the heterodimeric pairs are clearly increasing to values around 1, which confirms the formation of coiled-coil structures.

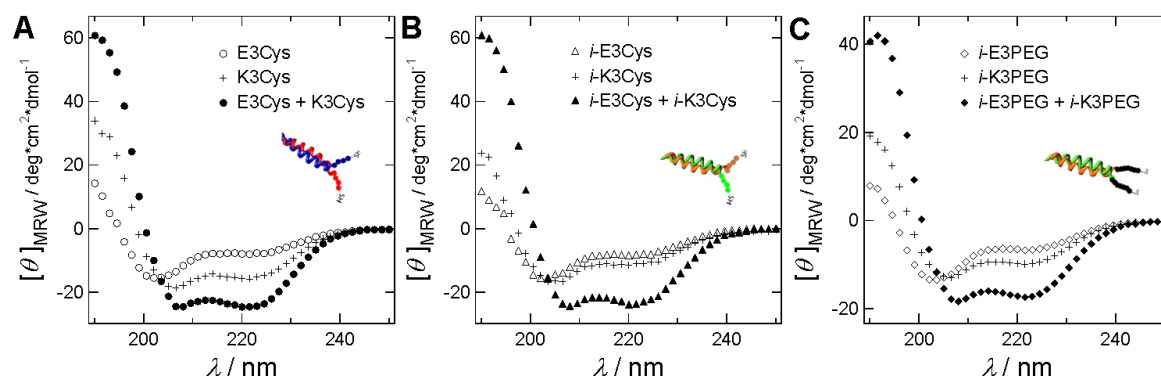


FIGURE V.2 CD spectra of employed peptides and their heterodimeric mixtures ($c_{\text{peptide}} = 0.1 \text{ mM}$ in PB 6.8). (A) E3Cys (open circles), K3Cys (crosses) and their 1:1 mixture (filled circles). (B) *i*-E3Cys (open triangles), *i*-K3Cys (crosses) and their 1:1 mixture (filled triangles). (C) *i*-E3PEG (open squares), *i*-K3PEG (crosses) and their 1:1 mixture (filled squares).

By the means of secondary structure analyses, we found that K-peptides already show a substantial α -helical content in solution, while E-peptides adopt a predominately random coil structure (see Table V.1). After formation of parallel-aligned heterodimeric coiled-coil structures, the α -helical content increases considerably over 70 %, while the β -sheet content vanishes. Interestingly, PEGylated peptides show a significantly lower helical structuring in their monomeric form than their unPEGylated analogs; however their mixture also shows 73 % of

α -helix. The ratio of α -helix to random coil content of each coiled-coil dimer reflects the ratio of amino acids forming the heptad repeat (21 aa) to amino acids, which merely act as an anchor group (6-7 aa) or to the amount of PEG-residues present, respectively.

	E3Cys	K3Cys	<i>i</i> -E3Cys	<i>i</i> -K3Cys	<i>i</i> -E3PEG	<i>i</i> -K3PEG	E3Cys + K3Cys	<i>i</i> -E3Cys + <i>i</i> -K3Cys	<i>i</i> -E3PEG + <i>i</i> -K3PEG
α -helix / %	31	46	31	44	9	21	79	78	73
β -sheet / %	12	23	12	23	35	23	0	0	2
random / %	57	31	57	33	56	56	21	21	25
$[\theta]_{220}/[\theta]_{208}$	0.69	0.87	0.71	0.75	0.61	0.80	1.00	0.98	0.93

TABLE V.1 Distribution of secondary structure fractions of peptides before and after formation of coiled-coil assemblies obtained from CD measurements in solution. All measurements were carried out in PB 6.8 with an overall peptide concentration of $c = 0.1$ mM. Percentages were obtained from *DichroWeb* online analysis software (72, 73).

Apart from CD spectroscopy, which is sensitive to α -helix formation of peptides but rather insensitive to distinguish a single α -helix from a coiled-coil motif, transmission FT IR spectroscopy was employed. Here, the amide I band absorbing near 1650 cm^{-1} is mainly generated by C=O stretching vibrations in the protein backbone, which stabilizes secondary structure (64) (see Chapter IV.1.2). Therefore, this region is sensitive to conformational changes such as coiled-coil formation, which can be seen in the difference between single peptide spectra and spectra of peptide mixtures (see Fig. V.3).

While each E-peptide shows a band maxima around 1650 cm^{-1} , the signal of K-peptides is shifted to lower wavenumbers. In the corresponding heterodimeric peptide mixtures, the band maximum is located between 1645 cm^{-1} and 1652 cm^{-1} . Heimburg and coworkers showed that dimeric coiled-coil structures display at least three separable bands in their amide I region (67). This separation can be achieved by deconvoluting the FT IR spectra and reassembling the amide I band by multiple Gaussian fits (see Fig. V.3, lower panel). All sets of heterodimeric peptide mixtures applied in this thesis show the expected band separation indicating a successful formation of coiled-coil structures in solution.

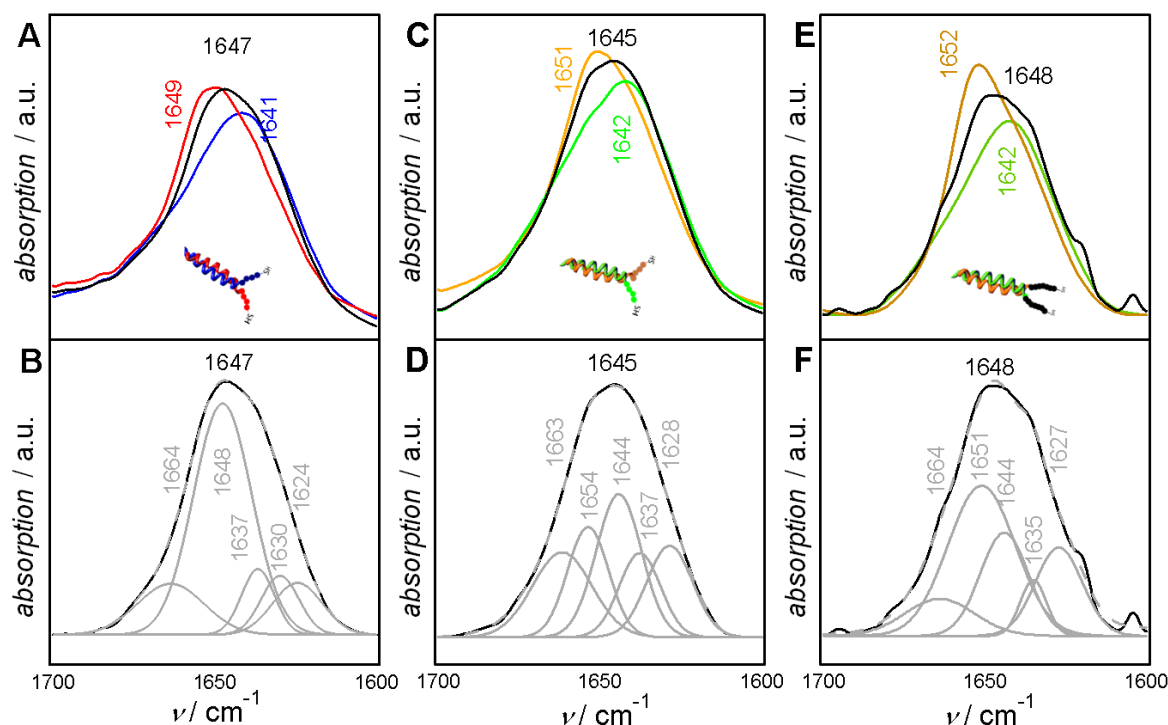


FIGURE V.3 Amide I band in transmission FT IR spectra of E- and K-peptides in solution (D_2O with 50 mM NaCl) as monomer and after heterodimerization. Numbers in graph indicate position of band maxima. (A) E3Cys (red), K3Cys (blue) and their 1:1 mixture (black). (B) Deconvolution of amide I band from E3Cys/K3Cys heterodimer shown above by multiple Gaussian fits to document formation of coiled-coil dimers. The positions of Gaussian functions were estimated by computing the second derivative of the spectra. Experimental data is shown in black, grey curves are Gaussian fits, grey scattered line represents the sum of all Gaussian fit. (C) *i*-E3Cys (yellow), *i*-K3Cys (green) and their 1:1 mixture (black). (D) Deconvolution as described above for *i*-E3Cys/*i*-K3Cys heterodimer. (E) *i*-E3PEG (yellow), *i*-K3PEG (green) and their 1:1 mixture (black). (F) Deconvolution as described above for *i*-E3PEG/*i*-K3PEG heterodimer.

Heimburg *et al.* also found a correlation between the spectral maximum and the helical distortion, *i.e.*, the superhelical pitch. The length of the superhelical pitch is related to the distortion and the spectral maximum, respectively the spectral weight. In other words, a spectral maximum at higher wavenumbers corresponds to an increased length of the superhelical pitch. For the peptide mixtures presented here, their spectral maxima are located $\approx 1647 \text{ cm}^{-1}$, which can be correlated to the formation of a superhelical pitch with a length of $\approx 200 \text{ \AA}$.

In summary, CD and IR spectroscopy confirm that E- and K-peptides interact by forming defined coiled-coil dimers. Inverting the recognition sequence has no influence concerning the secondary structure of the monomeric peptides, but introducing a short PEG linker leads to more unstructured single peptide strands. However, upon mixing in a one-to-one ratio, the clear increase in α -helical structure as well as the decrease of β -sheets to almost zero proves the successful coiled-coil formation and is similar for all three employed sets of heterodimers.

V.2.2 Antiparallel Coiled-coil Formation

Since the order of amino acids in the recognition sequence is inverted concerning *i*-K3Cys and K3Cys, and *i*-E3Cys and E3Cys, respectively, antiparallel coiled-coil formation is assumed. This is mainly due to the β -branched amino acid isoleucine, which favors the *a* position (49). In the mixtures presented in this chapter, isoleucine would be forced to occupy the *d* position if a parallel heterodimer would be formed. This already hints a formation of antiparallel heterodimerization. Furthermore, the melting temperature T_m of the coiled-coil structures can be predicted using an algorithm¹⁴ based on a catalogue of helix propensities and electrostatic interactions for the employed amino acids in the recognition sequence (94, 95). Hereby, the T_m for parallel (Chapter V.2.1) as well as for antiparallel coiled-coil formation presented here can be estimated to be 56 °C. If we would assume a parallel interaction between the peptide mixtures of *i*-K3Cys/E3Cys and *i*-E3Cys/K3Cys, respectively, T_m would decrease to only 24 °C, hence the antiparallel heterodimerization is more stable and therefore favored.

To check if coiled-coil formation occurs upon mixing of inverted peptide sequences with their corresponding non-inverted sequences, CD spectroscopy measurements were employed analogously to the measurements described in Chapter V.2.1. Hereby, both one-to-one mixtures of *i*-K3Cys with E3Cys and *i*-E3Cys with K3Cys, respectively, showed spectra with significant α -helical propensities (see Fig. V.4).

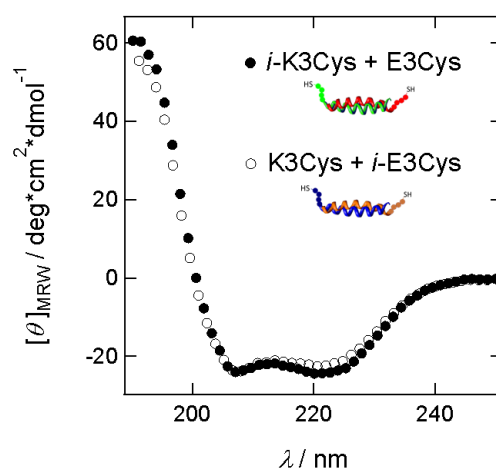


FIGURE V.4 Spectra of antiparallel coiled-coil heterodimers composed of *i*-K3Cys and E3Cys (filled circles) or K3Cys and *i*-E3Cys (open circles), respectively. Amount of α -helix was determined to be 79 % (filled circles) and 73 % (open circles), respectively.

¹⁴ bZIP coiled-coil interaction prediction algorithm (bCIPA), available online: <http://www.molbiotech.uni-freiburg.de/bCIPA/> (21. 08. 2012).

In the graph above, both mixtures display the specific maximum at 190 nm and the two local minima at 208 nm and 220 nm expected for α -helical structures. The intensity ratio of these minima for the heterodimeric pairs can be calculated to be around 1, which confirms the formation of a coiled-coil structure. Also, the amount of α -helical structure is determined to be relatively high compared to single peptide strands (see Table V.2).

	<i>i</i> -E3Cys + K3Cys	E3Cys + <i>i</i> -K3Cys
α -helix / %	73	79
β -sheet / %	2	0
random / %	24	21
$[\theta]_{220}/[\theta]_{208}$	0.94	1.03

TABLE V.2 Distribution of secondary structure fractions of peptides after antiparallel coiled-coil formation obtained from CD spectroscopy measurements in solution (PB 6.8; $c_{\text{peptide}} = 0.1 \text{ mM}$). Percentages were obtained from *DichroWeb* online analysis software (72, 73).

From these results, it can be concluded that heterodimeric coiled-coil structures are formed also between *i*-K3Cys with E3Cys and *i*-E3Cys with K3Cys, respectively. Nevertheless, the data presented here gives no hint of parallel or antiparallel orientation of the peptides to each other, since with CD spectroscopy only secondary structure changes can be analyzed. But, considering the reasons mentioned above and the calculations concerning the melting temperatures, an antiparallel formation can be safely assumed.

V.3 Structural Analyses After *in situ* Coupling to a Lipid Bilayer

In this part, peptide-membrane interaction like the *in situ* coupling reaction will be presented. In the first Chapter V.3.1 solid supported lipid bilayers in dependence of cholesterol are characterized concerning their layer thicknesses to evaluate the ellipsometry analysis. In the second part (Chapter V.3.2) the actual *in situ* coupling reaction is analyzed concerning its kinetic and specificity as well as the subsequent coiled-coil formation through peptide heterodimerization is analyzed on a solid supported membrane (SSM).

V.3.1 Membrane Thickness in Dependence of Cholesterol

Cholesterol is a major regulator of bilayer thickness, which is important for the proteins integration in membranes (96). To put the effect of cholesterol to lipid bilayer formation in

numbers, different lipids were characterized concerning their thickness after formation of solid supported membranes. Hereby, ellipsometry was employed to follow the spreading process and to determine specific layer thicknesses. Four different phosphocholine lipids (abbr.: PC), namely DMOPC (di14:1), DΔPPC (di16:1), DOPC (di18:1) and DEPC (di20:1), varying in their acyl chain length, were analyzed. All lipids carry two unsaturated identical fatty acid residues and are all in their fluid phase at room temperature. Therefore, differences in layer thickness are solely due to the number of carbons in the acyl chains. The resulting heights were compared to membrane thicknesses of SSM which contained 29 mol% cholesterol (abbr.: chol) (see Fig. V.5).

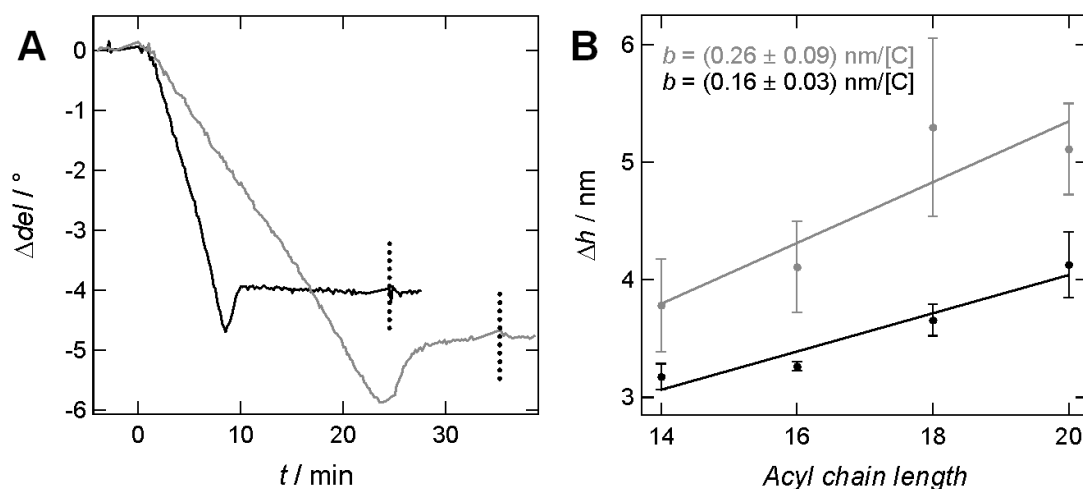


FIGURE V.5 (A) Spreading process for DEPC 100 % (black) and DEPC/chol 71:29 (grey). SUV were added at $t = 0$, scattered lines indicate start of rinsing. (B) Mean determined layer thicknesses for spreaded bilayers with varying acyl chain lengths consisting of 100 % unsaturated lipids (black circles) and mixtures with cholesterol (PC/chol 71:29) (grey); lines represent linear regression with indicated slopes b . Used lipids: DMOPC (di14:1), DΔPPC (di16:1), DOPC (di18:1) and DEPC (di20:1).

From graph A in Figure V.5 it is getting obvious that the presence of cholesterol slows down the spreading process, which might be attributed to larger bending modulus of cholesterol containing membranes and therefore less contact area is driving the spreading process. Furthermore, it can be seen that layer thickness is increased for the mixture in comparison with the pure PC SSM. In Figure V.5 B the mean determined heights, calculated from the angle del , for the employed PC lipids and their cholesterol containing mixtures are presented against the number of carbon atoms per fatty acid residue. Besides a linear increase of layer thickness with carbon atoms present in acyl chains, an increased layer thickness for all used PC/chol mixtures is shown (see also Table V.3), which is in good accordance with literature (97). From the linear fit functions, a height increase per carbon atom can be given, which is $(0.16 \pm 0.03) \text{ nm}/[\text{C}]$ for pure lipids and $(0.26 \pm 0.09) \text{ nm}/[\text{C}]$ for cholesterol mixtures. A linearity of pure lipid bilayer thickness

concerning their acyl chain length was already shown in 1983 by Lewis and Engelmann (98), however this linearity is retained upon addition of cholesterol.

	DMOPC (di14:1)	DΔPPC (di16:1)	DOPC (di18:1)	DEPC (di20:1)
h_{PC} / nm	3.2 ± 0.1	3.3 ± 0.1	3.7 ± 0.1	4.1 ± 0.3
$h_{PC/chol} / \text{nm}$	3.8 ± 0.4	4.1 ± 0.4	5.3 ± 0.8	5.1 ± 0.4
ratio	1.19	1.26	1.45	1.24

TABLE V.3 Mean determined heights for spreaded bilayers consisting of 100 % unsaturated PC-lipids (h_{PC}) and PC/chol 71:29 ($h_{PC/chol}$), respectively. The last row gives the ratio of height increase.

From the layer thicknesses (see Table V.3), a ratio of height increase due to cholesterol addition can be calculated. All determined ratios are in the same regime, resulting in a mean increase by a factor of 1.29 ± 0.11 for SSM thickness upon cholesterol addition. In general, cholesterol containing membranes showed not only a slower spreading process, but also the determined heights present a significantly higher variance than for the pure PC lipid bilayers, which might be due to incomplete spreading processes and multilayer formation, respectively. Therefore, in the following experiments the usage of cholesterol was avoided to achieve a higher reproducibility of the model membranes.

V.3.2 Membrane Functionalization by *in situ* Coupling Reactions

In situ coupling of peptides to solid supported membranes (SSM) through maleimide chemistry was monitored by time-resolved ellipsometry and ATR-FT IR spectroscopy. The combination of these methods gives the possibility to focus on kinetic aspects of the reaction (see Chapter V.3.2.1) as well as to gain insights concerning peptides' secondary structure on SSMs (V.3.2.2). Finally, lipopeptide formation is analyzed quantitatively in terms of its specificity (V.3.2.3).

V.3.2.1 Kinetic Analyses of Membrane Functionalization

The formation of hybrid lipopeptide structures (abbr.: LP-) is achieved via build-up of a covalent bond between peptides with C-terminal cysteine residues and maleimide functionalized receptor lipids embedded in a SSM. To analyze the kinetics of this *in situ* coupling reaction, time-resolved ellipsometry is employed to determine the principal angle $\Delta\theta$ which is proportional to layer thicknesses for sufficiently thin dielectric layers ($h < 30 \text{ nm}$) (80). Absolute height changes

resulting from peptide coupling and coiled-coil formation on a spreaded SSM can be computed from del assuming a refraction index of 1.5 for the peptides.

For the kinetic measurements small unilamellar vesicles consisting of DOPC/MCCDOPE 90:10 were spread on the silica to form SSMs. Afterwards, the first peptide sequence was coupled via maleimide chemistry to form lipopeptides which serve as receptors to form coiled-coil motifs at the membrane surface (see Fig. V.6).

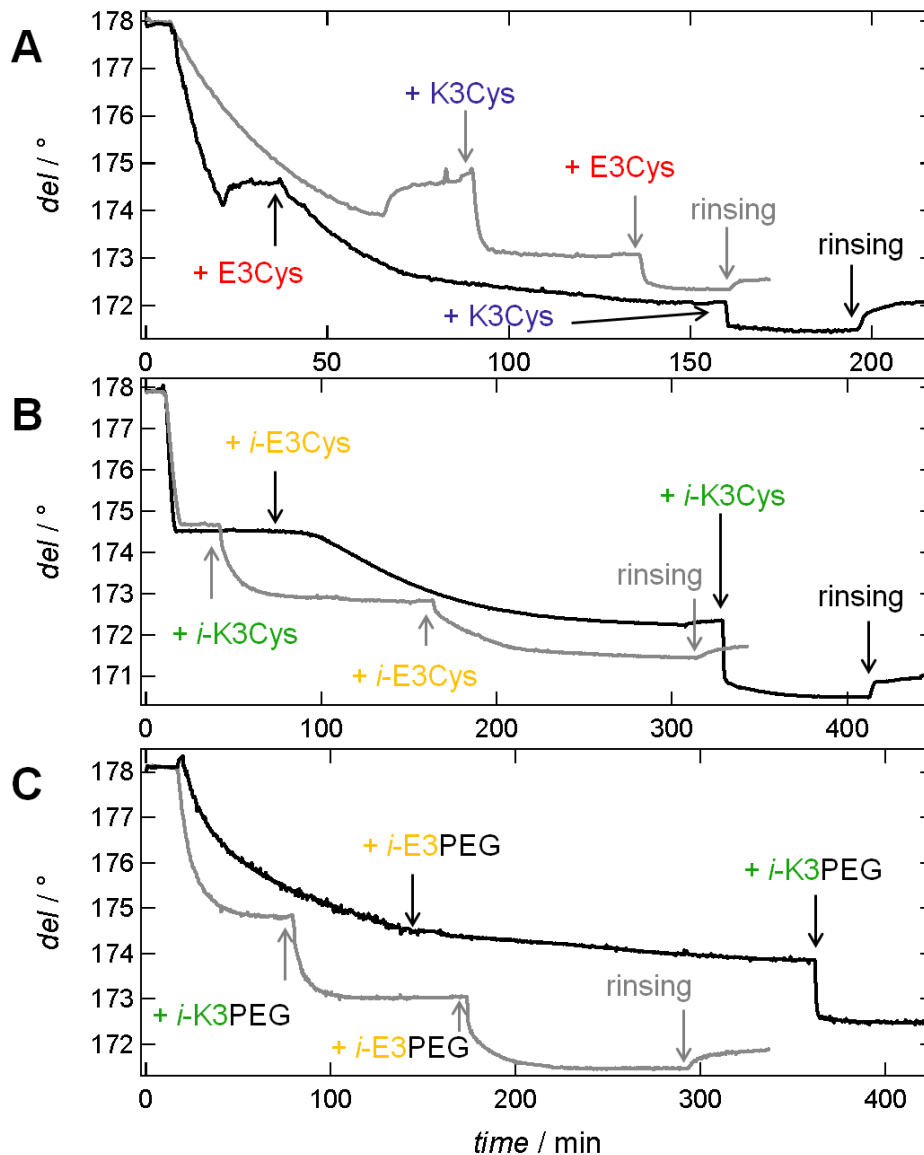


FIGURE V.6 Exemplary binding kinetics of E- and K-peptides to a DOPC/MCCDOPE 90:10 lipid bilayer spread on silicon oxide with ellipsometry in PB 6.8. Arrows indicate peptide addition and final rinsing, SUV to form SSM were added at the beginning of experiment. Before each addition of substance, a rinsing step was carried out of at least 5 min (not indicated in graphs). (A) Lipopeptide formation of K3Cys (grey) / E3Cys (black) followed by addition of E3Cys (grey) / K3Cys (black). (A) Lipopeptide formation of *i*-K3Cys (grey) / *i*-E3Cys (black) followed by addition of *i*-E3Cys (grey) / *i*-K3Cys (black). (C) Lipopeptide formation of *i*-K3PEG (grey) / *i*-E3PEG (black) followed by addition of *i*-E3PEG (grey) / *i*-K3PEG (black).

In the graph shown above, a steep drop of del indicates the formation of a lipid bilayer after SUV addition. The calculated layer thickness for the formed SSM from ellipsometry is $h_{SSM} \approx 3.5-3.7$ nm, which is in good agreement to reported values (99). In all curves, lipopeptide as well as coiled-coil formation is clearly visible by a further decrease of angle del , which is related to an increase of height. It gets obvious that the *in situ* coupling reaction of E-peptides to MCCDOPE is very slow in comparison to lipopeptide formation of K-peptides. A possible reason might be the negative charge of E-peptides resulting in an electrostatic repulsion of the membrane, since the receptor lipids MCCDOPE carry a net charge of -1. On the other hand, K-peptides exhibit a net charge of +3 at physiological conditions, promoting the interaction with the receptor lipids. In the final rinsing step a significant decrease of layer thickness is observed. Here, no covalent bonds like during the *in situ* coupling reaction of cysteine to a maleimide anchor are created but stable coiled-coil structures are formed; however, this reaction is partial reversible.

With 10 mol% of receptor lipids present in the lipid bilayer, a full coverage of the surface with lipopeptides can be assumed due to proportions of one peptide compared to a lipid bilayer headgroup. Therefore, the heights determined here display roughly the actual peptide sizes which are summarized in Table V.4. While lipopeptide formation corresponds to a layer thickness of ≈ 1.7 nm, addition of second peptide leads to a smaller height increase (≈ 1.2 nm). This can be explained by the structure of one heterodimeric coiled-coil complex, where peptide sequences wrap around each other and induce a more straightened up position on the membrane surface. The dimensional size of a complete coiled-coil complex can be determined to be ≈ 2.5 nm.

	LP-K3Cys + E3Cys	LP-E3Cys + K3Cys*	LP- <i>i</i> -K3Cys + <i>i</i> -E3Cys	LP- <i>i</i> -E3Cys + <i>i</i> -K3Cys	LP- <i>i</i> -K3PEG + <i>i</i> -E3PEG	LP- <i>i</i> -E3PEG + <i>i</i> -K3PEG*
$\Delta h_{LP} / \text{nm}$	2.0 ± 0.5	2.7	1.4 ± 0.5	1.6 ± 1.4	1.6 ± 1.0	0.7
$\Delta h_{cc} / \text{nm}$	1.3 ± 0.7	0.7	0.9 ± 0.3	1.4 ± 1.0	1.4 ± 0.7	1.5
$\Delta h_{rinse} / \text{nm}$	-0.3 ± 0.1	-0.7	-0.2 ± 0.1	-0.5 ± 0.2	-0.4 ± 0.1	<i>n.a.</i>
$\Delta h_{total} / \text{nm}$	3.0 ± 0.5	2.7	2.1 ± 0.8	2.5 ± 2.1	2.6 ± 1.6	2.2

TABLE V.4 Absolute height changes for *in situ* coupling reaction (Δh_{LP}), coiled-coil formation (Δh_{cc}), final rinsing (Δh_{rinse}) and total layer thickness of fully build-up coiled-coil structure (Δh_{total}) on a SSM consisting of DOPC/MCCDOPE 90:10. Mean values with their standard deviations are given determined from at least 2 measurements. *) No statistic could be determined due to slow binding kinetics of E-peptides to maleimide lipids.

Furthermore, from Figure V.6 it is obvious that kinetics of coiled-coil heterodimerization after completed lipopeptide formation are depending on the type of provided peptide coupled to the bilayer. Generally, we observe faster association rates if K-peptides are added to E-lipopeptides as opposed to addition of E-peptides to K-lipopeptides (see Fig. V.7). These adsorption kinetics can be best described by a double exponential fit where two independent time constants τ_1 and τ_2 are determined corresponding to distinct height increases A_1 and A_2 . Additionally, the kinetics of final rinsing steps are computed by applying an exponential function to describe the here observed dissociation phase. From this, a further time constant τ is defined, which is correlated with the inverse k_{off} binding rate.

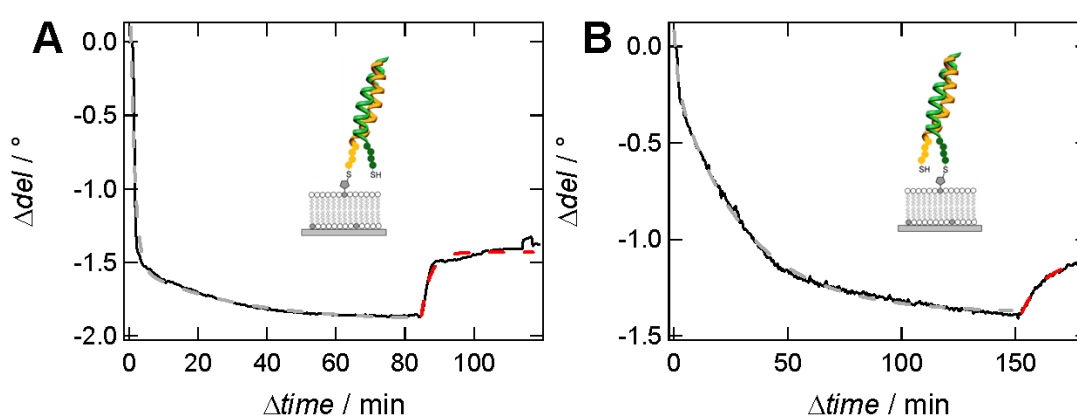


FIGURE V.7 Exemplary time-resolved ellipsometry data of coiled-coil formation with subsequent rinsing (black). Graphs are magnified views from corresponding parts shown in Figure V.6 B, SSM consisted of DOPC/MCCDOPE 90:10. Double exponential fits while adsorption phase are shown as grey scattered lines, exponential fits computing dissociation of coiled-coil complex are shown as red scattered lines. (A) Addition of *i*-K3Cys to *i*-E3Cys lipopeptides. (B) Addition of *i*-E3Cys to *i*-K3Cys lipopeptides.

All six peptide combinations show essentially the same qualitative kinetics of coiled-coil formation at the membrane interface (see also Table V.5). Across the board, the first fast binding step (τ_1) occurs within 0.3-1.6 min, while the second slower binding process (τ_2) needs at least 5 min. Notably, the amount of bound peptide within the fast adsorption regime depends strongly on the preparation protocol. Especially if *i*-K3Cys or *i*-K3PEG is employed as lipopeptide, the corresponding height increase A_1 during the fast time constant decreases significantly to 18 % and 47 %, respectively, while for all other peptide combinations A_1 is in a range of 75-93 %.

The calculated k_{off} values characterizing the dissociation induced through final rinsing is found to be in a range of $(1.5-7.0) \times 10^{-3} \text{ s}^{-1}$. Only the dissociation of E3Cys from LP-K3Cys displays a larger off-rate of $17.6 \times 10^{-3} \text{ s}^{-1}$ indicative of a decreased lifetime of coiled-coil motifs formed through this route.

	LP-K3Cys + E3Cys	LP-E3Cys + K3Cys*	LP- <i>i</i> -K3Cys + <i>i</i> -E3Cys	LP- <i>i</i> -E3Cys + <i>i</i> -K3Cys	LP- <i>i</i> -K3PEG + <i>i</i> -E3PEG	LP- <i>i</i> -E3PEG + <i>i</i> -K3PEG*
$\tau_1 / \text{min (A}_1)$	0.3 (75 %)	0.3 (83 %)	1.6 (18 %)	0.3 (78 %)	0.8 (47 %)	0.9 (93 %)
$\tau_2 / \text{min (A}_2)$	5.5 (25 %)	13.3 (17 %)	30.5 (82 %)	21.2 (22 %)	14.9 (53 %)	15.1 (7 %)
$k_{\text{off}} / 10^{-3} \text{s}^{-1}$	17.6	4.8	1.5	5.0	1.9	7.0*

TABLE V.5 Quantitative characterization of coiled-coil formation on DOPC/MCCDOPE 90:10 via double exponential fit (upper panel) with time constants τ_1 and τ_2 and corresponding height increases A . Off-rate k_{off} is calculated from τ determined via an exponential fit function to dissociation phase. *) DOPC/MCCDOPE 94:6 was used as SSM.

In summary, it can be concluded that all peptides form the expected lipopeptides and are capable of successive peptide heterodimerization on a membrane surface. E- and K-peptides exhibit significant different kinetics while *in situ* coupling process, leading to preferring K-lipopeptides over E-lipopeptides due to better handling.

V.3.2.2 Secondary Structure of Peptide Heterodimers on SSM¹⁵

Time-resolved ATR-FT IR spectroscopy was used to confirm and quantify successful formation of coiled-coil structures at the membrane interface concerning their secondary structure. For this purpose, covalent coupling to single solid supported membranes (SSM) deposited on the ATR-FT IR crystal was monitored prior to addition of the binding partner. An advantage of this method is that lipids and peptides show both strong absorption bands which do not overlap. Lipids have a characteristic band pattern in the regime of 2800-3000 cm^{-1} originating from the different stretching vibrations of the fatty acid alkyl chains (62). Furthermore, at around 1730 cm^{-1} a strong absorption of the carboxylate ester occurs, which is neighbored to the most prominent absorption band of peptides and proteins, the amide I band at around 1650 cm^{-1} (see also Chapter IV.1). In Figure V.8 the corresponding spectra are shown.

¹⁵ Parts of this Chapter are published in Gesa Pähler, Cornelia Panse, Ulf Diederichsen and Andreas Janshoff "Coiled-coil formation on lipid bilayers-implications for docking and fusion efficiency", *Biophysical Journal* **2012**, 103, 2295-2303.

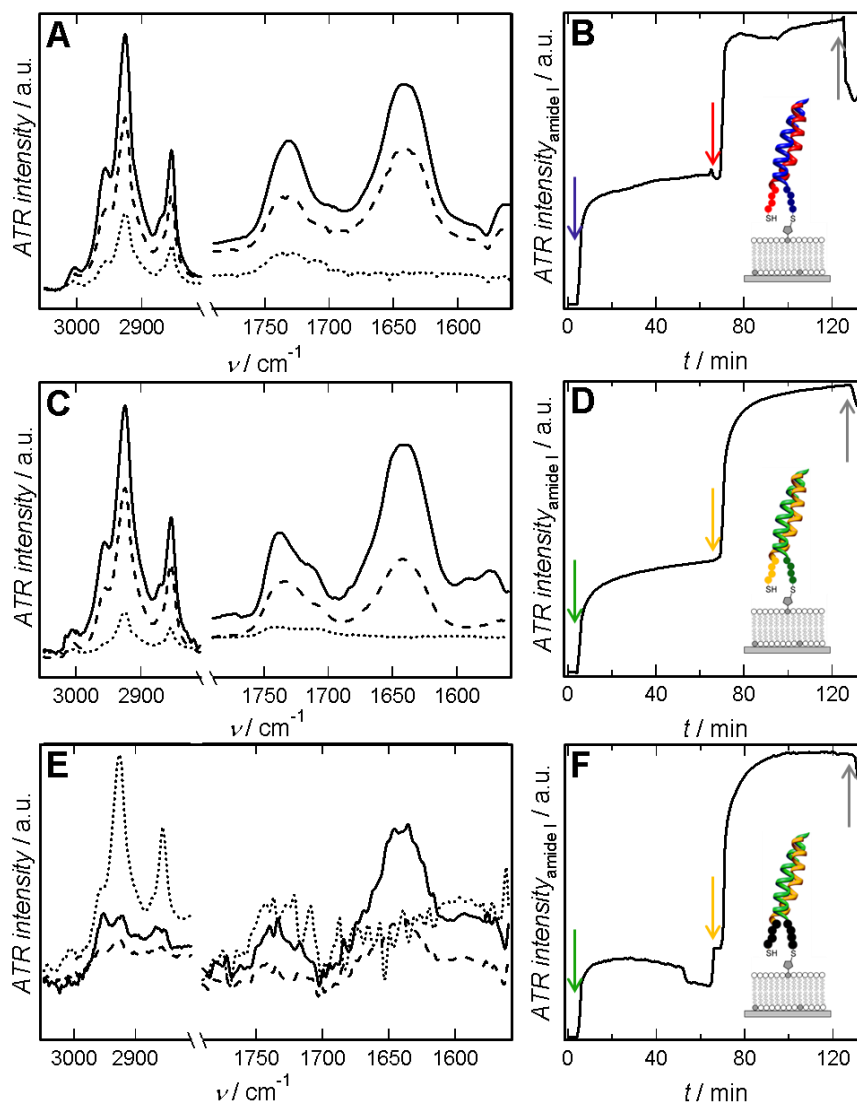


FIGURE V.8 (left panel) ATR-FT IR spectra of plain solid supported membranes (.....) consisting of DOPC/MCCDOPE 90:10 in D₂O with 50 mM NaCl spread on a Si-covered ZnSe-crystal. Lipid bands and amide I region are shown. Lipopeptides were formed with K-peptides covalently attached to the maleimide headgroups of MCCDOPE (- - -). Solid lines indicate spectra after coiled-coil formation upon addition of E-peptides (—). (right panel) Time course of lipopeptide coupling reaction followed by coiled-coil formation shown left: Intensity of amide I band is plotted vs. time. Time course starts with completed bilayer ($t = 0$). Addition of peptides and rinsing is indicated by arrows. (A, B) SSM + K3Cys (lipopeptide, blue arrow) + E3Cys (red arrow). (C, D) SSM + *i*-K3Cys (lipopeptide, green arrow) + *i*-E3Cys (yellow arrow). (E, F) SSM + *i*-K3PEG (lipopeptide, green arrow) + *i*-E3PEG (yellow arrow). In (E) lipid peaks are only present in spectrum directly after spreading, because this spectrum was subtracted from the two other shown here due to water vapor correction.

In the course of the experiment, a bilayer consisting of DOPC/MCCDOPE 90:10 was prepared on the ATR crystal. Subsequently, K-peptides were coupled covalently to the surface using maleimide chemistry covering a large portion of the surface. Finally, coiled-coil structures were formed on the bilayer by addition of the corresponding peptide. The successful coupling and heterodimerization of the peptides is visible in the spectra due to the increasing intensity of the

amide I band. The experiment was carried out using a flow cell, hence, the intensity of amide I band can be followed in a time-dependent fashion (see Fig. V.8, *right panel*). The lipopeptide coupling reaction as well as the coiled-coil formation is detected by a steep increase of amide I intensity. Rinsing the surface with buffer results in partial dissolution of the complexes, as it was already observed in the ellipsometry measurements shown in the previous chapter.

By the means of an internal analyses (QUANT2, see Chapter IV.1.2), the amount of α -helical content can be followed during coiled-coil formation on the ATR crystal, while the integral of the amide I band is correlated with the peptide concentration on the surface (see Fig. V.9). Upon addition of E-peptide, the α -helical content increases following similar kinetics as observed in ellipsometry experiments (see Chapter V.3.2.1). Again, a two-step dimerization process is observed, characterized by a fast time constant with significant binding, followed by a slow saturation phase, where additional peptide is coupled to the lipopeptide functionalized membrane. The defined increase of helical structuring is a clear hint that also on a solid supported membrane with its constricted geometry a coiled-coil formation can be achieved.

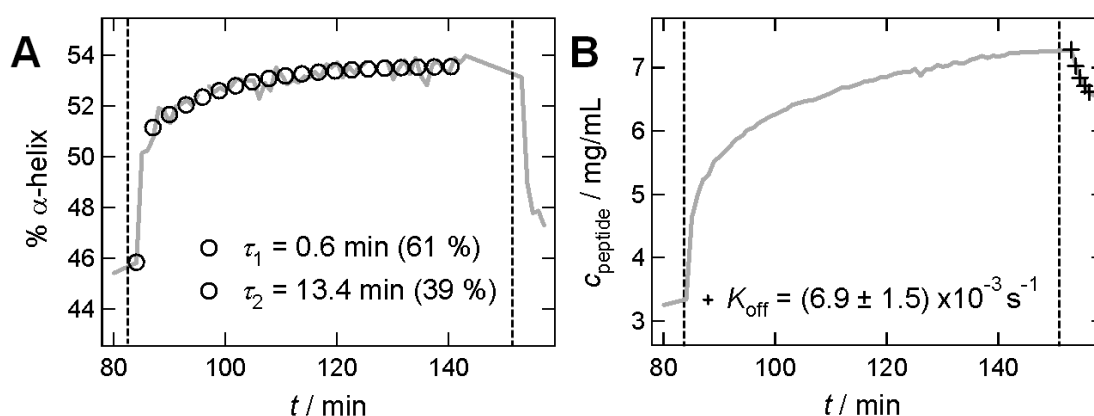


FIGURE V.9 Time-resolved ATR-FT IR spectroscopy of coiled-coil formation. Plots show α -helical content (A) and protein concentration in evanescent field (B). Spectral data was analyzed using QUANT2, a software provided by Bruker Optics. SSM was formed from DOPC / MCCDOPE 90:10 SUV, then *i*-K3PEG was covalently attached to the bilayer via maleimide chemistry. Afterwards, *i*-E3PEG was added in solution. Only coiled-coil formation of LP-*i*-K3PEG with *i*-E3PEG is shown in graph, scattered lines indicate beginning and end of dimerization. Before and after peptide addition, sample was rinsed with D₂O (with 50 mM NaCl). Grey curves represent experimental data, black circles show biexponential fit function while coiled-coil formation (A), black crosses in (B) show monoexponential fit function for rinsing off peptide.

The determined concentrations (see Fig. V.9, B) cannot be related to exact amount of peptide present in the experiment, because only the substance inside the evanescent field is detected. But since molecules which are located closer to the surface of the ATR crystal are detected with higher intensity than bulk material, the actual binding process can be followed. The curve shows

the expected increase in peptide concentration upon coiled-coil formation. Furthermore, a defined decrease while dissociation phase induced by final rinsing is observed here, which can be described by a monoexponential function to determine a k_{off} value, which is in good agreement to the off-rate calculated from ellipsometry data ($k_{\text{off}}(\text{ellipsometry}) = 1.9 \times 10^{-3} \text{ s}^{-1}$).

To prove the actual formation of coiled-coil structures on lipid bilayers, amide I bands determined from ATR-FT IR spectroscopy measurements were deconvoluted following the descriptions of Heimburg *et al.* (67) (see Fig. V.10; compare with Chapter V.2.1). Bilayers were prepared on an ATR crystal mounted in a Bio-ATR cell. The resulting ATR-FT IR spectra showed essentially the same amide I band separation as in solution (compare with Fig. V.3), which is also in good accordance with a recent study using gp41 derived peptides (81, 100). As a consequence, we can safely assume that coiled-coil formation occurs also at the membrane interface (see Fig. V.10).

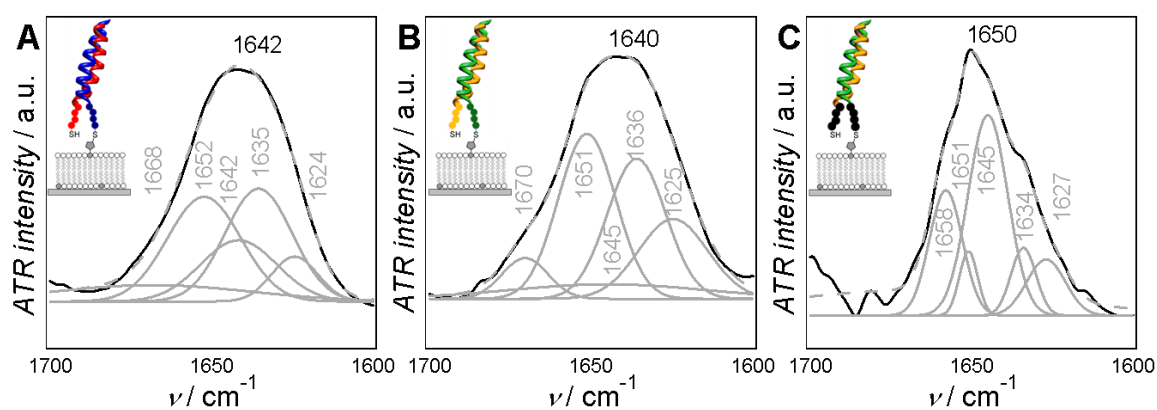


FIGURE V.10 Deconvolution of amide I band for coiled-coil build of LP-K + E-peptides on DOPC/MCCDOPE 90:10 in D_2O with 50 mM NaCl spread on a Si-covered ZnSe-crystal. Spectra were collected using an ATR-FT IR spectroscopy setup. Numbers in graph indicate position of band maxima. Single Gaussian fits are shown in grey, amide I band of spectra in black. Scattered grey lines represent the sum of all Gaussian fits. (A) SSM + K3Cys (lipopeptide) + E3Cys. (B) SSM + *i*-K3Cys (lipopeptide) + *i*-E3Cys. (C) SSM + *i*-K3PEG (lipopeptide) + *i*-E3PEG.

The spectral maximum for coiled-coil complexes made of LP-K3Cys/E3Cys and LP-*i*-K3Cys/*i*-E3Cys attached to a lipid bilayer are shifted to smaller wavenumbers, *i.e.* 1642 cm^{-1} and 1640 cm^{-1} instead of 1647 cm^{-1} and 1645 cm^{-1} in solution, respectively. Interestingly, the described shift of amide I peak position is not observed for the PEGylated analogs of the peptides. The peak position remains nearly unchanged comparing the amide I band of heterodimeric complexes in solution compared to the one attached to a membrane. A possible explanation concerning this difference might be the slightly changed hydrophilic character of the molecules due to the PEG residues. However, the spectrum of amide I band shown in Figure V.10 C exhibits some

interfering signals due to water vapor; hence the observed effects might be also related to an experimental error.

The shift of spectral maximum observed here for the unPEGylated coiled-coil complexes can be correlated to a decrease in superhelical pitch length. While for the heterodimerization in solution, a distance of $\approx 200 \text{ \AA}$ was determined, the superhelical pitch length decreases to $\approx 170 \text{ \AA}$ for coiled-coil complexes attached to membrane surfaces. This finding can be attributed to a reduced configurational freedom and steric hindrance caused by the covalent attachment of one peptide to the lipid bilayer. Nevertheless, it could be proven that the actual coiled-coil formation is not hindered concerning their secondary structure build-up.

V.3.2.3 Specificity and Quantification of Lipopeptide Formation¹⁶

In this part the focus is laid on solely the lipopeptide formation during *in situ* coupling reaction. Since the amount of receptor lipids MCCDOPE can be controlled during bilayer formation, the amount of subsequent formed hybrid structures will be quantified here in detail. Therefore, SSM with different contents of MCCDOPE were produced and K-peptides were coupled to the surface to determine the apparent layer thickness by the means of ellipsometry. Furthermore, employed K-peptide concentration was varied to define a minimal amount needed to assure a complete saturation of presented receptor lipids (see Fig. V.11).

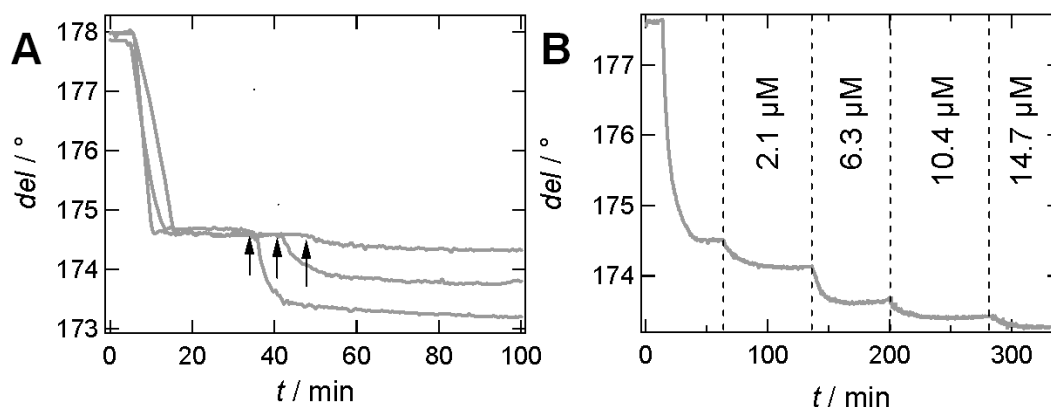


FIGURE V.11 Time-resolved ellipsometry data determined on silica in PB 6.8. (A) *In situ* coupling of *i*-K3PEG to DOPC/MCCDOPE bilayers with the compositions 92:8, 94:6, and 98:2 (from left to right, arrows mark point of peptide addition). (B) *i*-K3PEG added in increasing concentrations (see graph) to a SSM made of DOPC/MCCDOPE 90:10.

¹⁶ Parts of this Chapter are published in

Gesa Pähler, Cornelia Panse, Ulf Diederichsen and Andreas Janshoff "Coiled-coil formation on lipid bilayers-implications for docking and fusion efficiency", *Biophysical Journal* **2012**, *103*, 2295-2303.

From Figure V.11 A it can be clearly seen that the height increase due to lipopeptide coupling reaction is correlated with the presented amount of receptor lipids. With only 2 mol% MCCDOPE in the spreaded SSM, an apparently thinner peptide layer compared to 6 mol% or 8 mol% is achieved. This is due to an increasing coverage of the bilayer. Similar can be seen in Figure V.11 B, where with only 2.1 μM of added peptide, no full coverage of the SSM is achieved. Hence, after increasing the peptide concentration, another decrease of principal angle del can be observed. After the addition of 14.7 μM , no further decrease of del could be achieved through an increase of concentration. Since in all other experiments in this thesis, concentrations of $\approx 50 \mu\text{M}$ were applied, a maximal saturation of offered receptor lipids can be safely assumed.

The apparent layer thickness depending on the amount of offered receptor lipids in the solid supported membrane was further analyzed and quantified concerning its specificity. Therefore, the height increase correlated to a defined concentration of MCCDOPE was determined (see Fig. V.12).

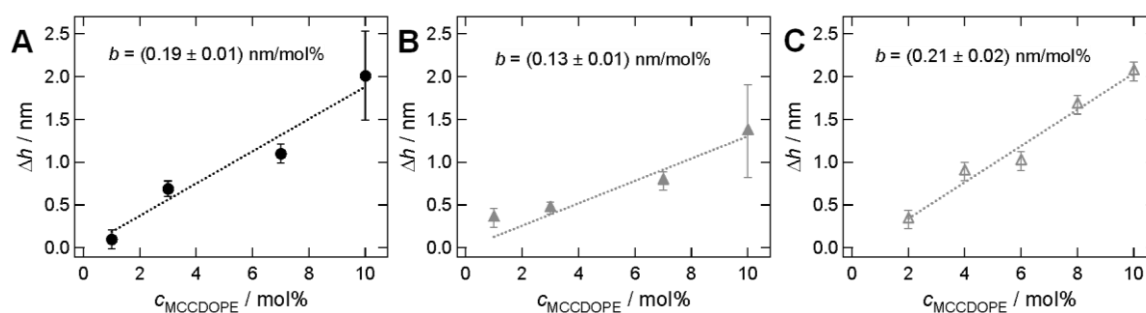


FIGURE V.12 Layer thickness of K-peptides (markers) added to SSM containing different amounts of MCCDOPE. Presented values b are the corresponding slopes of the linear regression (dotted lines). Mean values with their standard deviation are given. (A) LP-K3Cys formation. (B) LP-*i*-K3Cys formation. (C) LP-*i*-K3PEG formation (no mean values were calculated here, error corresponds to instrumental error).

Due to variation of the used amount of MCCDOPE within the SSM in a range of 1-10 mol%, a linear increase of the apparent height for the thin film after addition of K-peptides is determined. The slope b of corresponding fit functions can be interpreted as an increase of apparent layer thickness per employed mol% of receptor lipids. While for K3Cys and *i*-K3PEG, b is determined to be around 0.2 nm/mol%, the value is reduced for *i*-K3Cys to 0.13 nm/mol%. This is actually consistent with the findings from Chapter V.3.2.1, where also for *i*-K3Cys the lowest layer thickness was determined in comparison to the other applied K-lipopeptides.

To quantify the impact of non-specific interaction of peptides with membranes lacking receptor molecules like MCCDOPE or lipopeptides, E- and K-peptides were added to neat DOPC bilayers.

Hereby, time-resolved experiments employing ellipsometry and ATR-FT IR spectroscopy were carried out (see Fig. V.13).

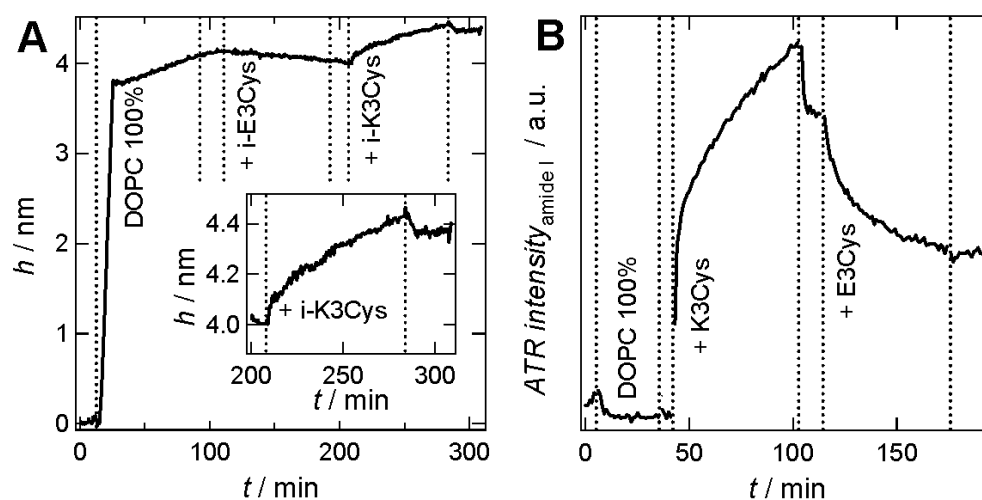


FIGURE V.13 Controls with neat DOPC membranes. Before and after each step (indicated by scattered lines) samples were rinsed with buffer. (A) Layer thicknesses calculated from ellipsometry measurements (in PB 6.8) of bilayer spreading (DOPC 100 %) with subsequent addition of i -E3Cys and afterwards i -K3Cys (i -K3Cys addition shown magnified in inset). (B) Time course of ATR-FT IR flow cell measurement in $D_2O + 50mM NaCl$. Intensity of amide I band is shown while bilayer spreading (DOPC 100 %) with subsequent addition of K3Cys and afterwards E3Cys.

For E-peptides no interaction with pure DOPC is observed. However, K-peptides adhere transiently to plain phosphocholine lipid bilayers. This effect can be attributed to the opposed net charges of the peptides. E-peptides are negatively charged (-3), while K-peptides carry a net charge of +3. Moreover, the kinetics of adsorption is considerably slower than in the case of specific *in situ* coupling. After more than 1 h, no saturation can be observed for the non-specific interaction, whereas for the formation of covalent bonds equilibrium is reached after ≈ 30 min. From Figure V.13 B it is obvious that addition of corresponding E-peptide reverses the effect of adhesion in contrast to the covalently coupled lipopeptides; here, a further increase was observed (see Chapter V.3.2.2). This leads to the conclusion that coiled-coil formation in solution is thermodynamically favored in comparison to electrostatic interaction of K-peptides to phospholipids. Interestingly, non-specific adsorption of K-peptides is absent if small amounts of MCCDOPE are present in the bilayer (compare Fig. V.12). Extrapolating the linear response to zero receptor lipids suggests that non-specific adsorption is negligible. Therefore, our determined responses presented during the characterization of peptide-membrane interaction can be solely attributed to peptide coverage.

V.4 Discussion

In this chapter, some important prerequisites for following experiments were proven. Membrane spreading was analyzed in the absence and presence of cholesterol, leading to detailed knowledge of SSM characteristics. It could be shown that the minimal model system of K- and E-peptides forms coiled-coil complexes in parallel as well as in antiparallel orientation. Furthermore, this heterodimerization process is not affected by the covalent coupling of peptides to lipid bilayers. The lipopeptide formation via maleimide chemistry employing an *in situ* coupling reaction was established with high specificity, however coupling kinetics are very different comparing E- and K-peptides. This is explained with the opposing charges of the two different peptide types, whereat the positive charge of K-peptides promotes the adhesion and subsequent binding to lipid bilayers.

For coiled-coil complex formation on SSM, a two-step mechanism was found, consisting of a fast and a slow time constant depending on the presented lipopeptide. Possible reasons might be a defined structuring of hybrid lipopeptides in the SSM, inducing a kinetic response depending also on a lateral reorganization time constants. A sufficient explanation of this observation cannot be given here, but will be discussed in detail in Chapter VII.

VI Thermodynamics of Parallel and Antiparallel Coiled-coil Formation on Lipid Bilayers¹⁷

In the following section, parallel and antiparallel coiled-coil formation of four different oligopeptides was characterized concerning their thermodynamics in solution, at hydrogels (Chapter VI.2) and on membranes (Chapter VI.3). Therefore, *i*-K3Cys and *i*-E3Cys, peptides which were synthesized in reversed sequence to K3Cys and E3Cys, were employed. Coiled-coil formation in solution as opposed to association at the membrane surface displays considerably larger binding constants that are largely attributed to loss of translational entropy at the interface (Chapter VI.3.2). Finally, the fusogenicity of the various coiled-coil motifs was explored providing clear evidence that hemifusion followed by full fusion requires a parallel orientation of α -helices, while antiparallel oriented coiled-coil formation displays merely docking (Chapter VI.4).

VI.1 Introduction

Recently, Smith and Weisshaar (101) suggested that docking rather than fusion is the rate limiting step in SNARE driven membrane fusion assays, putting the focus on the initial contact of two bilayers. Hence, many collisions may be required until a docked pair of two vesicles forms. Li and coworkers determined the energetics and dynamics of SNARE protein folding upon coiled-coil formation to be $35 k_B T$ (27), a folding energy which is close to the proposed energy needed for membrane fusion ($\approx 50 k_B T$) (9, 102). Enhancement of the overall rate might be only achieved by more efficient docking.

Here, we investigate thermodynamics and kinetics of coiled-coil formation between the peptides with either E- or K-sequence (E3Cys and K3Cys) taking place in solution and at lipid bilayers. By inverting the primary sequence of recognition domain (*i*-E3Cys and *i*-K3Cys) we were able to compare coiled-coil forming peptides with different superhelical macro-dipoles and a predominantly parallel or antiparallel orientation concerning their thermodynamic characteristics and their fusogenicity (see Fig. VI.1).

¹⁷ Main parts of this Chapter are published in Gesa Pähler, Cornelia Panse, Ulf Diederichsen and Andreas Janshoff "Coiled-coil formation on lipid bilayers-implications for docking and fusion efficiency", *Biophysical Journal* **2012**, *103*, 2295-2303.

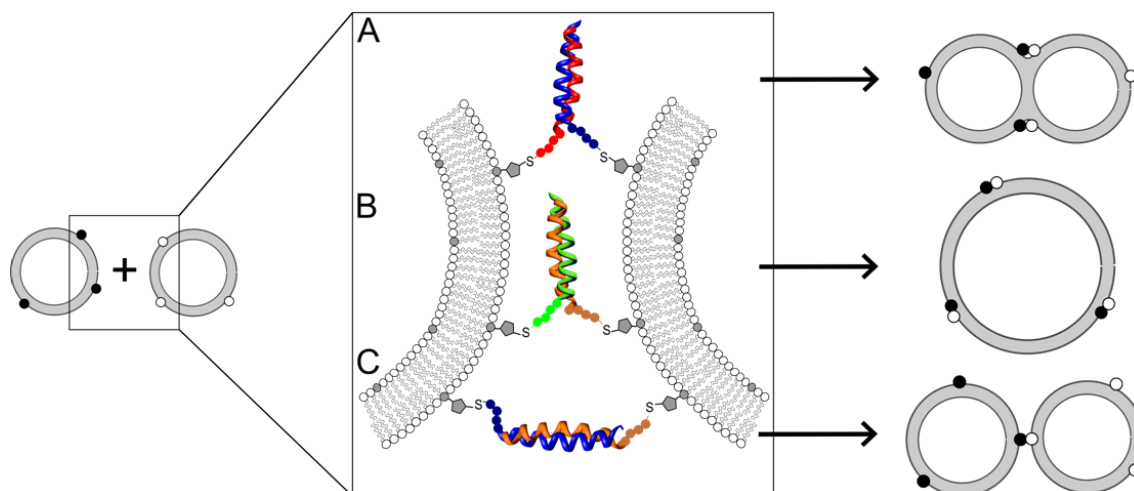


FIGURE VI.1 Schematic drawing of peptide-mediated membrane-membrane interaction through coiled-coil formation. Parallel coiled-coil formation of peptides E3Cys and K3Cys (A) and inverted peptides *i*-E3Cys and *i*-K3Cys (B), respectively, are envisioned to be capable of inducing lipid mixing like hemifusion or fusion, while for antiparallel coiled-coil formation (C) only docking events are expected.

While Monera *et al.* (103) showed that, in the case of similar electrostatic interactions, antiparallel coiled-coils are more stable, Lygina *et al.* (32) could prove that a parallel orientation of peptide hybrids leads to a higher fusogenicity. We found that all peptidic dimers display approximately identical binding affinities, but coiled-coil formation in the context of membranes generates less free energy compared to complexation in solution due to loss in translational degrees of freedom. Additionally, a closer proximity of membranes is achieved through formation of parallel coiled-coils. In conclusion, one can state that parallel coiled-coil formation eventually results in fusion, while antiparallel coiled-coils only exhibit docking events.

VI.2 Thermodynamics of Pure Peptides in Solution and on Hydrogels

Thermodynamics of the formation of parallel- and antiparallel-aligned coiled-coil dimers composed of E- and K-peptides was scrutinized in solution and on hydrogels using CD and SPR spectroscopy. We focused on determining the substance specific dissociation constant K_D which can be correlated with the gain in free energy due to coiled-coil formation. These thermodynamic information are used to reveal a possible orientation dependency concerning parallel and antiparallel dimerization.

After heterodimerization, the coiled-coil forming peptides are mainly α -helical, hence the CD spectra show one maximum at 190 nm and two distinct minima at 208 nm and 220 nm (compare Chapter V.2). The intensity of this ellipticity at 220 nm can be used to determine the dissociation

constant of coiled-coil complexes by dilution experiments (see Fig. VI.2). Here, successive reduction of peptide concentration leads to a dissociation of coiled-coil assemblies, which results in a corresponding decrease of the α -helix content (75).

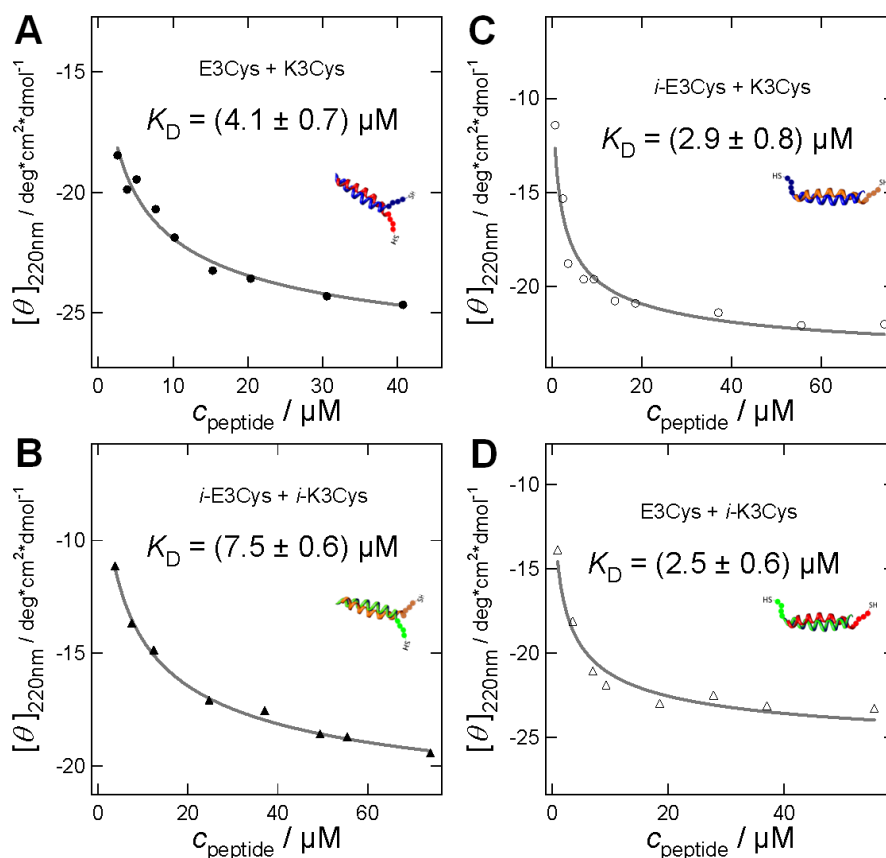


FIGURE VI.2 Concentration dependent of $[\theta]_{\text{MRW}}$ at 220 nm measured by CD spectroscopy for heterodimeric coiled-coil mixtures to determine K_D via dilution experiments. On left side parallel, on right side antiparallel coiled-coil formation are shown. (A) Data for dimer formed of E3Cys and K3Cys; solid circles. (B) Dimer formed of *i*-E3Cys and *i*-K3Cys; solid triangles. (C) Dimer formed of *i*-E3Cys and K3Cys; open circles. (D) Dimer formed of E3Cys and *i*-K3Cys; open triangles. Resulting K_D values are presented with corresponding fits shown as grey lines (75).

The measured concentration dependent ellipticity $[\theta]_{220\text{nm}}$ can be determined as described by equation IV.6 (see Chapter IV.2.2.2). Besides the dissociation constant K_D , the ellipticity for a monomeric unfolded peptide and the maximum ellipticity for a complete coiled-coil structure need to be specified. Hence, we determined the minima at 220 nm for an unfolded peptide from the CD spectra of single peptides before dimerization and used this value in the fit function, while the maximum ellipticity is determined from fitting the data. Notably, the resulting dissociation constants for the lowest peptide concentrations are intrinsically inaccurate due to the low signal-to-noise ratio. The dissociation constants determined for inverted and non-inverted peptides leading both to parallel aligned dimeric coiled-coil structures are in the lower

μM -regime. The K_D for a coiled-coil formed of *i*-K3Cys and *i*-E3Cys ($K_D = (7.5 \pm 0.6) \mu\text{M}$) is nearly twice the K_D found for K3Cys and E3Cys ($K_D = (4.1 \pm 0.7) \mu\text{M}$). The values for an antiparallel packing, thus dimerization of K3Cys and *i*-E3Cys or *i*-K3Cys and E3Cys, respectively, are found to be generally smaller but very similar for both coiled-coil heterodimers ($K_D(\text{K3Cys}/i\text{-E3Cys}) = (2.9 \pm 0.8) \mu\text{M}$; $K_D(i\text{-K3Cys}/\text{E3Cys}) = (2.5 \pm 0.6) \mu\text{M}$). Literature values for K_D of the non-inverted coiled-coil complexes using similar sequences were reported to be between 10^{-7} - 10^{-8} M employing CD spectroscopy, ITC measurements (90), and guanidine hydrochloride denaturation studies (48) are smaller by one order of magnitude, which we attribute to the inherent inaccuracy of the method as well as a slightly different peptide sequences.

Additionally, due to the limited signal to noise ratio of CD spectroscopy at low peptide concentrations, SPR spectroscopy measurements were carried out. Thereby, in addition to thermodynamic values from isotherm data, we are able to measure adsorption and desorption kinetics (104) by focusing on specific association and dissociation phases (see Fig. VI.3).

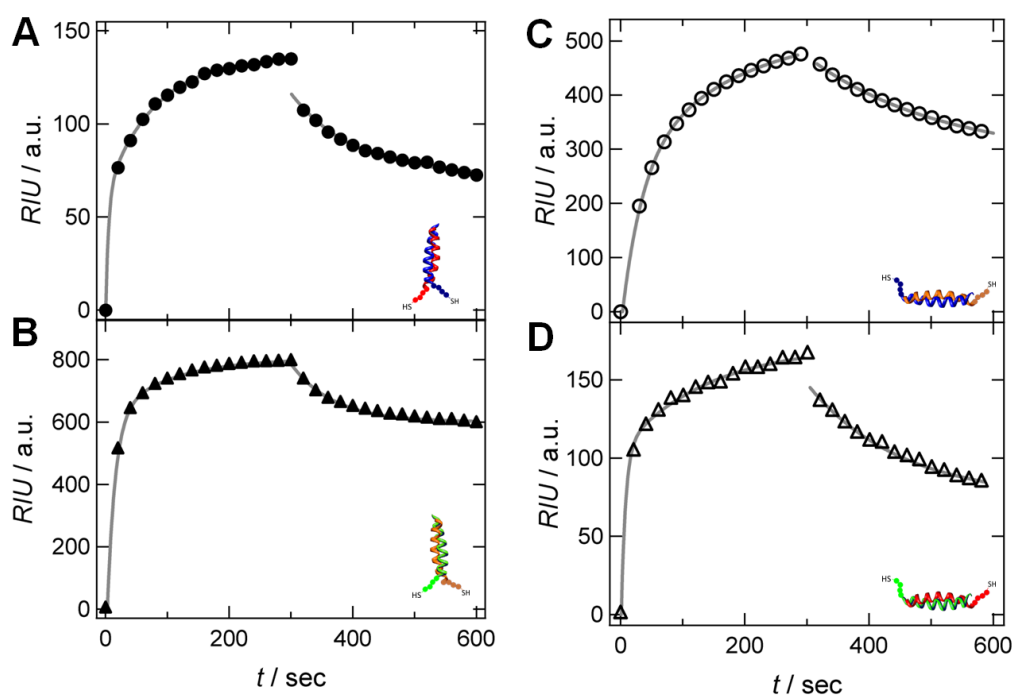


FIGURE VI.3 Association ($t = 0\text{-}300$ s) and dissociation ($t = 300\text{-}600$ s) of E-peptides coupled to immobilized K-peptides on a hydrogel monitored with SPR spectroscopy. E-peptides were added at a concentration of $15 \mu\text{M}$. On left side parallel, on right side antiparallel coiled-coil formation are shown. Association of peptides is described by the rate of assembly k_{on} , while dissociation of the peptide assembly follows a monoexponential function (k_{off}). Fits are shown as grey lines, for corresponding values see Table VI.1. (A) E3Cys added to immobilized K3Cys (solid circles). (B) *i*-E3Cys added to immobilized *i*-K3Cys (solid triangles). (C) *i*-E3Cys added to immobilized K3Cys (open circles). (D) E3Cys added to immobilized *i*-K3Cys (open triangles).

Coiled-coil formation can be best described by a double exponential time dependence (τ_a , τ_b), where the smaller time constant τ_a provides k_{on} , describing the prevailing interaction. Dissociation of the dimers could be fitted with a mono-exponential function providing the off rate k_{off} . The dissociation constant K_D can be calculated as a quotient of these two time dependent constants (see Table VI.1; for detailed description of analytical workup see Chapter IV.3.1).

	K3Cys + E3Cys	<i>i</i> -K3Cys + <i>i</i> -E3Cys	K3Cys + <i>i</i> -E3Cys	<i>i</i> -K3Cys + E3Cys
$k_{on} / \text{M}^{-1}\text{s}^{-1}$	$(2.2 \pm 1.3) \times 10^4$	$(7.9 \pm 4.3) \times 10^3$	$(1.2 \pm 0.9) \times 10^4$	$(8.9 \pm 4.7) \times 10^3$
k_{off} / s^{-1}	$(8.4 \pm 1.5) \times 10^{-2}$	$(1.3 \pm 0.2) \times 10^{-3}$	$(4.1 \pm 0.8) \times 10^{-3}$	$(6.8 \pm 1.1) \times 10^{-3}$
$K_D / \mu\text{M}$	0.5 ± 0.3	2.3 ± 1.8	0.5 ± 0.3	1.2 ± 1.0

TABLE VI.1 Thermodynamic constants determined from SPR: Double-exponential fit to association phase provides τ_a and k_{on} , exponential fit to dissociation phase provides k_{off} . Therefore, resulting dissociation constant K_D can be derived.

The resulting K_D -values computed from kinetic data at various peptide concentrations are smaller but still in the same regime as the dissociation constants determined by CD spectroscopy. SPR reveals K_D values in the low μM -range, with a significantly lower dissociation constant for the coiled-coil formed with K3Cys tethered to the hydrogel. Both, the parallel coiled-coil formation with E3Cys as well as the antiparallel coiled-coil formation with *i*-E3Cys show a K_D of $(0.5 \pm 0.3) \mu\text{M}$. In comparison, coiled-coil formation with tethered *i*-K3Cys is characterized by higher K_D values. Here, the antiparallel heterodimerization with E3Cys gives a K_D of $(1.2 \pm 1.0) \mu\text{M}$, while the dissociation constant for the parallel heterodimer formed with *i*-E3Cys was found to be $(2.3 \pm 1.8) \mu\text{M}$.

Since all dissociation constants from the various peptide combinations determined with two independent methods, are approximately in the same regime, we can conclude that coiled-coil formation is rather independent of helix orientation. This is remarkable, because Monera *et al.* (103) reported that antiparallel coiled-coil structures are more stable when similar electrostatic interactions are given. However, the authors used cysteine-bridged peptides for their denaturation studies, *i.e.* the two helices were covalently coupled to each other, imposing constraints we do not need in our setup. Since the electrostatic interactions at the *e* and *g* positions are always between lysine and glutamic acid residues, we attribute the difference between their findings and ours to differences in entropy changes upon assembly / disassembly due to constraining disulfide-bridges, which covalently couples the two coiled-coil forming peptides.

VI.3 Thermodynamics on Solid Supported Membranes

Solid supported membranes display a more constricted geometry to peptide assembly experiments than ones in solution, because coiled-coil heterodimerization has to take place on a two-dimensional surface. Therefore, thermodynamics are scrutinized on SSM by the means of adsorption isotherms carried out by ellipsometry (Chapter VI.3.1). We found a distinct loss of binding energy compared to solution experiments, which we attribute to a loss of entropy (Chapter VI.3.2).

VI.3.1 Adsorption Isotherms

For a detailed view concerning thermodynamics in membrane-membrane interaction, it is important to compare the results from solution experiments shown in Chapter VI.2 with peptides which are covalently bound to lipid bilayers. Therefore, adsorption isotherms were measured with the ellipsometer to quantify the binding affinity between E- and K-peptides as lipopeptides. For the analysis of resulting isotherms, the theories of Langmuir and Bragg-Williams were employed (82) (see Chapter IV.4.2).

Prior to the experiments, a SSM containing a specific amount of MCCDOPE receptor lipids was spread on silica and monitored by time-resolved ellipsometry. Afterwards, first peptide was coupled covalently to the surface using maleimide chemistry. Then the actual adsorption isotherm was monitored by steadily increasing the concentration of coiled-coil forming peptide, resulting in a concomitant increase in apparent thickness corresponding to an increase in peptide coverage on the bilayer. The resulting concentration dependent layer thickness can be described employing Langmuir functions. First, we compare different preparation pathways, *e.g.* E-peptide addition to K-lipopeptides and *vice versa*. Furthermore, the impact of receptor lipid density is tested via variation of MCCDOPE concentration in the pre-formed spreaded solid supported bilayer (see Fig. VI.4).

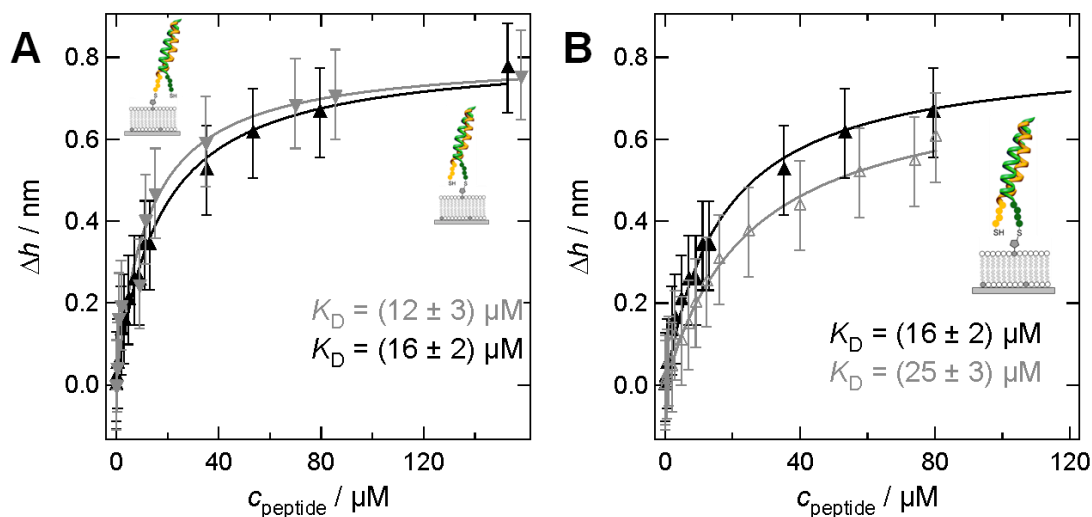


FIGURE VI.4 Langmuir adsorption isotherms determined with ellipsometry represent coiled-coil formation of *i*-K3Cys and *i*-E3Cys. Solid triangles represent the measured data points while solid lines represent corresponding fit functions. (A) Comparison of the preformed lipopeptide (LP-) on a DOPC/MCCDOPE 90:10 lipid bilayer in PB 6.8. Addition of *i*-K3Cys to LP-*i*-E3Cys is shown in grey, addition of *i*-E3Cys to LP-*i*-K3Cys is shown in black. (B) Addition of *i*-E3Cys to LP-*i*-K3Cys on a SSM formed of DOPC/MCCDOPE 90:10 (black) and of DOPC/MCCDOPE 97:3 (grey).

In graph VI.4 A, the addition of *i*-K3Cys to LP-*i*-E3Cys is compared to the addition of *i*-E3Cys to LP-*i*-K3Cys. Both dissociation constants are higher than the determined values from solution experiments, corresponding to a lower gain in energy for coiled-coil formation on SSM, but in the same regime concerning their preparation protocol. The K_D value determined for *i*-E3Cys added to LP-*i*-K3Cys is slightly higher, but still well comparable regarding the corresponding range of inaccuracy. Hence, for the following experiments, K-peptides were employed for membrane functionalization due to their faster binding kinetics during *in situ* coupling.

Comparing different amounts of MCCDOPE in the lipid bilayer, as shown in Figure VI.4 B, leads to a similar picture concerning the determined dissociation constant K_D : with only 3 mol% of receptor lipids present in the SSM (instead of 10 mol% as before) the energy released upon coiled-coil formation decreased further, visible in the increase of K_D from 16 μM to 25 μM . However, the calculated maximal height Δh_{max} is reduced from 0.82 nm for 10 mol% MCCDOPE to 0.75 nm for 3 mol%. This is consistent with our expectations, since less peptide is coupled to the surface, resulting in a decreased apparent layer thickness.

However, the observed increase of K_D with decreasing amount of MCCDOPE is surprising, since less steric hindrance is expected and therefore heterodimerization process should be facilitated in comparison to a SSM which is completely covered with lipopeptides. This effect is further

analyzed in the following adsorption isotherms, which compare parallel and antiparallel coiled-coil formation. Therefore, we employed also 3 mol% of receptor lipid in the bilayer. The resulting maximum layer thickness Δh_{\max} and the dissociation constant K_D were determined by fitting the data with a Langmuir adsorption isotherm or a Bragg-Williams isotherm. In the latter one, the regression reflects the sigmoid shape of one of the experimental data, which is indicative of a slightly cooperative binding (100). In our experiments, only the antiparallel interaction of LP-K3Cys with *i*-E3Cys shows a Bragg-Williams behavior with a marginal cooperativity of $\chi = 1.2$, the other three analyzed coiled-coil formations can be fitted with high accuracy using the Langmuir equation (see Fig. VI.5).

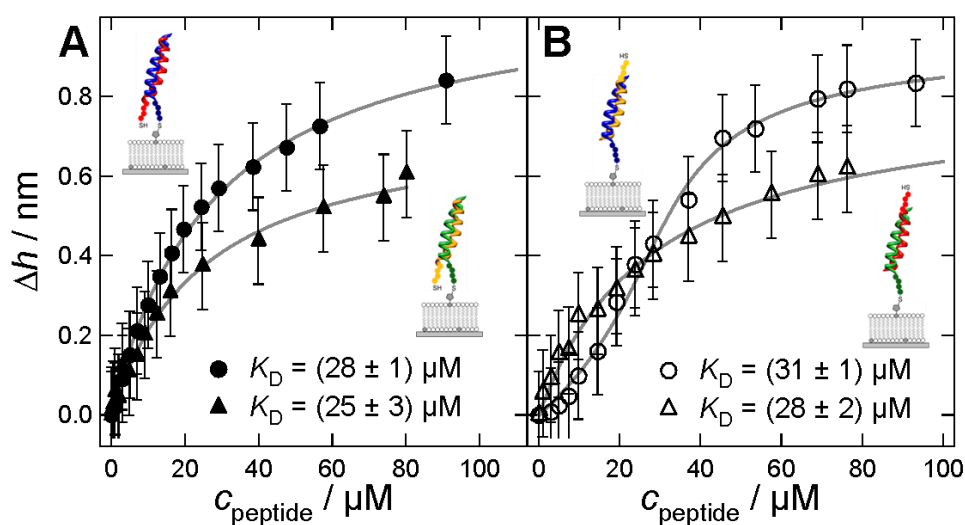


FIGURE VI.5 Ellipsometry adsorption isotherms representing coiled-coil formation of E-peptides binding to K-lipopeptides. Bilayers were formed from DOPC/MCCDOPE 97:3, afterwards K-peptides were coupled covalently to the surface. The isotherm was measured by subsequently increasing the added E-peptide concentration. (A) Parallel coiled-coil formation. Solid circles: LP-K3Cys + E3Cys; solid triangles: LP-*i*-K3Cys + *i*-E3Cys; data were fitted according to Langmuir (fits: grey line). (B) Antiparallel coiled-coil formation. Open circles: LP-K3Cys + *i*-E3Cys; open triangles: LP-*i*-K3Cys + E3Cys; data were fitted according to Langmuir theory for LP-*i*-K3Cys + E3Cys, while for LP-K3Cys + *i*-E3Cys a Bragg-Williams isotherm was used (fits: grey line).

Here, it is getting obvious that not only the amount of MCCDOPE present in the SSM determines the overall height found for coiled-coil assembly, but also the peptide sequence coupled to the bilayer. Using K3Cys as a lipopeptides produces a change in layer thickness of $h_{\max} = 1.1 \text{ nm}$ (LP-K3Cys + E3Cys) and $h_{\max} = 0.95 \text{ nm}$ (LP-K3Cys + *i*-E3Cys), respectively, due to formation of coiled-coil dimers on the lipid bilayer. In contrast, if *i*-K3Cys is used to form the lipopeptide, the maximum layer thickness amounts merely to $h_{\max} = 0.75 \text{ nm}$ (LP-*i*-K3Cys + *i*-E3Cys) and $h_{\max} = 0.82 \text{ nm}$ (LP-*i*-K3Cys + E3Cys), respectively. It should be noted that after formation of the complete heterodimeric layer on the SSM, all measurements displayed roughly the same layer

thicknesses. Hence, we attribute those differences in h_{\max} to a different folding and α -helix propensity of the peptides coupled to the lipid. It is conceivable that peptides that display a more random coil-like structure are less stiff and therefore less receptive to form dimers at the interface. In general, these values are not to be mistaken as a dimensional size of coiled-coil complexes, because with only 3 mol% of MCCDOPE as an anchor lipid in the bilayer, no complete surface coverage by peptide coupling can be achieved.

In summary, no significant difference of the dissociation constant between antiparallel and parallel coiled-coil formation at the membrane interface was found. All isotherms display a similar affinity between E- and K-peptides with K_D -values ranging between 25 μM and 31 μM . Notably, all dissociation constants determined with 3 mol% of receptor lipid are higher than the K_D value determined for a complete covered SSM; hence, steric hindrance cannot solely be the explanation for the loss of energy upon heterodimerization.

VI.3.2 Loss of Entropy

Compared to measurements of peptide dimerization in solution (CD spectroscopy) or within a hydrogel (SPR spectroscopy), the K_D -values found for coiled-coil dissociation at the membrane interface increased by one order of magnitude. This corresponds to a decrease of 3-4 $k_B T$ following equation VI.1 to determine the released free energy ΔG° upon coiled-coil formation.

$$\Delta G^\circ = -RT \cdot \ln K_D \quad (\text{VI.1})$$

Notably, covalent immobilization of one peptide to a 3D hydrogel does not impair with the release of free assembly energy associated with coiled-coil formation (see Table VI.2).

K3Cys + E3Cys		<i>i</i> -K3Cys + <i>i</i> -E3Cys		K3Cys + <i>i</i> -E3Cys		<i>i</i> -K3Cys + E3Cys	
$K_D / \mu\text{M}$	$\Delta G^\circ / k_B T$	$K_D / \mu\text{M}$	$\Delta G^\circ / k_B T$	$K_D / \mu\text{M}$	$\Delta G^\circ / k_B T$	$K_D / \mu\text{M}$	$\Delta G^\circ / k_B T$
4.1 ± 0.7	-12.4	7.5 ± 0.6	-11.8	2.9 ± 0.8	-12.8	2.5 ± 0.6	-12.9
0.5 ± 0.3	-14.5	2.3 ± 1.8	-13.0	0.5 ± 0.3	-14.5	1.2 ± 1.0	-13.6
28 ± 1	-10.5	25 ± 3	-10.6	$31 \pm 1^*$	-10.4	28 ± 2	-10.5

TABLE VI.2 Dissociation constants K_D and corresponding free enthalpies ΔG° for coiled-coil formation determined by solution sensitive methods (CD spectroscopy; first row), within hydrogels (SPR spectroscopy; second row), and at the membrane interface (ellipsometry (Langmuir isotherm); last row). *) Ellipsometry data was fitted with Bragg-Williams isotherm.

We attribute this decrease in apparent affinity at the membrane interface to loss in translational entropy, which inevitably occurs due to a restriction in mobility of the surface bound peptides. We consider binding of peptides from solution to their corresponding lipopeptide counterparts embedded in a membrane as an adsorption process, in which at least one degree of translational freedom is lost. Generally, loss in entropy upon adsorption on a membrane surface is due to conversion of free translational and rotational degrees of freedom into bound motions, *i.e.* 'soft' vibrations of only a few $k_B T$.

Assuming that lipopeptides are immobilized on a planar 2D surface, we expect a frozen orientation of the peptides with less translational and probably also rotational degrees of freedom. Ben-Tal *et al.* (105) calculated that a loss of free energy of $\approx -1.5 k_B T$ for each translational degree of freedom due to adsorption is expected. In general, despite of the quantitative estimations from theory, we can safely assume that our reduction in binding enthalpies compared to association of peptides in solution arises from loss in entropy upon binding to membrane-based lipopeptides. This correction adds up to a maximum of free-energy loss of $\approx -4.5 k_B T$ for coiled-coil formation on a membrane surface, leading to essentially identical affinities at the membrane surface and in solution.

Finally it can be pointed out that otherwise coiled-coil formation on SSM is independent of the environment. Apart from that, the thermodynamics of peptide-association are also independent of helix orientation regardless whether parallel or antiparallel coiled-coil structures are formed. For inverted peptides with the opposite direction of the helical dipole moment, no substantial changes in binding strength could be found. All values are in the same regime, with slightly higher dissociation constants for antiparallel coiled-coil formation. Interestingly, it has been proposed that about $16 k_B T$ are required for hemifusion. As a consequence, a single dimer of this size used in this study is not sufficient to induce fusion mainly due the missing $3-4 k_B T$ of free energy spent to reduce entropy at the membrane interface. The necessary amount of free energy can therefore only be recruited by forming a larger number of coiled-coil complexes or by using longer helices with more heptad repeats.

VI.4 Fusogenicity of Parallel and Antiparallel Coiled-coil Complexes

Fusion efficiency comprising both lipid mixing and content mixing was explored as a function of peptide assembly. We were mainly interested whether parallel coiled-coil structures lead to higher fusion rates compared to antiparallel assemblies according to the zipper model that predicts a shorter distance between the two opposing lipid bilayers, if the peptides form a parallel coiled-coil bundle (see Fig. VI.1). Apart from the alignment, we also addressed the question whether reversal of the sequence changes fusion efficiencies. Since all peptide combinations show virtually identical binding constants, differences in fusogenic activity can be solely attributed to differences in molecular orientation.

Lipid mixing and content mixing were quantified by carrying out dequenching fluorescence assays (34, 87). For this purpose, two liposome populations are prepared, one population containing a fluorescent dye in self-quenching concentration, the other devoid of fluorophore. 10 mol% Texas Red in the membrane shell was used for lipid mixing, and 20 mM SRB (sulforhodamin B), a water-soluble dye enriched in the liposome lumen, for content mixing. The fluorescently labeled liposome populations were decorated with K-peptides, while the second, unlabeled vesicle population was functionalized with E-peptides. After mixing of the two vesicle populations, lipid mixing or content mixing, respectively, were detected by increasing fluorescence intensity due to dilution of the corresponding fluorescence dye (see Fig. VI.6).

100 % fusion refers to a one-to-one mixture of vesicles, *i.e.* one fluorescently labeled vesicle interacts with exactly one unlabeled liposome, which results in a calculable dilution of fluorophore concentration (see Chapter IV.7.1). Since the quenching mechanism for lipids covalently coupled to a fluorescent dye, like Texas Red depends on the membrane composition (106), we measured the concentration dependence of fluorescence for our lipid system using the Stern-Volmer equation. For SRB, a concentration dependent Stern-Volmer constant is published and was used to estimate a value for 100 % fusion which was employed for normalization (58).

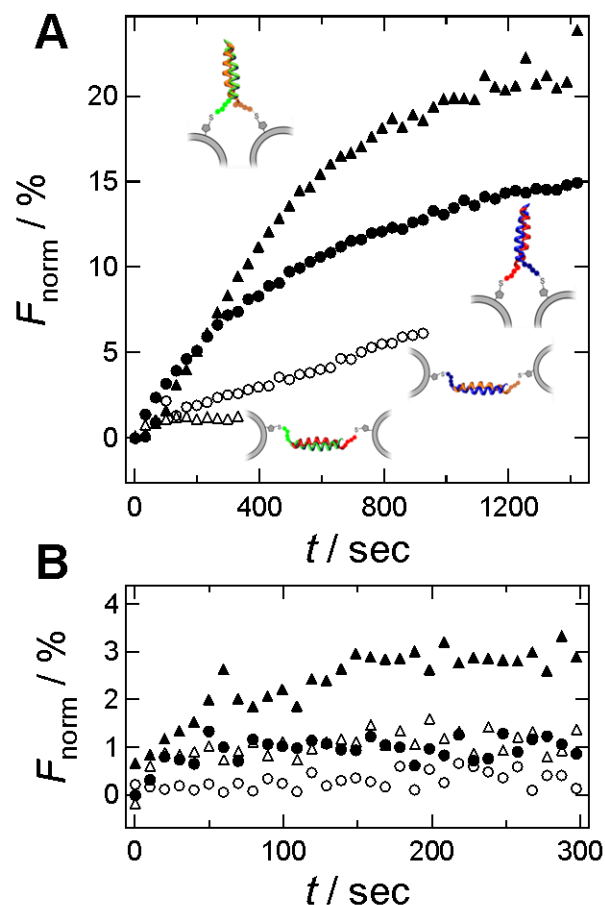


FIGURE VI.6 Lipid mixing and content mixing of SUVs decorated with E- and K-peptides. 100 % refers to 1:1 vesicle mixing. (A) Texas Red self-quenching assay for lipid mixing. Labeled SUVs were functionalized with K-peptides and mixed with unlabeled E-peptide bearing SUVs (start of mixing: $t = 0$). Parallel peptide packing facilitates lipid mixing (solid circles: K3Cys + E3Cys; solid triangles: *i*-K3Cys + *i*-E3Cys), in contrast to antiparallel coiled-coil formation (open circles: K3Cys + *i*-E3Cys, open triangles: *i*-K3Cys + E3Cys). (B) Content mixing monitored with a sulforhodamin B (SRB) self-quenching assay. K-peptide functionalized SUVs were filled with SRB (20 mM) and mixed with buffer filled SUVs displaying E-peptides. At time $t = 0$ Ca^{2+} ions were added ($c_{\text{final}} = 8$ mM). Markers are identical to those used in A.

From Figure VI.6 A it becomes evident that parallel coiled-coil formation leads to a substantial lipid mixing visible by the increasing fluorescence intensity of the Texas Red dye, while antiparallel dimerization shows slower or negligible lipid mixing of the two vesicle populations. This result also proves distinct peptide specificity for vesicle-vesicle interaction. The observed fusogenicity cannot be due to charge effects, since both K-peptides and both E-peptides carry the same charges. Therefore, we attribute the different docking and fusion efficiency of the four peptide pairs to purely structural effects. A higher fusogenicity of parallel coiled-coil pairs was expected, since in this case the two membranes are forced into close contact to each other, while in the antiparallel alignment the peptides rather create a spacer holding the two membranes apart. In content mixing experiments (see Fig. VI.6, B), only the parallel interaction

mediated by *i*-K3Cys and *i*-E3Cys shows a small but detectable increase in F_{norm} , while the antiparallel coiled-coil assembly is virtually indistinguishable from control measurements in the absence of fusion peptides. Furthermore, it is important to note that content mixing was only detectable after addition of Ca^{2+} ions, which was not needed for lipid mixing experiments. We attribute this to the bridging effect of Ca^{2+} binding to PC, PE, and non reacted MCCDOPE carrying a negative charge. Similar observations were made by Höök *et al.* also for otherwise zwitterionic lipids (31). However, full fusion is generally low compared to reconstituted SNAREs (107).

The only peptide assembly, which showed a positive result in both fluorescence fusion assays, was the coiled-coil consisting of *i*-K3Cys and *i*-E3Cys. This particular dimer showed the weakest binding in solution, but on a SSM its K_D was the lowest correlating with the strongest binding found. However, it is unlikely that this small difference in free energy explains the fusion activity of the peptides. We rather attribute the difference in content mixing to the dipole orientation affecting the peptide arrangement in the contact zone. Other important factors comprise higher order assemblies as observed for peptides on the membrane surface which will be highlighted in Chapter VII.

Notable is also the slow but consistent lipid mixing observable for the antiparallel coiled-coil consisting of K3Cys and *i*-E3Cys. This could be rationalized by the binding cooperativity found in ellipsometry studies for this particular dimer. Here, we also assume that this cooperativity mirrors lateral rearrangement of lipopeptides required to accommodate lipid mixing.

In summary, we found efficient lipid mixing for parallel coiled-coil heterodimerization as opposed to the corresponding antiparallel assembly. Content mixing, however, required addition of Ca^{2+} and was only observed for a single parallel combination of the coiled-coil dimers formed between the two opposing membranes. The sole mixing of both vesicle populations before addition of Ca^{2+} (see Fig. VI.6 B, $t = 0$) led to no increase in fluorescence intensity (data not shown).

VI.5 Discussion

The impact of peptide sequence on coiled-coil formation in solution and in the context of lipid bilayers was addressed with respect to docking thermodynamics and fusion efficiency. We found that neither antiparallel and parallel packing nor inversion of the helical dipole moment has a significant influence on the thermodynamics of coiled-coil dimerization. The dissociation constants of all peptide dimers were in the same regime. Free enthalpy changes

were significantly reduced if one peptide is coupled to a lipid bilayer in contrast to coiled-coil formation in solution. The difference of 3-4 $k_B T$ between coiled-coil formation in solution and at the membrane interface was largely attributed to a loss of translational degrees of freedom upon binding to the membrane. This implies a fixed orientation of lipopeptides resulting in reduced mobility which will be further scrutinized in Chapter VII.

The fusion assays reveal that a parallel coiled-coil formation is needed for a significant lipid mixing. We attribute this finding to the difference in proximity needed to overcome the hydration barrier. The zipper-like arrangement of the two peptides ensures a closer vicinity of the two opposing membranes and therefore hemifusion is facilitated. Simonsson *et al.* found a six times increased number of fusion events for a zipper-like orientation of two complementary DNA strands in contrast to DNA strands that form antiparallel double helices (31). In our case, full fusion of the two leaflets, however, was rarely observed and an appreciable efficiency only monitored for a single sequence.

A couple of reasons might explain this observation. First, the reduced lateral mobility prevents accumulation of coiled-coil dimers in the contact zone of the two vesicles, therefore limiting fusion efficiency. Second, so far we only employed lipids to anchor the recognition elements. Meyenberg *et al.* found that peptidic transmembrane anchors may boost fusion due to the finite stiffness of the helix and more severe perturbation of the membrane (34). This assumption is encouraged by the findings of Lygina *et al.* from the same group, who could show distinct fusion efficiency for parallel and antiparallel PNA (peptide nucleic acid) sequences coupled to transmembrane anchors (32).

VII Lateral Organization of Lipopeptides and the Impact on Heterodimerization¹⁸

In this chapter, the focus was laid on a potential self-assembled structuring of lipopeptides on lipid bilayers. Therefore, lateral mobility measurements of matrix lipids as well as hybrid lipopeptides and high resolution imaging of samples by the means of atomic force microscopy (Chapter VII.2) were carried out. Furthermore, impacts of peptide clustering on binding and unbinding forces were analyzed using membrane probe force spectroscopy (Chapter VII.3).

VII.1 Introduction

Hitherto, the model system established in this work was characterized in detail concerning its coiled-coil heterodimerization in solution and on membrane surfaces after lipopeptide formation via *in situ* maleimide chemistry (see Chapter V). Furthermore, it could be shown that a parallel coiled-coil formation of the peptides *i*-E3Cys and *i*-K3Cys shows decent fusogenicity concerning their lipid mixing ability, which makes it a suitable minimal model for SNARE mediated fusion (see Chapter VI.4). However, during those studies, some findings are not fully explainable yet. The heterodimerization on solid supported membranes showed a clear two-step kinetics encompassing a fast and a slow time constant, where the amount of peptide bound in the initial first time period characterized by $\tau_a < \tau_b$ strongly depends on the employed peptide sequences and the preparation protocol. With *i*-K-peptides coupled covalently to the surface, less than 50 % of the lipopeptides were accessible for coiled-coil formation in the first two minutes, implying that a slow reorganization process needed to occur before a full coverage could be achieved. Furthermore, upon SSM coupling, the coiled-coil formation of the employed model peptides correlated with a free energy release of only $10.5 k_B T$ which corresponds to a loss of $3-4 k_B T$ in comparison to solution experiments. We refer this to a loss of entropy due to potential peptide immobilization on the surface, which was not proven yet. Hence, lateral mobility studies employing fluorescence recovery after photobleaching (FRAP) and high resolution imaging of functionalized SSM by the means of atomic force microscopy (AFM) was applied to explore a possible structuring and self-assembled organization of lipopeptides.

¹⁸ Results of this chapter are published in

Gesa Pähler, Bärbel Lorenz and Andreas Janshoff "Impact of peptide clustering on unbinding forces in the context of fusion mimetics", *Biochemical and Biophysical Research Communications* **2013**, 430, 938-943.

Especially a potential lateral reorganization accompanying the process of coiled-coil heterodimerization, which might dissolve present lipopeptide clusters (see Fig. VII.1), called our attention and will be discussed here in detail.

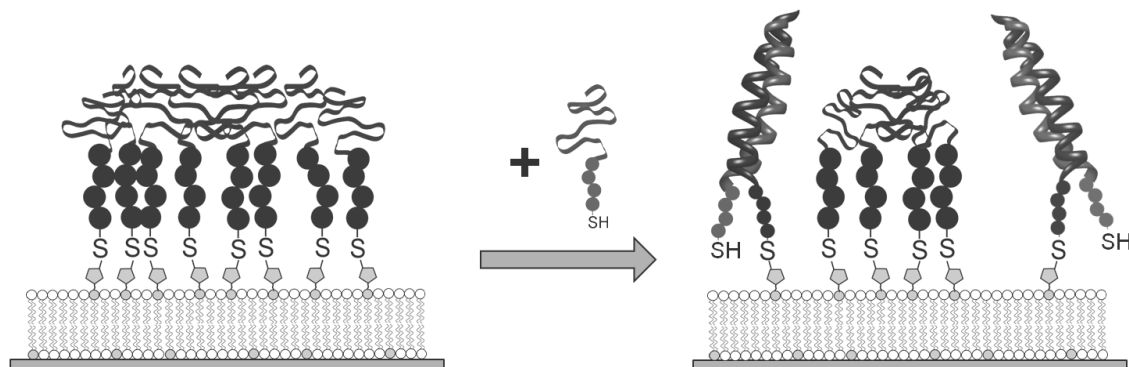


FIGURE VII.1 Schematic drawing of the envisioned lateral lipopeptide clustering on SSM, which partially dissolve upon coiled-coil heterodimerization.

To analyze the impact of lipopeptide organization or clustering on coiled-coil formation between two membranes, we performed force spectroscopy measurements similar to the setup introduced by Abdulreda *et al.* for SNARE proteins (108, 109). With this so called membrane probe force spectroscopy (MPS) setup, we studied the interaction between SSM doped with *i*-K3Cys and *i*-E3Cys constructs, respectively, in order to extract interaction force values of *i*-K3Cys/*i*-E3Cys heterodimers (see Chapter VII.3). By adjusting the peptide surface density in the applied setup and optimized dwell time, we were able to measure interaction forces for ensemble and single molecule events. At this juncture, a detailed view on processes occurring in the experiments could be achieved, concerning coiled-coil formation and subsequent cluster dissolution.

VII.2 Lateral Self-assembly of Lipopeptides in Solid Supported Membranes

In this part of the Chapter, the lipopeptide synthesis and subsequent coiled-coil formation on SSM are examined concerning their impact on lateral mobility of receptor lipids in the bilayer as well as the surrounding matrix lipids (see Chapter VII.2.1). Upon carrying out these experiments, more details pointed towards a self-assembled structuring of lipopeptides; this was analyzed employing high resolution imaging by means of AFM in Chapter VII.2.2.

VII.2.1 Lateral Mobility of Functionalized Membranes

In Chapter VI.3.2 an energy decrease of 3-4 $k_B T$ for the coiled-coil formation on solid supported membranes in comparison to solution experiments was found. This was explained by a loss of entropy, based on the assumption of a partial immobilization of peptide structures on SSM. To examine this working hypotheses, lateral mobility measurements were carried out by means of fluorescence recovery after photobleaching (FRAP). A SSM was labeled with 1 mol% of BODIPY, which afterwards is bleached by a sharp laser pulse at 488 nm to determine the recovery of the fluorescence intensity to the bleached region of interest (ROI) (see also Chapter IV.6). POPC, a fluid phase lipid, was employed as matrix lipid and the unfunctionalized lipid bilayer consisting of POPC/MCCDOPE/BODIPY 89:10:1 served as reference. The high amount of receptor lipid present in the analyzed SSM was chosen to achieve a high coverage of the surface with peptides; hence, the maximum impact of peptides on lateral mobility of lipids was achieved. With this method, SSM after lipopeptide formation via *in situ* coupling reactions as well as SSM presenting complete coiled-coil complexes were examined and their diffusion coefficient D and their mobile fraction F_{mob} were determined (see Fig. VII.2).

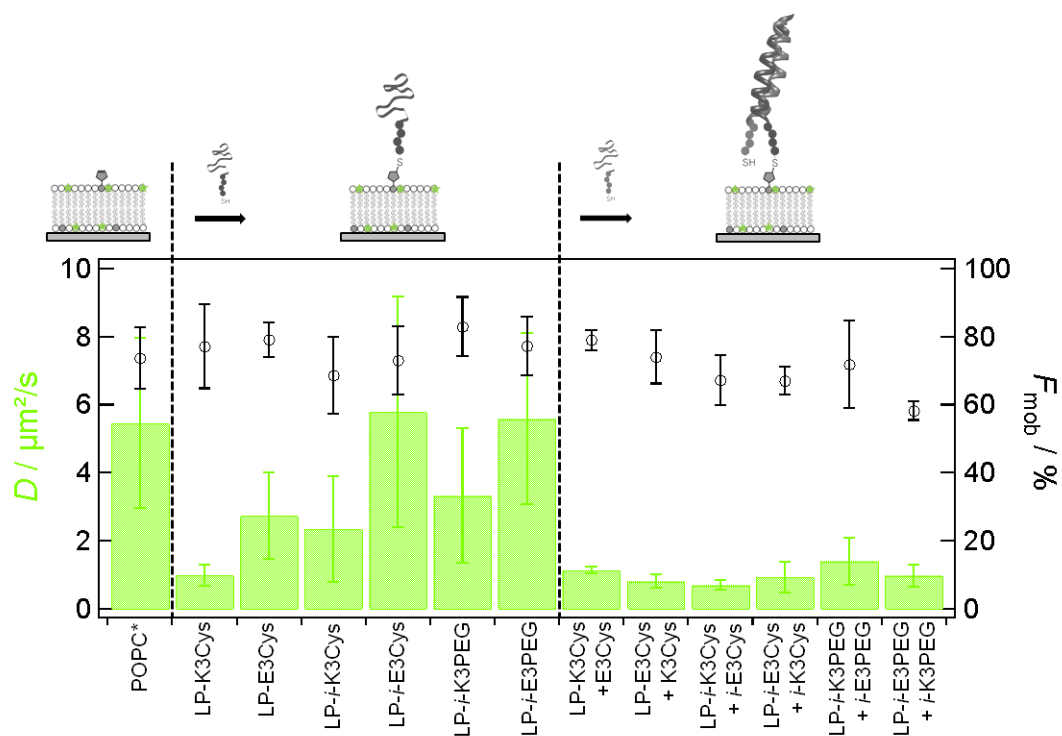


FIGURE VII.2 Results from fluorescence recovery after photobleaching (FRAP) experiments related to lateral mobility of lipid matrix. POPC/MCCDOPE/BODIPY 89:10:1 was spread on glass in PB 6.8 and functionalized with lipopeptides followed by successive coiled-coil formation to determine diffusion coefficient D (green bars) and mobile fraction F_{mob} (black circles). Plain SSM (POPC*) was used as reference which was compared to lipopeptide decorated SSM (LP-X) and SSM with complete coiled-coil structures (LP-X + Y).

The dissociation constant which was used as a reference value determined for a plain POPC membrane containing 10 mol% of receptor lipids and 1 mol% BODIPY is in good agreement to the literature (110) and it is shown that the mobile fraction of SSM on glass is already reduced to $\approx 80\%$ due to the adhesion to the solid support. From diffusion measurements of functionalized membranes, it is obvious that SSM with complete coiled-coil complexes exhibit a dramatic decrease of lateral mobility by half an order of magnitude in D from $5.5 \mu\text{m}^2/\text{s}$ to $\approx 1.0 \mu\text{m}^2/\text{s}$. For some SSM functionalized with only a single kind of lipopeptide, similar results can be found. Especially the *in situ* coupling reaction of K-lipopeptides leads to a decrease of the diffusion coefficient, while E-lipopeptides do not show such a pronounced behavior. Interestingly, the mobile fraction remains nearly constant, ranging between $\approx 60\text{--}80\%$, showing only small reduction of lateral mobility, which exhibits no correlation with the decreasing diffusion coefficient.

So far, in the described experiment, only the lateral mobility of surrounding matrix lipids was examined. Therefore, we extended the preparation protocol by removing BODIPY as fluorescent probe in SSM and labeled the complete coiled-coil structure by a subsequent coupling reaction to the remaining free cysteine of added peptide with and an Oregon Green 488 maleimide fluorophore (OG488). In this case, the peptides itself served as fluorescence FRAP probe, giving the possibility to determine their specific lateral mobility (see Fig. VII.3).

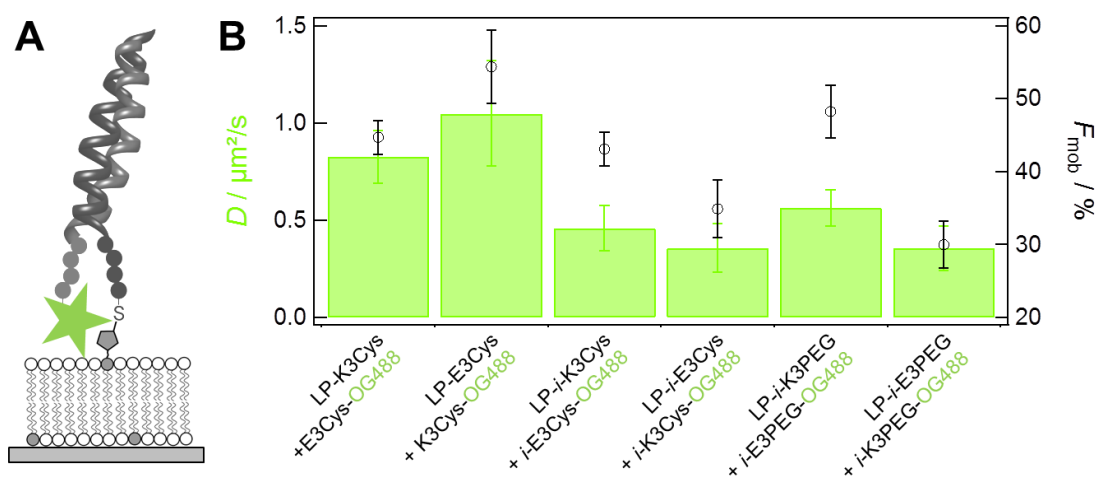


FIGURE VII.3 Results from fluorescence recovery after photobleaching (FRAP) experiments related to determine lateral mobility of coiled-coil complexes in lipid matrix. POPC/MCCDOPE 90:10 was spread on glass in PB 6.8 and functionalized with lipopeptides followed by successive coiled-coil formation. (A) Added peptides were afterwards labeled with Oregon Green 488 maleimide (OG488, green star). (B) Determined diffusion coefficients D (green bars) and mobile fractions F_{mob} (black circles) for tested LP-X + Y-OG488 combinations.

Here, an even lower diffusion coefficient D was determined for SSM presenting complete coiled-coil structures. While the mean diffusion for BODIPY labeled samples exhibiting a complete heterodimeric peptide structure was $1.0 \mu\text{m}^2/\text{s}$, it is further reduced to $0.6 \mu\text{m}^2/\text{s}$ for OG488 labeled coiled-coil complexes. Additionally, the mobile fraction shows here a clear correlation with the determined diffusion coefficients and is also reduced by $\approx 40\%$. All determined values are summarized in Table VII.1.

	$D^{\text{SSM}} / \mu\text{m}^2/\text{s}$	$F_{\text{mob}}^{\text{SSM}} / \%$	$D^{\text{cc}} / \mu\text{m}^2/\text{s}$	$F_{\text{mob}}^{\text{cc}} / \%$
POPC*	5.5 ± 2.5	74 ± 9	<i>n.a.</i>	<i>n.a.</i>
LP-K3Cys	1.0 ± 0.3	77 ± 12	<i>n.a.</i>	<i>n.a.</i>
LP-E3Cys	2.7 ± 1.3	79 ± 5	<i>n.a.</i>	<i>n.a.</i>
LP-<i>i</i>-K3Cys	2.4 ± 1.6	69 ± 11	<i>n.a.</i>	<i>n.a.</i>
LP-<i>i</i>-E3Cys	5.8 ± 3.4	73 ± 10	<i>n.a.</i>	<i>n.a.</i>
LP-<i>i</i>-K3PEG	3.3 ± 2.0	83 ± 9	<i>n.a.</i>	<i>n.a.</i>
LP-<i>i</i>-E3PEG	5.6 ± 2.5	77 ± 9	<i>n.a.</i>	<i>n.a.</i>
LP-K3Cys + E3Cys	1.1 ± 0.1	79 ± 3	0.8 ± 0.1	45 ± 2
LP-E3Cys + K3Cys	0.8 ± 0.2	74 ± 8	1.0 ± 0.3	54 ± 5
LP-<i>i</i>-K3Cys + <i>i</i>-E3Cys	0.7 ± 0.1	67 ± 7	0.5 ± 0.1	43 ± 2
LP-<i>i</i>-E3Cys + <i>i</i>-K3Cys	0.9 ± 0.5	67 ± 4	0.4 ± 0.1	35 ± 4
LP-<i>i</i>-K3PEG + <i>i</i>-E3PEG	1.4 ± 0.7	72 ± 13	0.6 ± 0.1	48 ± 4
LP-<i>i</i>-E3PEG + <i>i</i>-K3PEG	1.0 ± 0.3	58 ± 3	0.4 ± 0.1	30 ± 3

TABLE VII.1 Determined diffusion coefficients D and mobile fractions F_{mob} from FRAP experiments. Lateral mobility of matrix (index *SSM*, column 2-3) was specified by adding 1 mol% BODIPY to the SSM, mobility of coiled-coil complex (index *cc*, column 4-5) by labeling coiled-coil forming peptide with OG488. All experiments were carried out with 10 mol% MCCDOPE present in SSM.

The findings presented above prove that complete coiled-coil complexes are virtually immobile in SSM. Additionally, the study based on lateral mobility measurements of matrix lipids clearly indicates that already single lipopeptides, especially K-peptides, have a similar effect to the lipid bilayer. Hence, we can conclude that the hybrid structures formed of receptor lipids and one or two peptides, respectively, serve as obstacles to the surrounding matrix lipids, decreasing their lateral mobility but not the mobile fraction.

Additionally, in fluorescence micrographs taken during FRAP experiments, an inhomogeneity of fluorescence intensity was observed, which seemed to be correlated concerning the employed lipopeptides and complete coiled-coil structures, respectively (see Fig. VII.4).

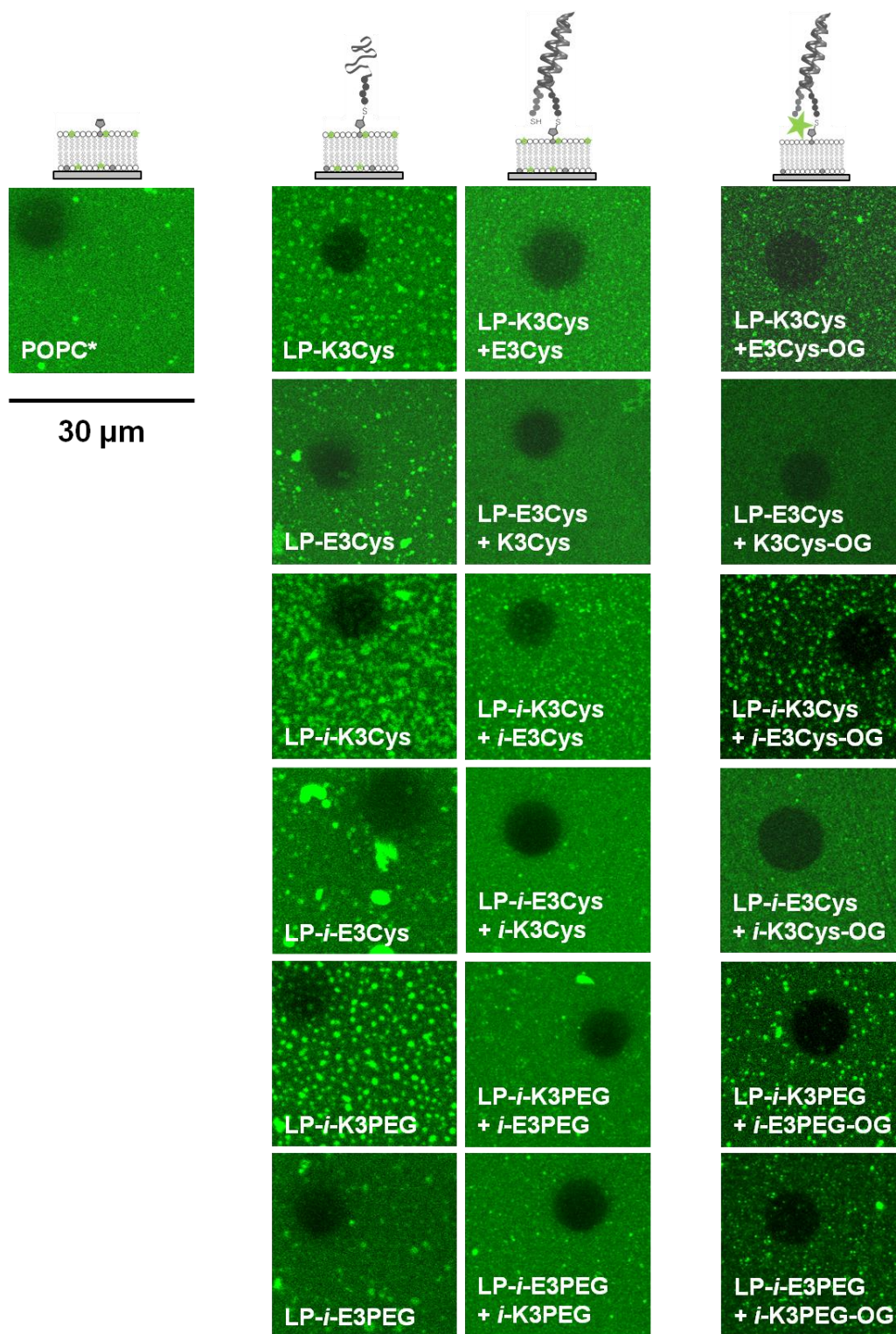


FIGURE VII.4 Typical FRAP fluorescence micrographs. Images were collected shortly after bleaching pulse. All pictures are $(30 \times 30) \mu\text{m}^2$. First column: plain SSM made of POPC/MCCDOPE/BODIPY 89:10:1 (*POPC**) Second column: POPC* functionalized with lipopeptides and with complete coiled-coil structures (third column). Fourth column: SSM made of POPC/MCCDOPE 90:10 functionalized with complete coiled-coil structures which were subsequently labeled *in situ* with OG488.

Compared to the plain membrane made of POPC/MCCDOPE/BODIPY 89:10:1 shown in first column, distinct structuring can be seen in some of the other samples. Especially for the peptide labeling preparation (fourth column), the K-lipopeptide based coiled-coil functionalized SSM exhibit a defined pattern. Hence, we can assume that a lateral clustering of peptides occurs on the surface and in dependence of the employed peptide sequences. Interestingly, also for the BODIPY labeled samples functionalized solely with K-lipopeptides, a similar structuring as in the fluorescence micrographs from OG488-labeled peptides can be found. Since in the pictures in second and third column, fluorescence of SSM is analyzed, we assume that lipopeptide formation induces a sorting of lipids correlating with local BODIPY concentration enrichment close to the formed hybrid structures. Furthermore, domains with higher fluorescence intensity seem to dissolve upon coiled-coil heterodimerization, since in the third column of Figure VII.4, a comparatively homogenous distribution of membrane fluorescence is detected. It is rather unlikely that the fluorescence active moiety interacts with the peptide, as BODIPY is an acyl chain labeled lipid, whereas the peptide moiety is attached to the headgroups of the embedded receptor lipids. However, it is conceivable that upon lipopeptide and coiled-coil formation, the acyl chain packing of MCCDOPE undergoes slight changes, due to the strongly affected headgroup geometries, resulting in more or less favored interactions with the present acyl chain labeled fluorophore.

In summary, these findings suggest that lipopeptide synthesis and successive coiled-coil formation lead to a lateral structuring of peptides on the membrane. The clusters additionally induce a sorting of lipids in the membrane which could be detected by an attraction of the lipid conjugated fluorophore BODIPY to the clusters. Furthermore, due to the diffusion coefficient measurements, we can conclude that coiled-coil modified receptor lipids are virtually immobile in a SSM. These relatively big peptide structures apparently act as obstacles, resulting in a strongly decreased lateral mobility of matrix lipids.

From the fluorescence micrographs, a cluster geometry can be assumed which seems to be related to the considered lipopeptide; however due to the limited lateral resolution achieved in fluorescence microscopy, no detailed quantification can be made. Therefore, AFM imaging was employed.

VII.2.2 Quantification of Peptide Clusters by High Resolution Imaging

Direct structural information of the membrane after *in situ* coupling reaction of peptides was obtained from AFM imaging of lipid bilayers spread on mica. Here, the gel phase lipid DPPC

instead of POPC was used as matrix lipid to slow down the lateral mobility. This enabled us to image even very small clusters. Furthermore, only 3 mol% of gel phase receptor lipid MCCDPPE was used to facilitate imaging of clusters and avoiding phase-separation from the DPPC matrix. A SSM made of DPPC/MCCDPPE 97:3 was spread on mica, imaged in PB 6.8 using tapping mode and exhibited the expected plain surface with a layer thickness of 4-5 nm (data not shown). After *in situ* coupling reaction with E-peptides, plaque shaped structures occurred on the SSM (see Fig. VII.5).

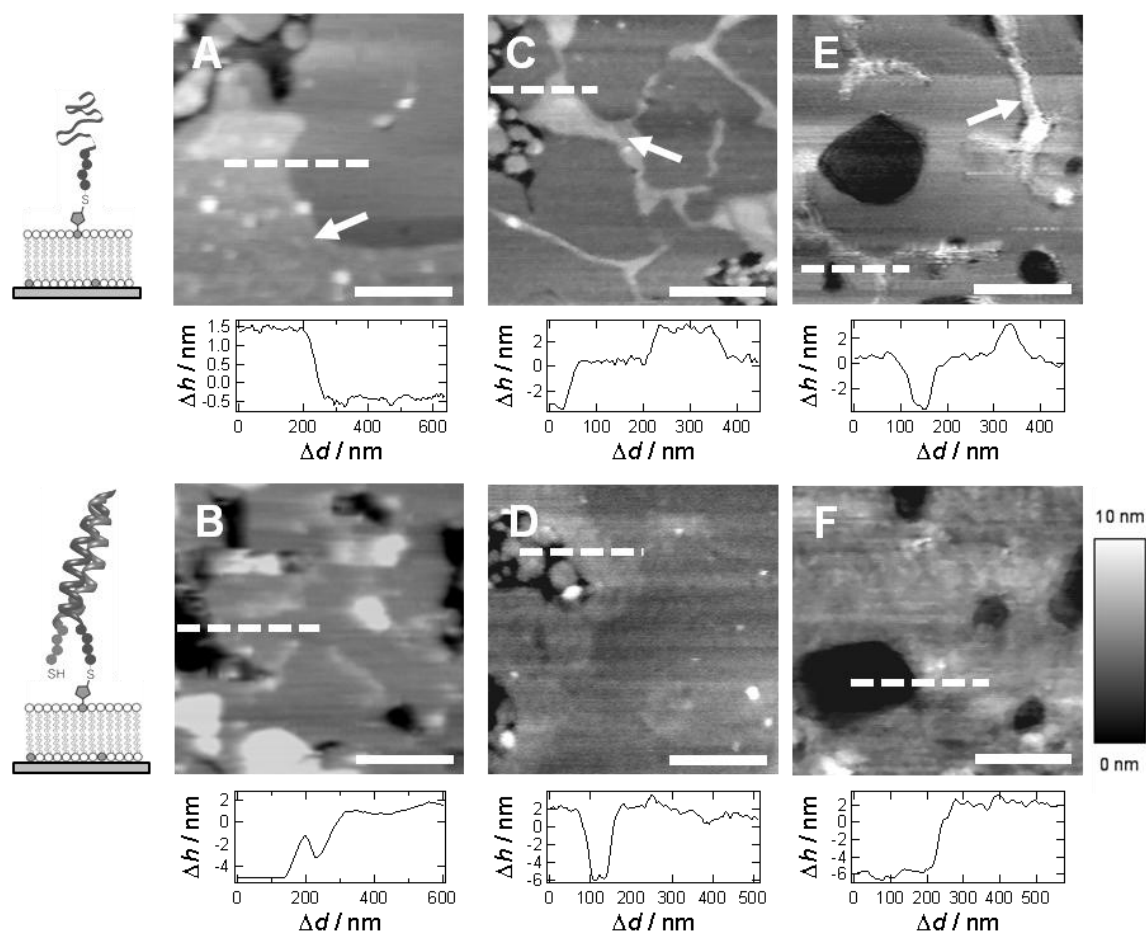


FIGURE VII.5 Topographical AFM images of E-lipopeptides embedded in DPPC/MCCDPPE 97:3 spread on mica (black in images) in PB 6.8. Clustering of lipopeptides is indicated with arrows (upper row); (second row) images were collected after corresponding coiled-coil forming peptides were added. Height profiles shown below the images were collected along scattered white lines. Scale bars: 400 nm, height of all images is set to 10 nm. (A) LP-E3Cys, (B) LP-E3Cys + K3Cys, (C) LP-*i*-E3Cys, (D) LP-*i*-E3Cys + *i*-K3Cys, (E) LP-*i*-E3PEG, (F) LP-*i*-E3PEG + *i*-K3PEG.

The height of this additional layer is determined to be ≈ 2 -3 nm and has a sheet-like nature for LP-E3Cys while for LP-*i*-E3Cys and LP-*i*-E3PEG the clusters exhibit a more stripe-shaped structure, whereas for the latter one less distinct borders are found. Strikingly, upon addition of the second coiled-coil forming peptide, the domains partially dissolve, but the overall determined layer

thickness increases to ≈ 8 nm. This implies that a full coverage of the SSM with coiled-coil heterodimers is achieved. However, the surface remains roughened, suggesting the presence of peptides on the membrane.

In contrast to the preparation protocol where E-peptides are covalently coupled to the receptor lipids, K-peptide functionalized lipid bilayers display smaller clusters (see Fig. VII.6).

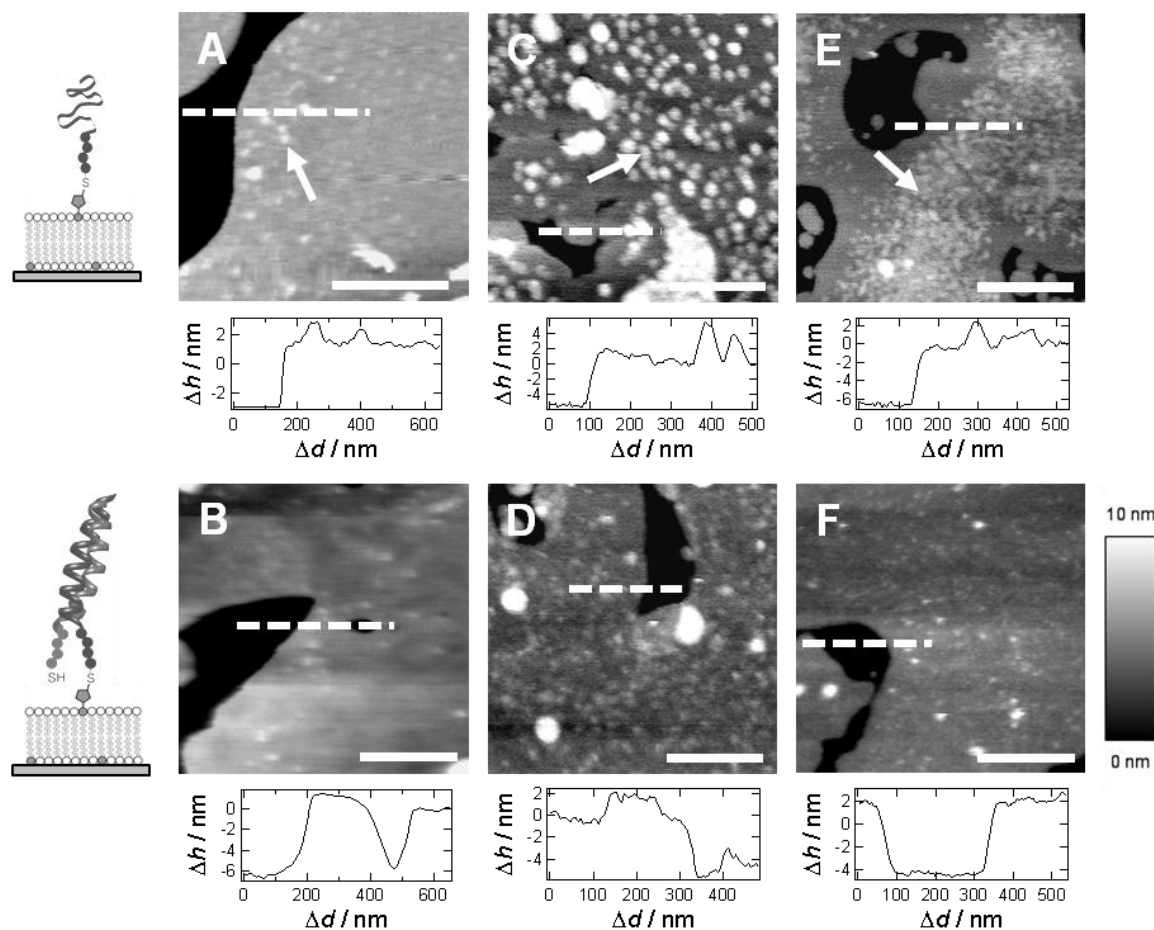


FIGURE VII.6 Topographical AFM images of K-lipopeptides embedded in DPPC/MCCDPPE 97:3 spread on mica (black in images) in PB 6.8. Clustering of lipopeptides is indicated with arrows (upper row); (second row) images were collected after corresponding coiled-coil forming peptides were added. Height profiles shown below the images were collected along scattered white lines. Scale bars: 400 nm, height of all images is set to 10 nm. (A) LP-K3Cys, (B) LP-K3Cys + E3Cys, (C) LP-*i*-K3Cys, (D) LP-*i*-K3Cys + *i*-E3Cys, (E) LP-*i*-K3PEG, (F) LP-*i*-K3PEG + *i*-E3PEG.

The layer thicknesses of peptide structures are again in a range of ≈ 2 -3 nm like for the E-peptide functionalized SSM shown before. LP-K3Cys exhibits only small clusters with a trend to lower heights, similar to LP-*i*-K3PEG. Here, a scattered structure consisting of clusters with a diameter of ≈ 10 -40 nm and a height of 1-2 nm is found. LP-*i*-K3Cys exhibits round and well defined shapes with a diameter ranging from 50-150 nm. Again, the samples were treated with coiled-coil forming peptides added in solution and imaged after an incubation time of several hours. Also

here, the overall layer thickness increased to up to 8 nm consistent with the height for a lipid bilayer decorated with peptides. In contrast to the samples with E-lipopeptide, residuals of clusters are still visible on the surface. Small scattered point-shaped structures are present on SSM containing LP-*i*-K3Cys/*i*-E3Cys and LP-*i*-K3PEG/*i*-E3PEG coiled-coil heterodimers, respectively, which are clearly reduced in their layer thickness and size. These findings are consistent with the negligible lateral diffusion present in gel phase bilayers and the additional immobilization due to peptide coupling. Even though, from the images, a partial dissolution of clusters can be assumed.

Comparing the results for K-lipopeptide decorated gel phase SSM presented above with images collected with fluid phase membranes, in this case POPC/MCCDOPE 97:3, similar findings concerning cluster formation and size are achieved (see Fig. VII.7).

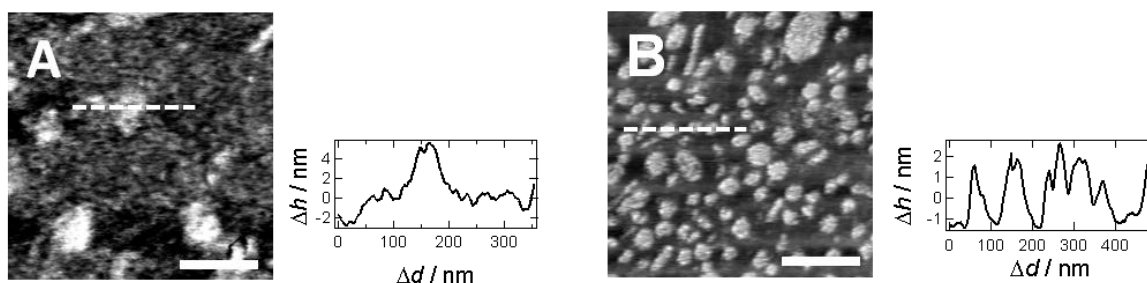


FIGURE VII.7 AFM images of K-lipopeptides attached to POPC/MCCDOPE 97:3 spread on mica (black in images) in PB 6.8. Height profiles (right next to the images) were collected along scattered white lines. Scale bars: 300 nm. (A) LP-K3Cys, (B) LP-*i*-K3Cys.

Cluster height was determined to be 2-3 nm over lipid bilayer surface as on gel phase SSM, but more difficult to capture, due to higher compressibility and fluidity of the membrane used here. LP-K3Cys exhibits a scattered and irregular structuring, whereas LP-*i*-K3Cys shows the well defined round shaped clusters which were already found for DPPC based membranes.

To examine the clusters in a more quantitative way, grain analysis of those images, which display clear structuring, was carried out. Hereby, a height threshold was introduced to determine size and geometry of the highest layer (see Fig. VII.8).

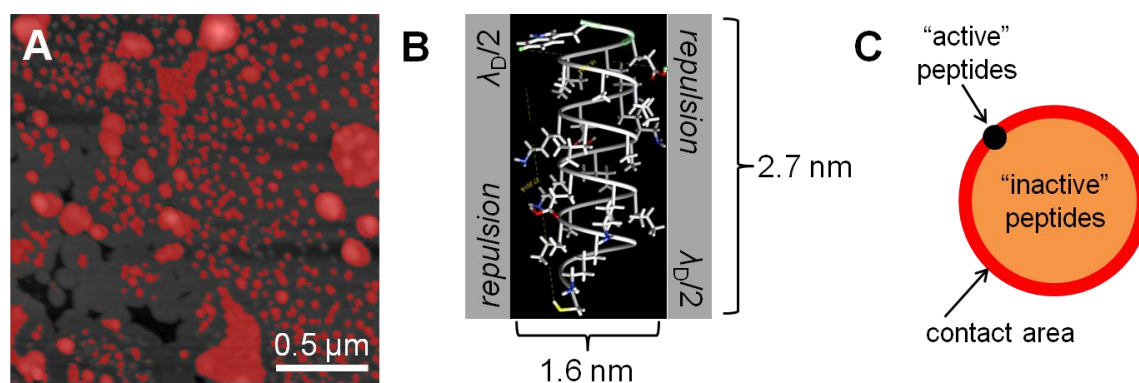


FIGURE VII.8 Schematic explanation of grain analysis. (A) AFM image of DPPC/MCCDPPE 97:3 functionalized with *i*-K3Cys on mica in PB 6.8. Grain analysis was carried out using a height threshold; grains are marked red in image. (B) Estimation of dimensional size of peptides. Size could be determined to be 2.7 nm in height and 1.6 nm in width. Grey blocks indicate a repulsion based on the debye length λ_D , between peptides. (C) Schematic drawing of cluster (orange-red). Peptides inside are considered inactive, peptides in contact area (black) are considered active.

From these calculations the overall fraction of peptide occupied area A is defined as mean grain area. All fractions of the bilayer covered with peptide are $\approx 30\%$ (see Table VII.2), which is in good agreement with the expectations for 3 mol% of MCC-phospholipids present in the SSM, since with 10 mol% of receptor lipids a full coverage of the surface with lipopeptides is achieved.

	LP-K3Cys	LP-E3Cys	LP- <i>i</i> -K3Cys	LP- <i>i</i> -E3Cys	LP- <i>i</i> -K3PEG	LP- <i>i</i> -E3PEG
$A_{\text{POPC}} / \%$	29 ± 1	-	30 ± 2	23 ± 7	-	-
$A_{\text{DPPC}} / \%$	22 ± 8	27 ± 4	32 ± 2	28 ± 8	39 ± 7	26 ± 9

TABLE VII.2 Fraction of area occupied by peptide clusters on SSM made of fluid phase lipids (A_{POPC}) and of gel phase lipids (A_{DPPC}); for POPC bilayers, only data for LP-K3Cys, LP-*i*-K3Cys and LP-*i*-E3Cys was collected.

From these results, the performance of employed grain analysis could be evaluated. It is obvious that for clusters exhibiting a relatively scattered patterning, the mean error for the defined occupied areas increases considerably: SSM functionalized with E-lipopeptides show errors in a range of 4-9%. Furthermore, the ratio for the very small structures made of LP-*i*-K3PEG also shows an error of 7%.

By means of grain analysis, the number of clusters per area as well as their mean equivalent disc radius r_{cluster} is determined (see Table VII.3). For the latter one, the structures are described by a circular shape, to define the lateral dimensional size of lipopeptide clusters. Since E-functionalized SSM show a diffuse and scattered arrangement, this approximation is not valid for those structures; hence no equivalent disc radius is determined here. Another source of error can be seen in Figure VII.8 A. Due to the merging of several clusters, the grain analysis software

identifies one big structure instead of the true number of clusters. Therefore, mean equivalent disc radii are systematically overestimated.

	$N_{\text{cluster}} / \mu\text{m}^{-1}$	$r_{\text{cluster}} / \text{nm}$	$N_{\text{active peptides}}$
LP-K3Cys (POPC)	535 ± 550	9 ± 5	39 %
LP- <i>i</i> -K3Cys (POPC)	145 ± 80	20 ± 8	18 %
LP-K3Cys (DPPC)	31 ± 31	22 ± 8	14 %
LP- <i>i</i> -K3Cys (DPPC)	295 ± 378	28 ± 8	14 %
LP- <i>i</i> -K3PEG (DPPC)	378 ± 499	11 ± 9	31 %

TABLE VII.3 Grain analysis for fluid and gel phase membranes. Assuming an area of 5 nm² for a single lipopeptide, ratio of active peptides in outer ring of cluster can be calculated ($N_{\text{active peptides}}$).

With the knowledge of overall cluster size, an estimation of number of peptides in the outer ring of clusters can be achieved. In the following those peptides will be so-called “active” peptides, whereas the molecules inside clustered structures will be referred to as “inactive” (see Fig. VII.8, C). The dimensional size of peptides were estimated employing the molecular modeling system UCSF Chimera (University of California, San Francisco, USA, funded by National Institute of Health) (111) and was found to be identical for all applied peptides in this work (see Fig. VII.8, B). The determined height of 2.7 nm is in very good agreement with the findings from our AFM measurements. Furthermore, with the determined diameter of 1.6 nm an area of occupation per peptide can be calculated. However, a repulsion between the peptides in clusters has to be assumed, which we calculated employing the specific Debye length λ_D (see eq. VII.1).

$$\lambda_D = \left(\sqrt{4\pi l_B \sum_{i=1}^n c_i z_i^2} \right)^{-1} \quad (\text{VII.1})$$

With the concentration c of present ions (with charge number z) in employed buffer PB 6.8 and assuming a Bjerrum-length l_B of ≈ 0.7 nm for water at room temperature (112), the Debye length is calculated to be 0.9 nm in our experiments. Hence, the diameter of one peptide inclusive a repulsive region increases to 2.5 nm, resulting in an area occupied per peptide of $A_{\text{peptide}} = 5 \text{ nm}^2$. Based on this lateral dimensional size of one lipopeptide, the number of peptides in the outer ring of clusters is calculated to define the ratio of “active” to “inactive” peptides (see last column, Table VII.3). As mentioned above, the results for LP-K3Cys are error-prone due to the scattered structure of formed clusters. However, this is not the case for the ratios defined for LP-*i*-K3Cys and LP-*i*-K3PEG. Strikingly, the amount of “active” peptides is strongly correlating with

the amount of coiled-coil formation taking place within the fast initial time step observed in time-resolved ellipsometry measurements (see Chapter V.3.2.1). Here, a two-step binding kinetic upon addition of coiled-coil forming peptides was found, resulting in just 18 % of *i*-E3Cys bound to LP-*i*-K3Cys in 1.6 min and 47 % of *i*-E3PEG to LP-*i*-K3PEG in 0.8 min, respectively, whereas other preparation protocols with E-peptides coupled covalently to the lipid bilayer showed up to 93 % binding in the first two minutes. These findings described above were made for fully covered lipid bilayers containing 10 mol% of receptor lipid MCCDOPE, which is not consistent with the 3 mol% of receptor lipid employed for the AFM imaging. However, in Figure VII.9 two-step binding kinetics for 3 mol% of MCCDOPE are presented, exhibiting a similar behavior then found for the fully covered lipid bilayers. Also here, initial binding in the fast time constant τ_1 shows less and slower heterodimerization if *i*-K3Cys is employed as lipopeptide in comparison to LP-*i*-E3Cys coupled covalently to the membrane.

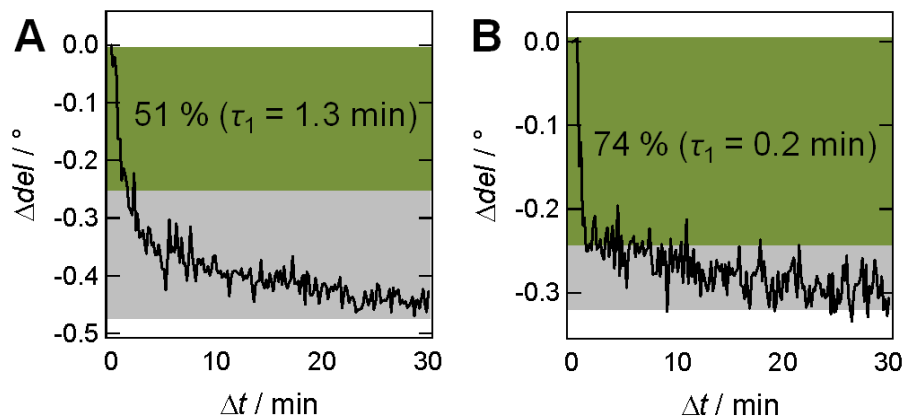


FIGURE VII.9 Coiled-coil formation on lipopeptide containing lipid bilayers monitored with time-resolved ellipsometry. All SSM were made of DOPC/MCCDOPE 97:3, experiments were carried out on silica in PB 6.8. Green marked area displays amount of fast initial binding within time constant τ_1 (peptides referred to as “active”), grey marked area displays subsequent binding until full coverage within slow time constant τ_2 (peptides referred to as “inactive”). (A) Addition of *i*-E3Cys to LP-*i*-K3Cys. (B) Addition of *i*-K3Cys to LP-*i*-E3Cys.

We envision that the clusters formed by lipopeptides receptors are slowly dispersed upon coiled-coil formation and a rather homogeneous layer of heterodimeric peptides replaces the clusters at the membrane interface. Therefore, we propose that the tendency towards clustering combined with the low lateral mobility of lipopeptides explains the observed two-step binding kinetics in ellipsometry, which could be described by a double exponential fit function. Now, we attribute the first, rather fast binding represented by τ_1 to binding of accessible lipopeptide receptor molecules - the “active” peptides in the outer ring of clusters - while remodeling of the lateral organization of membrane-based receptors gives rise to slower kinetics represented by

time constant τ_2 , since it requires additional time to liberate cluster-confined receptors. Desorption from coiled-coil complexes, however, follows a monoexponential decay with off-rates typically found for SNARE analogs (113, 114) supporting the idea that lateral clustering is abrogated by coiled-coil formation.

In summary, lipopeptides are laterally organized into clusters and act as obstacles slowing down the overall lateral mobility of the lipids in the bilayer. Especially, *i*-K3Cys exhibits clusters with well defined borders and regular size, which is reflected in the two-step binding kinetics found in ellipsometry measurements. To define a possible rearrangement of clusters on a shorter time-scale and to examine the impacts of lateral structuring on the energy landscape during binding and unbinding processes, the peptide pair *i*-K3Cys/*i*-E3Cys was analyzed employing force spectroscopy.

VII.3 Impact of Lipopeptide Clustering on Unbinding Forces¹⁹

Interaction forces between E-peptides and their corresponding K-peptides in the context of fluid lipid bilayers were assessed by means of membrane probe force spectroscopy (MPS). MPS permits to acquire force-distance curves between a membrane-coated bead ($\varnothing = 1\text{-}20\ \mu\text{m}$) and a solid supported membrane. Force distance curves are obtained as cycles comprising approach of the probe to the underlying SSM surface, and retraction of the probe from the contact zone. Adhesive forces are obtained from retraction curves due to formation of bonds in the contact area. To ensure a comparability of experiments, all measurements were carried out with a loading rate of $\approx 10\ \text{nN/s}$ (87, 115). Furthermore, if not otherwise stated, the interaction time of probe with the solid supported membrane underneath was kept constant at 1 s, and the approach and retraction was achieved with a velocity of $1\ \mu\text{m/s}$. In the presence of complementary peptides on the membrane surfaces (*i*-K3Cys on the membrane probe, *i*-E3Cys on the flat support) interaction forces are increased in contrast to control experiments with unfunctionalized, neat membranes (see Fig. VII.10). Forces of $\approx 250\ \text{pN}$ can be found for peptide-peptide interaction with 3 mol% of MCCDOPE present in the employed lipid bilayers, exhibiting a very broad distribution from $\approx 80\ \text{pN}$ to up to $\approx 600\ \text{pN}$ (see also Fig. VII.11, C). In comparison,

¹⁹ Experiments and analysis in this Chapter were carried out in cooperation with Bärbel Lorenz (PhD).

Main parts of this Chapter are published in

Gesa Pähler, Bärbel Lorenz and Andreas Janshoff "Impact on peptide clustering on unbinding forces in the context of fusion mimetics", *Biochemical and Biophysical Research Communications* **2013**, 430, 938-943.

neat membranes show most probable interaction forces of ≈ 20 pN which is just slightly above the experimental noise (115).

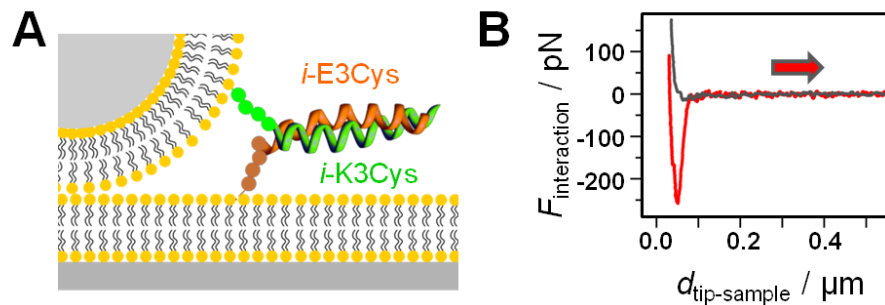


FIGURE VII.10 Coiled-coil interactions lead to increased membrane-membrane adhesion. (A) Schematic drawing of the experimental setup for the analysis of membrane interactions mediated by *i-K3Cys/i-E3Cys* coiled-coil formation. (B) Force-distance curves (retraction) as recorded for two neat POPC membranes (grey) and interactions between POPC membranes decorated with 3 mol% *i-K3Cys* and *i-E3Cys* peptides (red). Forces of ≈ 250 pN act on the membrane probe upon peptide interaction.

The results above are controversy to the results of Bornschlöggl *et al.* who determined the unfolding mechanics of coiled-coil structures following an un-zipping model. There, the unbinding forces are independent of analyzed superhelical length and in a range of ≈ 12 pN (116-118). Hence, interaction forces determined in our experiments must evolve from a large number of heterodimers formed between the membrane surfaces during contact. Considering the found forces ranging from ≈ 80 -1000 pN and the unbinding force determined by Bornschlöggl *et al.*, this would lead to 7-83 peptide bonds formed in the contact area. To understand this rather brought distribution which is related to the inhomogeneous arrangement of peptides on the membrane, the findings for the lateral organization of lipopeptides in clusters are considered. From AFM image analysis (grain size distribution) (Chapter VII.2.2) the number of clusters and therefore the number of peptides in contact area can be calculated.

Considering the calculated clusters per μm^2 (145 ± 80) and employing the Hertz model to determine the size of the contact zone (119), the lipid coated contact area between probe and silicon wafer can be calculated to a size of $0.011 \mu\text{m}^2$, corresponding to ≈ 1.6 *i-K3Cys* clusters in the contact area. Furthermore, it is conceivable that preferably peptide molecules in the outer cluster-shell undergo coiled-coil formation, due to steric hindrance and the determined low mobility of lipopeptides in the inner part of the cluster. In the previous chapter, it was calculated that only 18 % of lipopeptides in a POPC membrane doped with 3 mol% of LP-*i-K3Cys* are located in the outer cluster-shell and are therefore assumed to be able for heterodimerization.

To further investigate the impact of clustering on peptide interaction forces and to gain insights in how many bonds participate in cluster formation, we performed membrane probe spectroscopy measurements and varied the peptide surface in a range from 0.1 mol% to 10 mol%, resulting in interaction forces of ≈ 80 pN at the lowest surface concentration increasing to a value of ≈ 550 pN for 10 mol% lipopeptides (see Fig. VII.11, A).

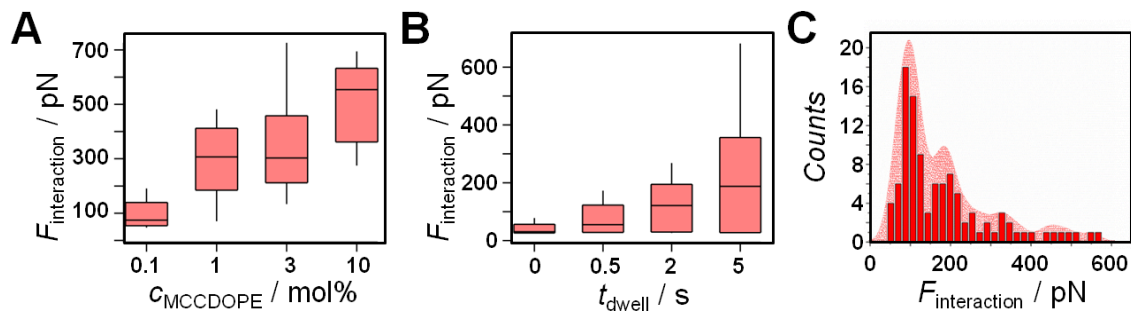


FIGURE VII.11 Variation of peptide concentration and interaction time for *i*-K3Cys/*i*-E3Cys-mediated membrane interaction forces. (A) Increased peptide surface concentration leads to enhanced interaction forces at a dwell time of 1 s. The median of membrane interaction force values varies between ≈ 80 pN at 0.1 mol% and ≈ 550 pN at 10 mol% lipopeptides in POPC membrane. (B) Increased membrane interaction time (dwell time t_{dwell}) leads to enhanced interaction forces (3 mol% MCCDOPE). The median of interaction forces ranges from ≈ 40 pN with no additional dwell time to ≈ 200 pN with $t_{\text{dwell}} = 5$ s. (C) Most probable interaction forces between *i*-K3Cys and *i*-E3Cys decorated membranes are ≈ 100 pN, ≈ 190 pN, ≈ 330 pN, and ≈ 480 pN (3 mol% MCCDOPE). Multiple force peaks can be interpreted in terms of the formation of several *i*-K3Cys/*i*-E3Cys interaction clusters. Kernel density estimation (bright red) shows maximum forces at 100 pN, 196 pN, 342 pN, 475 pN, and 560 pN.

Strikingly, this increase of interaction forces is non-linear, which indicates a progressive steric hindrance of peptides on the surface leading to constraints of peptide interactions. As availability of peptide helices for dimerization may be time-dependent with respect to peptide diffusion concerning *i*-E3Cys, we analyzed different membrane contact times for a given peptide surface concentrations. Hereby peptide interaction forces increase by a factor of five from a median of ≈ 40 pN at a dwell time $t_{\text{dwell}} = 0$ to a median of ≈ 200 pN at a contact time of 5 seconds (see Fig. VII.11, B). The maximum interaction force values for $t_{\text{dwell}} = 0$ are ≈ 50 pN, while they increase to up to ≈ 350 pN for increasing dwell and contact times. Since for E-lipopeptides the mobility of matrix lipids remains nearly unchanged, which is not the case for K-lipopeptides (see Chapter VII.2.1), we assume that E-lipopeptides are still mobile in the SSM and therefore can diffuse into the contact area to form additional coiled-coil heterodimers with K-lipopeptides.

Furthermore, we analyzed the interaction force distribution for 3 mol% of receptor lipids present in both membranes on probe and on underlying surface and found a multi-peak profile with a

most probable interaction force of around 100 pN (see Fig. VII.11, C). Further maxima can be found here at peak forces of ≈ 200 pN, ≈ 340 pN, ≈ 480 pN, and ≈ 560 pN. This distinct pattern of rupture forces suggests that each peak represents an additional cluster formed in the contact area. We identified five separate force peaks being indicative for a maximum number of five peptide clusters of differing interaction strength. When comparing these findings to the membrane probe contact area, it seems reasonable to claim that repositioning of the probe between individual measurements allows for different interaction scenarios involving varying numbers of peptide clusters (see Fig. VII.12).

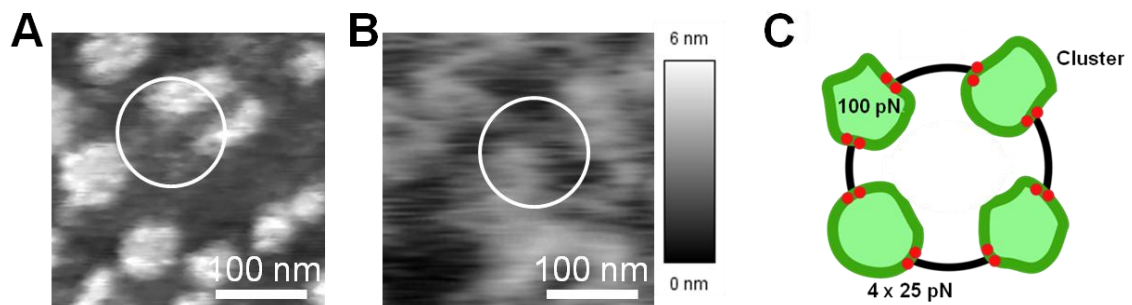


FIGURE VII.12 AFM images of POPC/MCCDOPE 97:3 decorated with *i*-K3Cys (A) and *i*-E3Cys (B). Both images were collected in PB 6.8 on mica substrates. Contact area estimated for MPS measurements is depicted as a white circle ($\varnothing \approx 120$ nm). (C) Membrane interaction scenario involving *i*-K3Cys/*i*-E3Cys peptides and spatial reduction of contact area. In combination with the contact zone defined by the probe geometry (indicated by black ring), coiled-coil formation (red dots) is only possible in intersection points of contact zone and clusters (green), with ≈ 100 pN force detection per cluster and between freely moving lipopeptides.

In the topographic image of K- and E-lipopeptides shown above, the contact area of MPS setup is depicted as a white circle. While LP-*i*-K3Cys displays clusters, LP-*i*-E3Cys shows scattered and diffuse structures which is not suitable to be analyzed with respect to cluster formation. From these images, it becomes evident, that for locally different force curves, varying interaction forces can be estimated. Assuming that each cluster is characterized by interaction strengths of ≈ 100 pN and that a single coiled-coil bond displays an interaction strength of ≈ 15 -50 pN, we arrive at 2-6 unbinding events per cluster. Actually, this is still considerably lower than the expected adhesive forces considering that 18 % of LP-*i*-K3Cys are still accessible, while the rest is bound and inactivated due to steric hindrance inside the clusters. However, assuming that interactions and hence coiled-coil formation is only possible in the intersections of the outer rings of K-clusters on the probe and the outer ring of the contact area (see Fig. VII.12, C), this leads to only two point-shaped intersections where heterodimerization could occur, decreasing the number of possible coiled-coil structures formed per cluster to 2-4. Additionally, it should be noted that the glass bead serving as probe displays a significant roughness, which has usually a

decreasing impact on the size of the contact area. However, in this specific case with cluster formation on the probe, the effect is not exactly assessable and has to be neglected here.

By reducing the peptide density on the membrane surface down to 0.1 mol%, we were able to extract unbinding events characterized by forces down to 25 pN and presenting a typical shape following the worm-like chain model which is indicative for the detection of unbinding of a single pair of coiled-coil peptides in a POPC bilayer (see Fig. VII.13).

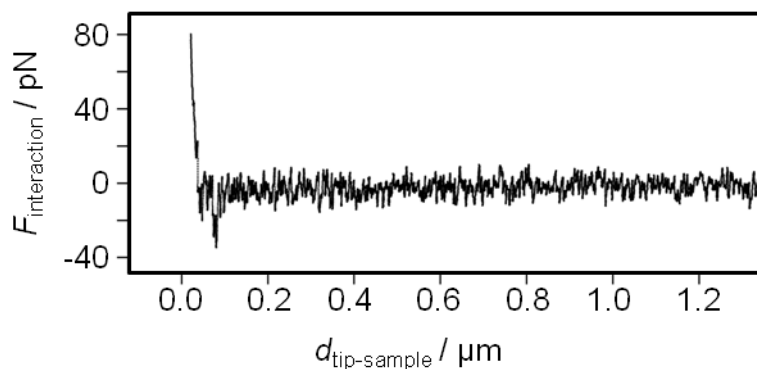


FIGURE VII.13 Force-distance curve (retraction) for interactions between POPC/MCCDOPE 99.9:0.1 membranes decorated with *i*-K3Cys and *i*-E3Cys peptides. Curve displays a single worm-like chain unbinding event at $F_{\text{interaction}} \approx 25$ pN.

This means in turn that the cluster being characterized by the main peak at 100 pN is composed of four *i*-K3Cys/*i*-E3Cys heterodimers, and that the maximum at 340 pN is generated by around 14 heterodimers. In accordance with the membrane topography depicted in the presented AFM images, we consider that peptide clusters of different sizes and of different availability for coiled-coil formation contribute to the overall membrane interaction force.

VII.4 Discussion

In this Chapter, we could prove the assumed lateral immobilization of lipopeptides and covalently coupled coiled-coil heterodimers on solid supported membranes due to distinct cluster formation. These findings explain reasonably well the results from Chapter VI, where a loss of free energy upon coiled-coil formation on lipid bilayers was found. This loss was explained by an immobilization of lipopeptides in the membrane, what could be shown here. Furthermore, the found clustering explains the similar binding affinities compared to a fully covered SSM (10 mol%) and an only partially covered membrane (3 mol%): steric hindrance, which affects the binding affinity, is - for the analyzed peptide sets - independent of the degree of coverage, since clustering and therefore steric hindrance in clusters occurs also on partially

covered membranes. Hence, the binding of peptides during coiled-coil formation depends strongly on the clustering, as it could be seen in the kinetic measurements following a two-step binding mechanism carried out by the means of ellipsometry.

Strikingly, the clustering and lateral mobility of hybrid lipopeptides is strongly dependent on the peptide type. E-lipopeptides exhibit a plaque- or stripe-shaped cluster formation, whereas K-lipopeptides display more point-like structures. Inversion of the peptide sequence has a great impact on clustering, considering the conversion from plaques to stripes for LP-E3Cys and LP-*i*-E3Cys, respectively. This effect is also observed for K-lipopeptides; here, LP-*i*-K3Cys exhibits a distinct point-like pattern, whereas LP-K3Cys display a more scattered clustering. Furthermore, PEGylation of the peptide sequences instead of using simple glycine spacers has also a considerable effect on the built clusters, resulting in smaller structures. Especially for the LP-*i*-K3PEG compared to LP-*i*-K3Cys, the mean radius decreases significantly from 28 nm to 11 nm for the PEGylated sequence, which can be correlated to a higher amount of “active” peptides in the outer ring of the clusters. Hence, we can conclude that not only the orientation of peptide sequence but also the spacer moiety has a clear impact on cluster formation. A possible explanation might be that *i*-K-peptides carry a positive charged amino acid (lysine) at their C-terminal recognition sequence, which is attached to the lipid bilayer, whereas K3Cys displays a negative charged glutamic acid residue at that position. Recently, it was shown that positive charged peptides can induce a lipid demixing if negative charged lipids are present (120). Since *i*-K3Cys carries a net charge of +3, the peptide might be interacting with remaining non-reacted receptor lipids (MCCDOPE) containing a negative charge, resulting in cluster formation. Furthermore, a bulky tryptophan group in the spacer sequence, present in all three E-peptides, might reduce a possible cluster density and hence result in more scattered patterning of lipopeptides in SSM.

Schuy *et al.* found clustering of HIV gp41 derived N36 lipopeptides that could be resolved by binding of T20 or the corresponding C34 peptide from solution (81) rendering clustering of lipopeptides a rather general phenomena. Furthermore, in 2001, syntaxin was found to be arranged in cholesterol dependent nanodomains, whose presence are crucial for fusion involving SNARE complex formation (14). In a later study employing high resolution fluorescence imaging (STED, stimulated emission depletion microscopy) in cells, the diameter of these domains could be defined to be 50-60 nm (121), which is very similar to the findings of our *i*-K3Cys clusters. However, in model systems it was shown that changes in cluster size can be generated by increasing the protein concentration by a factor of 100, leading to a strongly reduced docking

and thus fusion efficiency (122). Our minimal model system mimics these findings in a very sophisticated manner, providing exact peptide concentrations on the surface enabling the determination of ideal cluster size and peptide surface density to enhance fusion probability.

However, in the membrane probe spectroscopy experiments, the dramatic reduction of binding sites from expected several hundred events to a maximum of 14 coiled-coil heterodimers, is not exclusively explainable with clustering of LP-*i*-K3Cys. Since in the outer ring of clusters, 18 % of lipopeptides are available for heterodimerization, a decrease by a factor of five would be reasonable. However, the low forces can be explained assuming that interactions and hence coiled-coil formation is only possible in the intersections of the two outer rings defined by the borders of K-clusters and the rim of contact area defined by the probe. With on average 1.6 clusters in the contact area, the two main interaction forces found at ≈ 100 pN and ≈ 196 pN can be correlated with binding of one and two clusters, respectively. With the determined interaction force for one heterodimer (25 pN), which is good accordance to the results found by Bornschlöggl *et al.* (12 pN), this leads to 4-6 unbinding events per cluster. Hence, at one intersection point, 2-3 unbinding events can be estimated.

In conclusion, we can assume that lipopeptides organize into small lateral clusters with solid supported membranes that impair with the formation of coiled-coil dimers. This is in accordance with membrane probe force spectroscopy, AFM imaging, and kinetic data (see Chapter V.3.2). The latter one showed two consequential kinetic processes represented by a fast process (τ_1) and a slow one (τ_2). This two-step mechanism while heterodimerization can be correlated with grain analysis studies from AFM imaging, where the amount of peptides located in the outer ring of formed clusters corresponds well with the amount of coiled-coil formation during τ_1 . However, the slow time constant τ_2 probably corresponds to remodeling and dissolution of clusters so that the entire surface becomes occupied with coiled-coil peptides. Force cycles do not capture the two processes thus only report on quickly formed bonds, although the number of unbinding events could be increased by increasing the interaction times during dwell time studies. This is in good accordance with carried out lateral mobility studies, where E-lipopeptides still exhibited a distinct flexibility compared to virtually immobile K-lipopeptides. Therefore, laterally mobile E-lipopeptides diffuse into the contact area with increased interaction times during carried out force cycles, resulting in higher unbinding forces during retraction.

VIII Summary and Discussion

In this work, a minimal model system mimicking SNARE mediated membrane fusion was established and improved to compare not only energetic differences between the employed sets of coiled-coil heterodimers but also to determine structural characteristics like orientation and lateral self-assembly. Hereby, antiparallel and parallel coiled-coil complexes with varying spacer moieties were established and compared concerning their fusogenicity and thermodynamic behavior.

First, the well-known E- and K-sequences introduced by Litowski *et al.* in 2002 were employed to produce a short but specific heterodimeric peptide system, which could be altered by inverting the recognition sequence to form antiparallel coiled-coil complexes. Furthermore, a PEG-linker was embedded between the membrane surface and the recognition sequences instead of 3-4 glycine residues to analyze the impact of different spacer moieties. Membrane functionalization could be achieved via maleimide chemistry, providing a controlled amount of formed lipopeptides in lipid bilayers due to exact adjustment of the employed receptor lipid concentration.

Due to the primary sequence of employed peptides, with a β -branched amino acid in the hydrophobic layer defining a packing orientation, we assume that parallel and antiparallel heterodimerization takes place. After proving this successful and specific coiled-coil formation in solution and on membrane surfaces, we immersed into intricate thermodynamic analyzes to define dissociation constants of the employed peptides in 3D and 2D geometries. A distinct loss of free energy of $3-4 k_B T$ upon coiled-coil formation on solid supported membranes ($\Delta G^\circ \approx -11 k_B T$) compared to solution experiments ($\Delta G^\circ \approx -14 k_B T$) was determined for heterodimerization, which we were able to correlate with a loss of translational entropy due to immobilization of lipopeptides and coiled-coil functionalized receptor lipids in artificial membranes. Therefore, the formation of covalent hybrid peptide-lipid structures was analyzed concerning their specific lateral mobility as well as their impact on the surrounding matrix lipids. Hereby, a mean diffusion coefficient of only $0.6 \mu\text{m}^2/\text{s}$ for coiled-coil complexes was found, clearly correlating with a loss of mobility indicated by a lowered mobile fraction by $\approx 40\%$. Additionally, the lateral mobility of surrounding matrix lipids was determined to also decrease significantly upon functionalization. Especially, coiled-coil complexes lead to mean diffusion coefficient of only $1 \mu\text{m}^2/\text{s}$ for lipids, whereas the unfunctionalized SSM showed a five times higher diffusion constant. However, no impact on the overall mobility fraction of lipids was

found. By the means of this detailed lateral mobility studies, we were able to show that lipopeptides are virtually immobile in solid supported membranes and that they act as obstacles in lipid bilayers resulting in dramatically decreased diffusion rates.

Furthermore, this immobilization was correlated with peptide specific two-dimensional self-assembled local organization, leading to distinct cluster formation. Inside those dense collective lipopeptide structures, molecules are inactivated considering a potential heterodimerization. The peptide moieties occupying the outer ring at the border of clusters remain their activity and hence undergo a coiled-coil formation. Strikingly, although lipopeptides exhibit only marginal lateral mobility in lipid bilayers, the formed structures partially dissolve upon coiled-coil formation and hence undergo a slow but detectable rearrangement process mirrored also in a biphasic binding kinetics. The size and ordering of found clusters as well as the rate of immobilization of surrounding matrix lipids is highly dependent on the peptide type and the employed preparation pathway, *i.e.* a dependency concerning which peptide was coupled covalently and which was added to form coiled-coil complexes was found. In general, K-peptides exhibit a higher ordering character than E-peptides; the latter one are also considered as still mobile in membranes.

Employing fluorescence dequenching fusion assays, we tested the coiled-coil driven fusogenicity of parallel and antiparallel heterodimers. Hereby, the latter one showed no fusion activity, whereas the two parallel coiled-coil structures showed membrane mixing. The peptide pair made of i-K3Cys/i-E3Cys also showed full fusion in contrast to the peptide pair with the non-inverted recognition sequence consisting of K3Cys/E3Cys. Since this discrimination could not be attributed to thermodynamic characteristics of the employed four heterodimeric peptide sets, we explain these differences in fusogenicity with peptide specific characteristics concerning orientation during coiled-coil formation and self-assembled lateral organization. It is conceivable that antiparallel coiled-coil complexes hold the connected membranes apart abolishing lipid as well as lumen mixing. The differences concerning fusion activity of parallel coiled-coil molecules are attributed to the different degree of cluster formation. K3Cys/E3Cys showed scattered and inhomogeneous clustering correlating with sole lipid mixing, *i.e.* hemifusion, whereas the peptides exhibiting their inverted recognition sequence are full fusogenic and display homogeneous clusters with a narrow size distribution (compare with Fig. VII.7) correlating with distinct lateral reorganization of lipopeptides upon coiled-coil formation. This reorganization process leads to additional binding sites and hence stronger membrane interaction, which was

also mirrored in membrane probe spectroscopy mimicking the fusion geometry to extract interaction forces.

Finally, within this work it was shown that the formation of coiled-coil dimers consisting of E- and K-peptides displays already some of the intricacy peptides and proteins show at the interface of native membranes. Very important findings of this study are the considerably reduced binding affinity of coiled-coil forming peptides on solid supported membranes compared to solution experiments, which were successfully correlated to an immobilization of lipopeptides and their lateral clustering within the lipid bilayers. Especially the orientation and geometry dependent fusogenicity is novel, since only little comprehensive studies concerning this topic were carried out until now. With our results, we were able to show that the focusing on merely energetic aspects is insufficient to mimic membrane fusion based on coiled-coil driven recognition. Actually, the results presented here are indicative that lateral organization and protein-protein interactions due to self-assembly might be key processes in protein-mediated membrane fusion. Furthermore, in FRAP experiments a lipopeptide induced lipid sorting concerning the employed lipid labeled fluorophore BODIPY was found which resembles natural domain formation in plasma membranes. These native domains are supposed to provoke protein clustering and therefore might work as a key regulation step for membrane fusion. Nevertheless, the exact role of clustering needs to be elucidated in a more detailed manner. Furthermore, with the essential knowledge gained in this work, it calls for further specific studies with also native protein sequences like SNARE complexes beyond sole secondary and tertiary structure analytics to gain functional insights in protein-mediated membrane fusion considering the lateral protein organization.

References

1. Bruggeman, F. J., and H. V. Westerhoff. 2007. The nature of systems biology. *Trends Microbiol.* 15:45-50.
2. Zhang, Y., W. C. Ruder, and P. R. LeDuc. 2008. Artificial cells: building bioinspired systems using small-scale biology. *Trends Biotechnol.* 26:14-20.
3. Marsden, H. R., I. Tomatsu, and A. Kros. 2011. Model systems for membrane fusion. *Chem. Soc. Rev.* 40.
4. Berg, J. M., J. L. Tymoczko, and L. Stryer. 2003. *Biochemie*. Spektrum, Heidelberg.
5. Jahn, R., T. Lang, and T. C. Südhof. 2003. Membrane Fusion. *Cell* 112:519-533.
6. Chernomordik, L. V., and M. M. Kozlov. 2008. Mechanics of membrane fusion. *Nat. Struct. Mol. Biol.* 15:675-683.
7. Aefferer, S., T. Reusch, B. Weinhausen, and T. Salditt. 2009. Membrane fusion intermediates and the effect of cholesterol: An in-house X-ray scattering study. *Eur. Phys. J. E* 30:205-214.
8. Markin, V. S., M. M. Kozlov, and V. L. Borovjagin. 1984. On the Theory of Membrane Fusion. The Stalk Mechanism. *Gen. Physiol. Biophys.* 5:361-377.
9. Markin, V. S., and J. P. Albanesi. 2002. Membrane Fusion: Stalk Model Revisited. *Biophys. J.* 82:693-712.
10. Blumenthal, R., M. J. Clague, S. R. Durell, and R. M. Epand. 2003. Membrane Fusion. *Chem. Rev.* 103:53-70.
11. Basanez, G. 2002. Membrane fusion: the process and its energy suppliers. *Cell. Mol. Life Sci.* 59:1478-1490.
12. Singer, S. J., and G. L. Nicolson. 1975. The Fluid Mosaic Model of the Structure of Cell Membranes. *Science* 175:720-731.
13. Pike, L. J. 2009. The challenge of lipid rafts. *J. Lipid Res.* 50:S323-S328.
14. Lang, T., D. Bruns, D. Wenzel, D. Riedel, P. Holroyd, C. Thiele, and R. Jahn. 2001. SNAREs are concentrated in cholesterol-dependent clusters that define docking and fusion sites for exocytosis. *EMBO J.* 20:2202-2213.
15. Marsden, H. R., and A. Kros. 2010. Self-Assembly of Coiled Coils in Synthetic Biology: Inspiration and Progress. *Angew. Chem. Int. Ed.* 49:2988-3005.
16. Steinmetz, M. O., I. Jelesarov, W. M. Matousek, S. Honnappa, W. Jahnke, J. H. Missimer, S. Frank, A. T. Alexandrescu, and R. A. Kammerer. 2007. Molecular basis of coiled-coil formation. *Proc. Nat. Acad. Sci. USA* 104:7062-7067.
17. Chan, D. C., and P. S. Kim. 1998. HIV Entry and Its Inhibition. *Cell* 93:681-684.
18. Chen, J., J. J. Skehel, and D. C. Wiley. 1999. N- and C-terminal residues combine in the fusion-pH influenza hemagglutinin HA2 subunit to form an N cap that terminates the triple-stranded coiled coil. *Proc. Nat. Acad. Sci. USA* 96:8967-8972.
19. Bullough, P. A., F. M. Hughson, J. J. Skehel, and D. C. Wiley. 1994. Structure of influenza haemagglutinin at the pH of membrane fusion. *Nature* 371:37-43.
20. Südhof, T. C., and J. E. Rothman. 2009. Membrane Fusion: Grappling with SNARE and SM Proteins. *Science* 323:474-477.
21. Fernandez, I., J. Ubach, I. Dulubova, X. Zhang, T. C. Südhof, and J. Rizo. 1998. Three-Dimensional Structure of an Evolutionarily Conserved N-Terminal Domain of Syntaxin 1A. *Cell* 94:841-849.
22. Sutton, R. B., D. Fasshauer, R. Jahn, and A. T. Brunger. 1998. Crystal structure of a SNARE complex involved in synaptic exocytosis at 2.4Å resolution. *Nature* 395:347-353.
23. Jahn, R., and R. H. Scheller. 2006. SNAREs - engines for membrane fusion. *Nat. Rev. Mol. Cell Biol.* 7:631-643.

24. Brunger, A. T., K. Weninger, M. Bowen, and S. Chu. 2009. Single-Molecule Studies of the Neuronal SNARE Fusion Machinery. *Annu. Rev. Biochem.* 78:903-928.
25. Stein, A., G. Weber, M. C. Wahl, and R. Jahn. 2009. Helical extension of the neuronal SNARE complex into the membrane. *Nature* 460:525-528.
26. Woodbury, D. J., and K. Rognlien. 2000. The t-SNARE syntaxin is sufficient for spontaneous fusion of synaptic vesicles to planar membranes. *Cell Biol. Int.* 24:809-818.
27. Li, F., F. Pincet, E. Perez, W. S. Eng, T. J. Melia, J. E. Rothman, and D. Tareste. 2007. Energetics and dynamics of SNAREpin folding across lipid bilayers. *Nat. Struct. Mol. Biol.* 14:890-896.
28. van den Bogaart, G., M. G. Holt, G. Bunt, D. Riedel, F. S. Wouters, and R. Jahn. 2010. One SNARE complex is sufficient for membrane fusion. *Nat. Struct. Mol. Biol.* 17:358-364.
29. Stengel, G., R. Zahn, and F. Höök. 2007. DNA-Induced Programmable Fusion of Phospholipid Vesicles. *J. Am. Chem. Soc.* 129:9584-9585.
30. Stengel, G., L. Simonsson, R. A. Campbell, and F. Höök. 2008. Determinants for Membrane Fusion Induced by Cholesterol-Modified DNA Zippers. *J. Phys. Chem. B* 112:8264-8274.
31. Simonsson, L., P. Jönsson, G. Stengel, and F. Höök. 2010. Site-Specific DNA-controlled Fusion of Single Lipid Vesicles to Supported Lipid Bilayers. *ChemPhysChem* 11:1011-1017.
32. Lygina, A. S., K. Meyenberg, R. Jahn, and U. Diederichsen. 2011. Transmembrane Domain Peptide/Peptide Nucleic Acid Hybrid as a Model of a SNARE Protein in Vesicle Fusion. *Angew. Chem. Int. Ed.* 50:8597-8601.
33. Marsden, H. R., N. A. Elbers, P. H. H. Bomans, N. A. J. M. Sommerdijk, and A. Kros. 2009. A Reduced SNARE Model for Membrane Fusion. *Angew. Chem. Int. Ed.* 48:2330-2333.
34. Meyenberg, K., A. S. Lygina, G. van den Bogaart, R. Jahn, and U. Diederichsen. 2011. SNARE derived peptide mimic inducing membrane fusion. *Chem. Comm.* 47:9405-9407.
35. McNew, J. A., T. Weber, F. Parlati, R. J. Johnston, T. J. Melia, T. H. Söllner, and J. E. Rothman. 2000. Close Is Not Enough: SNARE-dependent Membrane Fusion Requires an Active Mechanism that Transduces Force to Membrane Anchors. *J. Cell Biol.* 150:105-118.
36. Chernomordik, L. V., J. Zimmerberg, and M. M. Kozlov. 2006. Membranes of the world unite! *J. Cell Biol.* 175:201-207.
37. Tamm, L. K., J. Crane, and V. Kiessling. 2003. Membrane fusion: a structural perspective on the interplay of lipids and proteins. *Curr. Opin. Struct. Biol.* 13:453-466.
38. Castellana, E. T., and P. S. Cremer. 2006. Solid supported lipid bilayers: From biophysical studies to sensor design. *Surf. Sci. Rep.* 61:429-444.
39. Milhiet, P. E., M.-C. Giocondi, and C. Le Grimellec. 2003. AFM imaging of Lipid Domains in Model Membranes. *ScientificWorldJournal* 3:59-74.
40. Schuy, S., B. Treutlein, A. Pietuch, and A. Janshoff. 2008. In situ Synthesis of Lipopeptides as Versatile Receptors for the Specific Binding of Nanoparticles and Liposomes to Solid-Supported Membranes. *Small* 4:970-981.
41. Rietveld, A., and K. Simons. 1998. The differential miscibility of lipids as the basis for the formation of functional membrane rafts. *Biochim. Biophys. Acta* 1376:467-479.
42. McMullen, T. P. W., and R. N. McElhaney. 1995. New aspects of the interaction of cholesterol with dipalmitoylphosphatidylcholine bilayers as revealed by high-sensitivity differential scanning calorimetry. *Biochim. Biophys. Acta* 1234:90-98.
43. Castorph, S., S. Schwarz Henriques, M. Holt, D. Riedel, R. Jahn, and T. Salditt. 2011. Synaptic vesicles studied by dynamic light scattering. *Eur. Phys. J. E* 34:1-11.
44. Lapinski, M. M., A. Castro-Forero, A. J. Greiner, R. Y. Ofoli, and G. J. Blanchard. 2007. Comparison of Liposomes Formed by Sonication and Extrusion: Rotational and Translational Diffusion of an Embedded Chromophore. *Langmuir* 23:11677-11683.

45. Reimhult, E., F. Höök, and B. Kasemo. 2002. Intact Vesicle Adsorption and Supported Biomembrane Formation from Vesicles in Solution: Influence of Surface Chemistry, Vesicle Size, Temperature, and Osmotic Pressure. *Langmuir* 19:1681-1691.
46. Mason, J. M., and K. M. Arndt. 2004. Coiled Coil Domains: Stability, Specificity, and Biological Implications. *ChemBioChem* 5:170-176.
47. Hol, W. G. J., P. T. van Duijnen, and H. J. C. Berendsen. 1978. The alpha-helix dipole and the properties of proteins. *Nature* 273:443-446.
48. Litowski, J. R., and R. S. Hodges. 2002. Designing Heterodimeric Two-stranded alpha-Helical Coiled-coils. *J. Biol. Chem.* 277:37272-37279.
49. Zhu, B.-Y., M. E. Zhou, C. M. Kay, and R. S. Hodges. 1993. Packing and hydrophobicity effects on protein folding and stability: Effects of β -branched amino acids, valine and isoleucine, on the formation and stability of two-stranded α -helical coiled coils/leucine zippers. *Protein Sci.* 2:383-394.
50. Eilers, M., A. B. Patel, W. Liu, and S. O. Smith. 2002. Comparison of Helix Interactions in Membrane and Soluble alpha-Bundle Proteins. *Biophys. J.* 82:2720-2736.
51. Merrifield, R. B. 1963. Solid Phase Peptide Synthesis. I. The Synthesis of a Tetrapeptide. *Journal of the American Chemical Society* 85:2149-2154.
52. Carpino, L. A., and G. Y. Han. 1970. 9-Fluorenylmethoxycarbonyl function, a new base-sensitive amino-protecting group. *J. Am. Chem. Soc.* 92:5748-5749.
53. Coin, I., M. Beyermann, and M. Bienert. 2007. Solid-phase peptide synthesis: from standard procedures to the synthesis of difficult sequences. *Nat. Protocols* 2:3247-3256.
54. Carpino, L. A., H. Imazumi, A. El-Faham, F. J. Ferrer, C. Zhang, Y. Lee, B. M. Foxman, P. Henklein, C. Hanay, C. Mügge, H. Wenschuh, J. Klose, M. Beyermann, and M. Bienert. 2002. Kupplungsreagentien vom Uronium-/Guanidinium-Typ: Synthese und Charakterisierung der authentischen Uroniumsalze. *Angew. Chem.* 114:457-461.
55. Kaiser, E., R. L. Colescott, C. D. Bossinger, and P. I. Cook. 1970. Color test for detection of free terminal amino groups in the solid-phase synthesis of peptides. *Anal. Biochem.* 34:595-598.
56. Choikhet, K., B. Glatz, and G. Rozing. 2003. The Physicochemical Causes of Baseline Disturbances in HPLC, Part I - TFA-Containing Eluents. *LC GC Eur.*:2-9.
57. Andrushchenko, V. V., H. J. Vogel, and E. J. Prenner. 2007. Optimization of the hydrochloric acid concentration used for trifluoroacetate removal from synthetic peptides. *J. Pept. Sci.* 13:37-43.
58. Plant, A. L. 1986. Mechanism of concentration quenching of a xanthene dye encapsulated in phospholipid vesicles. *Photochem. Photobiol.* 44:453-459.
59. Günzler, H., and H. M. Heise. 1996. IR-Spektroskopie. VCH, Weinheim.
60. Winter, R., F. Noll, and C. Czeslik. 2011. *Methoden der Biophysikalischen Chemie.* Teubner, Wiesbaden.
61. Tamm, L. K., and S. A. Tatulian. 1997. Infrared spectroscopy of proteins and peptides in lipid bilayers. *Q. Rev. Biophys.* 30:365-429.
62. Goormaghtigh, E., V. Raussens, and J.-M. Ruyschaert. 1999. Attenuated total reflection infrared spectroscopy of proteins and lipids in biological membranes. *Biochim. Biophys. Acta* 1422:105-185.
63. Fringeli, U. P., and H. H. Gunthard. 1981. Infrared membrane spectroscopy. *Mol. Biol. Biochem. Biophys.* 31:270-332.
64. Barth, A., and C. Zscherp. 2002. What vibrations tell about proteins. *Q. Rev. Biophys.* 35:369-430.
65. Reisdorf, W. C., and S. Krimm. 1996. Infrared Amide I Band of the Coiled Coil. *Biochemistry* 35:1383-1386.

66. Heimburg, T., J. Schuenemann, K. Weber, and N. Geisler. 1996. Specific Recognition of Coiled Coils by Infrared Spectroscopy: Analysis of the Three Structural Domains of Type III Intermediate Filament Proteins. *Biochemistry* 35:1375-1382.
67. Heimburg, T., J. Schünemann, K. Weber, and N. Geisler. 1999. FTIR-Spectroscopy of Multistranded Coiled Coil Proteins. *Biochemistry* 38:12727-12734.
68. Kelly, S. M., and N. C. Price. 2000. The Use of Circular Dichroism in the Investigation of Protein Structure and Function. *Curr. Protein Pept. Sci.* 1:349-384.
69. Kelly, S. M., T. J. Jess, and N. C. Price. 2005. How to study proteins by circular dichroism. *Biochim. Biophys. Acta* 1751:119-139.
70. Johnson, W. C. 1988. Secondary Structure of Proteins Through Circular Dichroism Spectroscopy. *Annu. Rev. Biophys. Biophys. Chem.* 17:145-166.
71. Pace, C. N., V. Felix, F. Lanette, G. Gerald, and G. Theronica. 1995. How to measure and predict the molar absorption coefficient of a protein. *Protein Sci.* 4:2411-2423.
72. Whitmore, L., and B. A. Wallace. 2004. DICHROWEB, an online server for protein secondary structure analyses from circular dichroism spectroscopic data. *Nucleic Acids Res.* 32:W668-W673.
73. Whitmore, L., and B. A. Wallace. 2008. Protein Secondary Structure Analyses from Circular Dichroism Spectroscopy: Methods and Reference Databases. *Biopolymers* 89:392-400.
74. Andrade, M. A., P. Chacón, J. J. Merelo, and F. Morán. 1993. Evaluation of secondary structure of proteins from UV circular dichroism spectra using an unsupervised learning neural network. *Protein Eng.* 6:383-390.
75. Chao, H., M. E. J. Houston, S. Grothe, C. M. Kay, M. O'Connor-McCourt, R. T. Irvin, and R. S. Hodges. 1996. Kinetic Study on the Formation of a de Novo Designed Heterodimeric Coiled-Coil: Use of Surface Plasmon Resonance to Monitor the Association and Dissociation of Polypeptide Chains. *Biochemistry* 35:12175-12185.
76. Homola, J., S. S. Yee, and G. Gauglitz. 1999. Surface plasmon resonance sensors: review. *Sens. Actuators, B* 54:3-15.
77. Day, Y. S. N., C. L. Baird, R. L. Rich, and D. G. Myszka. 2002. Direct comparison of binding equilibrium, thermodynamic, and rate constants determined by surface- and solution-based biophysical methods. *Protein Sci.* 11:1017-1025.
78. Karlsson, R., H. Roos, L. Fägerstam, and B. Persson. 1994. Kinetic and Concentration Analysis Using BIA Technology. *Methods* 6:99-110.
79. Rothen, A. 1945. The Ellipsometer, an Apparatus to Measure Thicknesses of Thin Surface Films. *Rev. Sci. Instrum.* 16:26-30.
80. Faiss, S., S. Schuy, D. Weiskopf, C. Steinem, and A. Janshoff. 2007. Phase Transition of Individually Addressable Microstructured Membranes Visualized by Imaging Ellipsometry. *J. Phys. Chem. B* 111:13979-13986.
81. Schuy, S., E. Schäfer, N. C. Yoder, K. Kumar, R. Vogel, and A. Janshoff. 2009. Lipopeptides derived from HIV and SIV mimicking the prehairpin intermediate of gp41 on solid supported lipid bilayers. *J. Struct. Biol.* 168:125-136.
82. Hinderliter, A., and S. May. 2006. Cooperative adsorption of proteins onto lipid membranes. *J. Phys.: Condens. Matter* 18:S1257-S1270.
83. Binnig, G., C. F. Quate, and C. Gerber. 1986. Atomic Force Microscope. *Phys. Rev. Lett.* 56:930-933.
84. Nečas, D., and P. Klapetek. 2012. Gwyddion: an open-source software for SPM data analysis. *Cent. Eur. J. Phys.* 10:181-188.
85. Axelrod, D., D. E. Koppel, J. Schlessinger, E. Elson, and W. W. Webb. 1976. Mobility measurement by analysis of fluorescence photobleaching recovery kinetics. *Biophys. J.* 16:1055-1069.

86. Soumpasis, D. M. 1983. Theoretical analysis of fluorescence photobleaching recovery experiments. *Biophys. J.* 41:95-97.
87. Lorenz, B., R. Keller, E. Sunnick, B. Geil, and A. Janshoff. 2010. Colloidal probe microscopy of membrane-membrane interactions: From ligand-receptor recognition to fusion events. *Biophys. Chem.* 150:54-63.
88. El Jastimi, R., and M. Lafleur. 1999. A dual-probe fluorescence method to examine selective perturbations of membrane permeability by melittin. *Biospectroscopy* 5:133-140.
89. Shlizerman, C., A. Atanassov, I. Berkovich, G. Ashkenasy, and N. Ashkenasy. 2010. De Novo Designed Coiled-Coil Proteins with Variable Conformations as Components of Molecular Electronic Devices. *J. Am. Chem. Soc.* 132:5070-5076.
90. Apostolovic, B., and H.-A. Klok. 2008. pH-Sensitivity of the E3/K3 Heterodimeric Coiled Coil. *Biomacromolecules* 9:3173-3180.
91. Apostolovic, B., S. P. E. Deacon, R. Duncan, and H.-A. Klok. 2010. Hybrid Polymer Therapeutics Incorporating Bioresponsive, Coiled Coil Peptide Linkers. *Biomacromolecules* 11:1187-1195.
92. Yano, Y., A. Yano, S. Oishi, Y. Sugimoto, G. Tsujimoto, N. Fujii, and K. Matsuzaki. 2008. Coiled-Coil Tag-Probe System for Quick Labeling of Membrane Receptors in Living Cells. *ACS Chem. Biol.* 3:341-345.
93. Zhou, N. E., C. M. Kay, and R. S. Hodges. 1992. Synthetic model proteins: the relative contribution of leucine residues at the nonequivalent positions of the 3-4 hydrophobic repeat to the stability of the two-stranded alpha-helical coiled-coil. *Biochemistry* 31:5739-5746.
94. Mason, J. M., M. A. Schmitz, K. M. Müller, and K. M. Arndt. 2006. Semirational design of Jun-Fos coiled coils with increased affinity: Universal implications for leucine zipper prediction and design. *Proc. Nat. Acad. Sci. USA* 103:8989-8994.
95. Hagemann, U. B., J. M. Mason, K. M. Müller, and K. M. Arndt. 2008. Selectional and Mutational Scope of Peptides Sequestering the Jun-Fos Coiled-Coil Domain. *J. Mol. Biol.* 381:73-88.
96. Mitra, K., I. Ubarretxena-Belandia, T. Taguchi, G. Warren, and D. M. Engelman. 2004. Modulation of the bilayer thickness of exocytic pathway membranes by membrane proteins rather than cholesterol. *Proc. Nat. Acad. Sci. USA* 101:4083-4088.
97. Kaiser, H.-J., A. Orłowski, T. Rog, T. K. M. Nyholm, W. Chai, T. Feizi, D. Lingwood, I. Vattulainen, and K. Simons. 2011. Lateral sorting in model membranes by cholesterol-mediated hydrophobic matching. *Proc. Nat. Acad. Sci. USA* 108:16628-16633.
98. Lewis, B. A., and D. M. Engelman. 1983. Lipid bilayer thickness varies linearly with acyl chain length in fluid phosphatidylcholine vesicles. *J. Mol. Biol.* 166:211-217.
99. Leonenko, Z. V., E. Finot, H. Ma, T. E. S. Dahms, and D. T. Cramb. 2004. Investigation of Temperature-Induced Phase Transitions in DOPC and DPPC Phospholipid Bilayers Using Temperature-Controlled Scanning Force Microscopy. *Biophys. J.* 86:3783-3793.
100. Schuy, S., E. Schäfer, N. Yoder, C., S. Hobe, K. Kumar, R. Vogel, and A. Janshoff. 2009. Coiled-Coil Lipopeptides Mimicking the Prehairpin Intermediate of Glycoprotein gp41. *Angew. Chem. Int. Ed.* 121:765-768.
101. Smith, E. A., and J. C. Weisshaar. 2011. Docking, Not Fusion, as the Rate-Limiting Step in a SNARE-Driven Vesicle Fusion Assay. *Biophys. J.* 100:2141-2150.
102. Cohen, F. S., and G. B. Melikyan. 2004. The Energetics of Membrane Fusion from Binding, through Hemifusion, Pore Formation, and Pore Enlargement. *J. Membr. Biol.* 199:1-14.
103. Monera, O. D., C. M. Kay, and R. S. Hodges. 1994. Electrostatic Interactions Control the Parallel and Antiparallel Orientation of alpha-Helical Chains in Two-Stranded alpha-Helical Coiled-Coils. *Biochemistry* 33:3862-3871.

REFERENCES

104. Myszka, D. G. 1997. Kinetic analysis of macromolecular interactions using surface plasmon resonance biosensors. *Curr. Opin. Biotechnol.* 8:50-57.
105. Ben-Tal, N., B. Honig, C. K. Bagdassarian, and A. Ben-Shaul. 2000. Association Entropy in Adsorption Processes. *Biophys. J.* 79:1180-1187.
106. MacDonald, R. I. 1990. Characteristics of self-quenching of the fluorescence of lipid-conjugated rhodamine in membranes. *J. Biol. Chem.* 265:13533-13539.
107. Parlati, F., T. Weber, J. A. McNew, B. Westermann, T. H. Söllner, and J. E. Rothman. 1999. Rapid and efficient fusion of phospholipid vesicles by the α -helical core of a SNARE complex in the absence of an N-terminal regulatory domain. *Proc. Nat. Acad. Sci. USA* 96:12565-12570.
108. Abdulreda, M. H., A. Bhalla, E. R. Chapman, and V. T. Moy. 2008. Atomic Force Microscope Spectroscopy Reveals a Hemifusion Intermediate during Soluble N-Ethylmaleimide-Sensitive Factor-Attachment Protein Receptors-Mediated Membrane Fusion. *Biophys. J.* 94:648-655.
109. Abdulreda, M. H., A. Bhalla, F. Rico, P.-O. Berggren, E. R. Chapman, and V. T. Moy. 2009. Pulling force generated by interacting SNAREs facilitates membrane hemifusion. *Integr. Biol.* 1:285-336.
110. Vaz, W. L. C., R. M. Clegg, and D. Hallmann. 1985. Translational diffusion of lipids in liquid crystalline phase phosphatidylcholine multibilayers. A comparison of experiment with theory. *Biochemistry* 24:781-786.
111. Pettersen, E. F., T. D. Goddard, C. C. Huang, G. S. Couch, D. M. Greenblatt, E. C. Meng, and T. E. Ferrin. 2004. UCSF Chimera—A visualization system for exploratory research and analysis. *J. Comput. Chem.* 25:1605-1612.
112. Stern, E., R. Wagner, F. J. Sigworth, R. Breaker, T. M. Fahmy, and M. A. Reed. 2007. Importance of the Debye Screening Length on Nanowire Field Effect Transistor Sensors. *Nano Lett.* 7:3405-3409.
113. Pobbati, A. V., A. Stein, and D. Fasshauer. 2006. N- to C-Terminal SNARE Complex Assembly Promotes Rapid Membrane Fusion. *Science* 313:673-676.
114. Fasshauer, D., and M. Margittai. 2004. A Transient N-terminal Interaction of SNAP-25 and Syntaxin Nucleates SNARE Assembly. *J. Biol. Chem.* 279:7613-7621.
115. Lorenz, B., L. Alvarez de Cienfuegos, M. Oelkers, E. Kriemen, C. Brand, M. Stephan, E. Sunnick, D. Yüksel, V. Kalsani, K. Kumar, D. B. Werz, and A. Janshoff. 2012. Model System for Cell Adhesion Mediated by Weak Carbohydrate-Carbohydrate Interactions. *J. Am. Chem. Soc.* 134:3326-3329.
116. Bornschlöggl, T., and M. Rief. 2006. Single Molecule Unzipping of Coiled Coils: Sequence Resolved Stability Profiles. *Phys. Rev. Lett.* 96:118102.
117. Bornschlöggl, T., and M. Rief. 2008. Single-Molecule Dynamics of Mechanical Coiled-Coil Unzipping. *Langmuir* 24:1338-1342.
118. Bornschlöggl, T., J. C. M. Gebhardt, and M. Rief. 2009. Designing the Folding Mechanics of Coiled Coils. *ChemPhysChem* 10:2800-2804.
119. Hertz, H. 1882. Über die Berührung fester elastischer Körper. *J. für die reine u. angew. Math.* 92:136.
120. Kiselev, V. Y., D. Marenduzzo, and A. B. Goryachev. 2011. Lateral Dynamics of Proteins with Polybasic Domain on Anionic Membranes: A Dynamic Monte-Carlo Study. *Biophys. J.* 100:1261-1270.
121. Sieber, J. J., K. I. Willig, C. Kutzner, C. Gerding-Reimers, B. Harke, G. Donnert, B. Rammner, C. Eggeling, S. W. Hell, H. Grubmüller, and T. Lang. 2007. Anatomy and Dynamics of a Supramolecular Membrane Protein Cluster. *Science* 317:1072-1076.
122. Liu, T., W. C. Tucker, A. Bhalla, E. R. Chapman, and J. C. Weisshaar. 2005. SNARE-Driven, 25-Millisecond Vesicle Fusion In Vitro. *Biophys. J.* 89:2458-2472.

Appendix

Abbreviations

AcCN	acetonitrile
AFM	atomic force microscopy
Ala, A	alanine
(ATR-)FT IR	(attenuated total reflection) Fourier transformed infrared
BODIPY	2-(4,4-difluoro-5-methyl-4-bora-3a,4a-diaza-s-inacen-3-dodecyl)-1-hexadecyl- <i>sn</i> -glycero-3-phosphocholine
CD	circular dichroism
chol	cholesterol
CLSM	confocal laser scanning microscopy
Cys, C	cysteine
DΔPPC	1,2-dipalmitoleoyl- <i>sn</i> -glycero-3-phosphocholine
DEPC	1,2-dieicosenoyl- <i>sn</i> -glycero-3-phosphocholine
DIEA	<i>N,N'</i> -diisopropylethylamine
DMF	<i>N,N'</i> -dimethylformamide
DMOPC	1,2-dimyristoleoyl- <i>sn</i> -glycero-3-phosphocholine
DOPC	1,2-dioleoyl- <i>sn</i> -glycero-3-phosphocholine
DOPE	1,2-dioleoyl- <i>sn</i> -glycero-3-phosphoethanolamine
DPPC	1,2-dipalmityl- <i>sn</i> -glycero-3-phosphocholine
DPPE	1,2-dipalmityl- <i>sn</i> -glycero-3-phosphoethanolamine
E3Cys	peptide Ac-(EIAALEK) ₃ -GWGGGC-NH ₂
EDT	1,2-ethanedithiol
ESI-(HR-)MS	electrospray ionization (high resolution) mass spectrometry
Fmoc	<i>N</i> -Fluorenylmethoxycarbonyl
FRAP	fluorescence recovery after photobleaching
Glu, E	glutamic acid
Gly., G	glycine
HBTU	2-(1H-Benzotriazole-1-yl)-1,1,3,3-tetramethyluronium-hexafluorophosphate
HEPES 7.4	4-(2-hydroxyethyl)-1-piperazineethanesulfonic acid buffered solution, pH 7.4
<i>i</i> -E3Cys	peptide Ac-(KELAAIE) ₃ -GWGGGC-NH ₂

<i>i</i> -E3PEG	peptide Ac-(KELAAIE) ₃ -GW(PEG) ₁₁ C-NH ₂
<i>i</i> -K3Cys	peptide Ac-WG-(EKLAAIK) ₃ -GGGGC-NH ₂
<i>i</i> -K3PEG	peptide Ac-WG-(EKLAAIK) ₃ -(PEG) ₁₁ C-NH ₂
Ile, I	isoleucine
K3Cys	peptide Ac-WG-(KIAALKE) ₃ -GGGGC-NH ₂
Leu, L	leucine
LP-X	lipopeptide formed of MCC-phospholipid and peptide X
LUV	large unilamellar vesicle
Lys, K	lysine
MCCDOPE	1,2-dioleoyl- <i>sn</i> -glycero-3-phosphoethanolamine-N-[4-(<i>p</i> -maleimidomethyl)cyclohexane-carboxamide]
MCCDPPE	1,2-dipalmitoyl- <i>sn</i> -glycero-3-phosphoethanolamine-N-[4-(<i>p</i> -maleimidomethyl)cyclohexane-carboxamide]
MLV	multilamellar vesicles
MPS	membrane probe force spectroscopy
OG488	Oregon Green 488 maleimide
PB 6.8	phosphate buffered solution, pH 6.8
PEG	polyethylene glycol
POPC	1-palmitoyl-2-oleoyl- <i>sn</i> -glycero-3-phosphocholine
POPE	1-palmitoyl-2-oleoyl- <i>sn</i> -glycero-3-phosphoethanolamine
ROI	region of interest
RP-A	polar solvent for RP-HPLC (H ₂ O / AcCN / TFA 99:1:0.1)
RP-B	non-polar solvent for RP-HPLC (H ₂ O / AcCN / TFA 10:90:0.05)
RP-HPLC	reversed phase high pressure liquid chromatography
SNARE	soluble <i>N</i> -ethylmaleimide-sensitive-factor attachment protein receptor
SPPS	solid phase peptide synthesis
SPR	surface plasmon resonance
SRB	sulforhodamine B
SSM	solid supported membrane
SUV	small unilamellar vesicle
Texas Red	TexasRed-1,2-dihexadecyl- <i>sn</i> -glycero-3-phosphoethanolamine
TFA	trifluoroacetic acid
TIS	triisopropylsilane
Trp, W	tryptophan
UV/vis	ultraviolet / visual wavelength range

List of Figures

- FIGURE I.1** Membrane topology during membrane fusion pathway. *From left to right:* Membranes come into close contact until a point-like protrusion is formed. Subsequently, a hemifusion stalk is formed, which can be either expanded to a hemifusion diaphragm or opened up to a full fusion pore directly. 2
- FIGURE I.2** SNARE mediated membrane fusion. (A) Schematic drawing of a SNARE mediated interaction of a vesicle with a target membrane. Enlarged drawing of SNARE protein complex (scattered box) is shown below. (B) Structure of the core complex consisting of syntaxin (*red*), synaptobrevin (*blue*) and SNAP25 (*green*) attached to bilayers via transmembrane domains (*yellow*). 4
- FIGURE III.1** Schematic drawing of an unilamellar vesicle (A) and a solid supported lipid membrane (B). 10
- FIGURE III.2** Schematic drawing of fatty acid chain packing in (A) gel phase and (B) fluid phase lipid bilayers. 11
- FIGURE III.3** Chemical structures of maleimide functionalized lipids MCCDPPE (gel phase) and MCCDOPE (fluid phase). 12
- FIGURE III.4** Chemical structures of used lipid conjugated fluorophores Texas Red (A) and BODIPY (B) as well as their absorption and emission spectra (C). Spectrum of BODIPY is shown in green, Texas Red in red. Absorption line is represented by a dotted line, emission spectra is shown as solid line. 13
- FIGURE III.5** Schematic representation of a parallel (A) and an antiparallel (B) dimeric coiled-coil. In the upper panel the relative positions of N- and C-terminus are shown; in the lower panel helical wheel diagrams are presented. One wheel represents one α -helical heptad repeat shown from the top, starting with N- or C-terminus, respectively, as indicated by the letter inside the wheel. The positions where ionic (red) and hydrophobic (blue) interactions are located are indicated with arrows. 16
- FIGURE III.6** Schematic presentation of reaction sequences applied in solid phase peptide synthesis. For each amino acid a new coupling step followed by a deprotection is carried out... 18
- FIGURE III.7** Chemical structures of activation reagent HBTU and of Rink Amide MBHA resin. ... 18
- FIGURE III.8** Reactions carried out in SPPS. (A) Deprotection (removal of Fmoc protecting groups); (B) coupling reaction of amino acid building blocks; (C) acetylation of N-terminal amino group; (D) cleavage of crude peptide from the polystyrene resin and removal of all side-chain protecting groups. 19
- FIGURE III.9** Schematic drawing of RP-HPLC setup. The sample is injected to the HPLC and eluted with the solvent mixture. Peptides can be identified in a chromatogram using a UV detector at $\lambda = 220$ nm, the wavelength of absorbance for peptide bonds. 21

- FIGURE III.10** Purification of *i*-E3Cys (yellow) and *i*-K3Cys (green) by (A) preparative RP-HPLC with a linear polarity gradient (see table III.3). Collected fractions are highlighted in grey. (B) Purity control determined with analytical RP-HPLC..... 23
- FIGURE III.11** Schematic drawing of *in situ* coupling reaction between MCC-phospholipid and cysteine-containing peptide on a SSM (solid supported membrane). 25
- FIGURE III.12** Chemical structures of hybrid lipopeptides formed of MCCDOPE as lipid moiety with *i*-K3Cys and *i*-K3PEG, respectively..... 25
- FIGURE III.13** Principle of size exclusion chromatography (SEC) applied for vesicle purification. The grey filling is the stationary phase, the blue phase on top depicts the employed elution buffer. Vesicles are shown in dark blue, small molecules (*e.g.* excess peptides or buffer ingredients) which were removed are shown as red dots. 27
- FIGURE III.14** UV/Vis absorption spectra of *i*-E3Cys labeled vesicles. The eluted 2.5 mL were collected in 8 fractions (8th not shown here). The highest concentration of peptide coupled to SUV was found in fractions 4-6..... 27
- FIGURE III.15** Chemical structures of Sulforhodamin B (SRB) and Oregon Green 488 maleimide (OG488)..... 28
- FIGURE IV.1** Schematic drawing of IR beam path in (A) transmission FT IR and on a (B) ATR crystal with formation of an evanescent field. Red line indicates IR beam which is total reflected at the ATR crystal..... 32
- FIGURE IV.2** ATR-FT IR spectra of lipids with its characteristic vibrations. (A) POPC at room temperature with marked stretching vibrations ν and bending vibrations δ . Area highlighted in grey depicts stretching vibrations sensitive to the lipid phase. (B) DPPC in a temperature range of 34-50 °C. Red spectrum is recorded at $T_m(\text{DPPC}) = 42$ °C, black spectra are collected at $T > 42$ °C, and grey spectra are collected at $T < 42$ °C. Stretching vibrations of -CH₃ moieties are marked here due to better visibility. 33
- FIGURE IV.3** Schematic drawings of amide I band in FT IR spectra consisting of (A) α -helix, (B) β -sheet, and (C) random coil. 34
- FIGURE IV.4** Scheme of an absorption spectrometer. In UV/Vis spectroscopy only light source, monochromator, sample, and detector are connected in series, while for a CD spectrometer the green marked polarizer and CD modulator are added to the setup. 36
- FIGURE IV.5** Schematic drawing of CD spectra from proteins with mainly α -helical (pink), β -sheet (blue) and random structure (light blue). Scattered line indicates ellipticity of 0..... 39
- FIGURE IV.6** Schematic drawing of a setup used in surface plasmon resonance (SPR) spectroscopy experiments..... 41
- FIGURE IV.7** Schematic drawing of signal recorded in SPR spectroscopy while association and dissociation of an analyte, followed by a regeneration step until baseline is reached again. 42

- FIGURE IV.8** Schematic drawing of a setup used in a null ellipsometer like it was employed in this work..... 45
- FIGURE IV.9** Simulated dependency of δ and ψ to layer thickness d in a range of 0-200 nm (A) and a zoom in (orange marked area in A) for thin layers with a thickness of 0-10 nm (B)..... 46
- FIGURE IV.10** Exemplarily presentations of isotherms following a Langmuir equation (grey) and a Bragg-Williams equation (red). 47
- FIGURE IV.11** (A) Schematic drawing of laser reflection on cantilever tip and detection at 4-quadrants photodiode. (B) Schematic presentation of tapping mode for imaging. 48
- FIGURE IV.12** Schematic presentation of a FRAP experiment and subsequent analytical workup. (A) Time-resolved image series, starting with unbleached image with definition of two ROIs. The black ROI is bleached (2nd image) and the recovery of fluorescence intensity is collected with time (3rd and 4th image). (B) Determined fluorescence intensity for bleached ROI (black) and unbleached reference ROI (grey). (C) Normalized fluorescence recovery curve (black) with Axelrod fit function (red) and immobile fraction marked in grey. (D) Determination of ROI size by fitting Gaussian function (red) and defining half-width ω to intensity profile along bleached ROI (grey). 50
- FIGURE IV.13** Schematic drawing of different labeling procedures. (A) BODIPY lipid (green) is introduced in a concentration of 1 mol% to the SSM. Afterwards, peptides can be added to form lipopeptides and coiled-coil heterodimers. (B) Complete coiled-coil structure is labeled by the means of coupling an OG488 moiety (green) to remaining cysteine groups..... 52
- FIGURE IV.14** Schematic presentation of lipid and content mixing dequenching assays. Black and white points indicate fusion-mediating moieties. Quenched fluorophores are represented by pink stars, fluorescently active fluorophores are marked as bright stars. 54
- FIGURE IV.15** Stern-Volmer plot for Texas Red quenching in DOPC vesicles. F_{quenched} is fluorescence intensity in intact vesicles, F_{max} the intensity after disruption of SUV with detergent (SDS, $c = 0.2\%$). Points correspond to measured data; grey line shows a linear fit. Stern-Volmer constant K_{SV} was determined from the slope. 55
- FIGURE V.1** (A) Schematic drawing of *in situ* coupling reaction between MCC-phospholipid and cysteine-containing peptide followed by coiled-coil formation on a SSM (solid supported membrane). (B) Corresponding height increases for processes displayed in A (i = spreading of SSM; ii = *in situ* coupling reaction; iii = coiled-coil formation). 60
- FIGURE V.2** CD spectra of employed peptides and their heterodimeric mixtures ($c_{\text{peptide}} = 0.1$ mM in PB 6.8). (A) E3Cys (open circles), K3Cys (crosses) and their 1:1 mixture (filled circles). (B) *i*-E3Cys (open triangles), *i*-K3Cys (crosses) and their 1:1 mixture (filled triangles). (C) *i*-E3PEG (open squares), *i*-K3PEG (crosses) and their 1:1 mixture (filled squares). 61
- FIGURE V.3** Amide I band in transmission FT IR spectra of E- and K-peptides in solution (D₂O with 50 mM NaCl) as monomer and after heterodimerization. Numbers in graph indicate position of band maxima. (A) E3Cys (red), K3Cys (blue) and their 1:1 mixture (black). (B) Deconvolution of

amide I band from E3Cys/K3Cys heterodimer shown above by multiple Gaussian fits to document formation of coiled-coil dimers. The positions of Gaussian functions were estimated by computing the second derivative of the spectra. Experimental data is shown in black, grey curves are Gaussian fits, grey scattered line represents the sum of all Gaussian fit. (C) *i*-E3Cys (yellow), *i*-K3Cys (green) and their 1:1 mixture (black). (D) Deconvolution as described above for *i*-E3Cys/*i*-K3Cys heterodimer. (E) *i*-E3PEG (yellow), *i*-K3PEG (green) and their 1:1 mixture (black). (F) Deconvolution as described above for *i*-E3PEG/*i*-K3PEG heterodimer. 63

FIGURE V.4 Spectra of antiparallel coiled-coil heterodimers composed of *i*-K3Cys and E3Cys (filled circles) or K3Cys and *i*-E3Cys (open circles), respectively. Amount of α -helix was determined to be 79 % (filled circles) and 73 % (open circles), respectively. 64

FIGURE V.5 (A) Spreading process for DEPC 100 % (black) and DEPC/chol 71:29 (grey). SUV were added at $t = 0$, scattered lines indicate start of rinsing. (B) Mean determined layer thicknesses for spreaded bilayers with varying acyl chain lengths consisting of 100 % unsaturated lipids (black circles) and mixtures with cholesterol (PC/chol 71:29) (grey); lines represent linear regression with indicated slopes b . Used lipids: DMOPC (di14:1), Δ PPC (di16:1), DOPC (di18:1) and DEPC (di20:1)..... 66

FIGURE V.6 Exemplary binding kinetics of E- and K-peptides to a DOPC/MCCDOPE 90:10 lipid bilayer spread on silicon oxide with ellipsometry in PB 6.8. Arrows indicate peptide addition and final rinsing, SUV to form SSM were added at the beginning of experiment. Before each addition of substance, a rinsing step was carried out of at least 5 min (not indicated in graphs). (A) Lipopeptide formation of K3Cys (grey) / E3Cys (black) followed by addition of E3Cys (grey) / K3Cys (black). (A) Lipopeptide formation of *i*-K3Cys (grey) / *i*-E3Cys (black) followed by addition of *i*-E3Cys (grey) / *i*-K3Cys (black). (C) Lipopeptide formation of *i*-K3PEG (grey) / *i*-E3PEG (black) followed by addition of *i*-E3PEG (grey) / *i*-K3PEG (black). 68

FIGURE V.7 Exemplary time-resolved ellipsometry data of coiled-coil formation with subsequent rinsing (black). Graphs are magnified views from corresponding parts shown in Figure V.6 B, SSM consisted of DOPC/MCCDOPE 90:10. Double exponential fits while adsorption phase are shown as grey scattered lines, exponential fits computing dissociation of coiled-coil complex are shown as red scattered lines. (A) Addition of *i*-K3Cys to *i*-E3Cys lipopeptides. (B) Addition of *i*-E3Cys to *i*-K3Cys lipopeptides. 70

FIGURE V.8 (left panel) ATR-FT IR spectra of plain solid supported membranes (.....) consisting of DOPC/MCCDOPE 90:10 in D₂O with 50 mM NaCl spread on a Si-covered ZnSe-crystal. Lipid bands and amide I region are shown. Lipopeptides were formed with K-peptides covalently attached to the maleimide headgroups of MCCDOPE (- - -). Solid lines indicate spectra after coiled-coil formation upon addition of E-peptides (—). (right panel) Time course of lipopeptide coupling reaction followed by coiled-coil formation shown left: Intensity of amide I band is plotted vs. time. Time course starts with completed bilayer ($t = 0$). Addition of peptides and rinsing is indicated by arrows. (A, B) SSM + K3Cys (lipopeptide, blue arrow) + E3Cys (red arrow). (C, D) SSM + *i*-K3Cys (lipopeptide, green arrow) + *i*-E3Cys (yellow arrow). (E, F) SSM + *i*-K3PEG (lipopeptide, green arrow) + *i*-E3PEG (yellow arrow). In (E) lipid peaks are only present in spectrum directly after spreading, because this spectrum was subtracted from the two other shown here due to water vapor correction. 72

FIGURE V.9 Time-resolved ATR-FT IR spectroscopy of coiled-coil formation. Plots show α -helical content (A) and protein concentration in evanescent field (B). Spectral data was analyzed using QUANT2, a software provided by Bruker Optics. SSM was formed from DOPC / MCCDOPE 90:10 SUV, then *i*-K3PEG was covalently attached to the bilayer via maleimide chemistry. Afterwards, *i*-E3PEG was added in solution. Only coiled-coil formation of LP-*i*-K3PEG with *i*-E3PEG is shown in graph, scattered lines indicate beginning and end of dimerization. Before and after peptide addition, sample was rinsed with D₂O (with 50 mM NaCl). Grey curves represent experimental data, black circles show biexponential fit function while coiled-coil formation (A), black crosses in (B) show monoexponential fit function for rinsing off peptide. 73

FIGURE V.10 Deconvolution of amide I band for coiled-coil build of LP-K + E-peptides on DOPC/MCCDOPE 90:10 in D₂O with 50 mM NaCl spread on a Si-covered ZnSe-crystal. Spectra were collected using an ATR-FT IR spectroscopy setup. Numbers in graph indicate position of band maxima. Single Gaussian fits are shown in grey, amide I band of spectra in black. Scattered grey lines represent the sum of all Gaussian fits. (A) SSM + K3Cys (lipopeptide) + E3Cys. (B) SSM + *i*-K3Cys (lipopeptide) + *i*-E3Cys. (C) SSM + *i*-K3PEG (lipopeptide) + *i*-E3PEG. 74

FIGURE V.11 Time-resolved ellipsometry data determined on silica in PB 6.8. (A) *In situ* coupling of *i*-K3PEG to DOPC/MCCDOPE bilayers with the compositions 92:8, 94:6, and 98:2 (from left to right, arrows mark point of peptide addition). (B) *i*-K3PEG added in increasing concentrations (see graph) to a SSM made of DOPC/MCCDOPE 90:10. 75

FIGURE V.12 Layer thickness of K-peptides (markers) added to SSM containing different amounts of MCCDOPE. Presented values *b* are the corresponding slopes of the linear regression (dotted lines). Mean values with their standard deviation are given. (A) LP-K3Cys formation. (B) LP-*i*-K3Cys formation. (C) LP-*i*-K3PEG formation (no mean values were calculated here, error corresponds to instrumental error). 76

FIGURE V.13 Controls with neat DOPC membranes. Before and after each step (indicated by scattered lines) samples were rinsed with buffer. (A) Layer thicknesses calculated from ellipsometry measurements (in PB 6.8) of bilayer spreading (DOPC 100 %) with subsequent addition of *i*-E3Cys and afterwards *i*-K3Cys (*i*-K3Cys addition shown magnified in inset). (B) Time course of ATR-FT IR flow cell measurement in D₂O + 50mM NaCl. Intensity of amide I band is shown while bilayer spreading (DOPC 100 %) with subsequent addition of K3Cys and afterwards E3Cys. 77

FIGURE VI.1 Schematic drawing of peptide-mediated membrane-membrane interaction through coiled-coil formation. Parallel coiled-coil formation of peptides E3Cys and K3Cys (A) and inverted peptides *i*-E3Cys and *i*-K3Cys (B), respectively, are envisioned to be capable of inducing lipid mixing like hemifusion or fusion, while for antiparallel coiled-coil formation (C) only docking events are expected. 80

FIGURE VI.2 Concentration dependent of $[\theta]_{MRW}$ at 220 nm measured by CD spectroscopy for heterodimeric coiled-coil mixtures to determine K_D via dilution experiments. On left side parallel, on right side antiparallel coiled-coil formation are shown. (A) Data for dimer formed of E3Cys and K3Cys; solid circles. (B) Dimer formed of *i*-E3Cys and *i*-K3Cys; solid triangles. (C) Dimer

formed of *i*-E3Cys and K3Cys; open circles. (D) Dimer formed of E3Cys and *i*-K3Cys; open triangles. Resulting K_D values are presented with corresponding fits shown as grey lines (75). .. 81

FIGURE VI.3 Association ($t = 0-300$ s) and dissociation ($t = 300-600$ s) of E-peptides coupled to immobilized K-peptides on a hydrogel monitored with SPR spectroscopy. E-peptides were added at a concentration of $15 \mu\text{M}$. On left side parallel, on right side antiparallel coiled-coil formation are shown. Association of peptides is described by the rate of assembly k_{on} , while dissociation of the peptide assembly follows a monoexponential function (k_{off}). Fits are shown as grey lines, for corresponding values see Table VI.1. (A) E3Cys added to immobilized K3Cys (solid circles). (B) *i*-E3Cys added to immobilized *i*-K3Cys (solid triangles). (C) *i*-E3Cys added to immobilized K3Cys (open circles). (D) E3Cys added to immobilized *i*-K3Cys (open triangles). 82

FIGURE VI.4 Langmuir adsorption isotherms determined with ellipsometry represent coiled-coil formation of *i*-K3Cys and *i*-E3Cys. Solid triangles represent the measured data points while solid lines represent corresponding fit functions. (A) Comparison of the preformed lipopeptide (LP-) on a DOPC/MCCDOPE 90:10 lipid bilayer in PB 6.8. Addition of *i*-K3Cys to LP-*i*-E3Cys is shown in grey, addition of *i*-E3Cys to LP-*i*-K3Cys is shown in black. (B) Addition of *i*-E3Cys to LP-*i*-K3Cys on a SSM formed of DOPC/MCCDOPE 90:10 (black) and of DOPC/MCCDOPE 97:3 (grey). 85

FIGURE VI.5 Ellipsometry adsorption isotherms representing coiled-coil formation of E-peptides binding to K-lipopeptides. Bilayers were formed from DOPC/MCCDOPE 97:3, afterwards K-peptides were coupled covalently to the surface. The isotherm was measured by subsequently increasing the added E-peptide concentration. (A) Parallel coiled-coil formation. Solid circles: LP-K3Cys + E3Cys; solid triangles: LP-*i*-K3Cys + *i*-E3Cys; data were fitted according to Langmuir (fits: grey line). (B) Antiparallel coiled-coil formation. Open circles: LP-K3Cys + *i*-E3Cys; open triangles: LP-*i*-K3Cys + E3Cys; data were fitted according to Langmuir theory for LP-*i*-K3Cys + E3Cys, while for LP-K3Cys + *i*-E3Cys a Bragg-Williams isotherm was used (fits: grey line). 86

FIGURE VI.6 Lipid mixing and content mixing of SUVs decorated with E- and K-peptides. 100 % refers to 1:1 vesicle mixing. (A) Texas Red self-quenching assay for lipid mixing. Labeled SUVs were functionalized with K-peptides and mixed with unlabeled E-peptide bearing SUVs (start of mixing: $t = 0$). Parallel peptide packing facilitates lipid mixing (solid circles: K3Cys + E3Cys; solid triangles: *i*-K3Cys + *i*-E3Cys), in contrast to antiparallel coiled-coil formation (open circles: K3Cys + *i*-E3Cys, open triangles: *i*-K3Cys + E3Cys). (B) Content mixing monitored with a sulforhodamin B (SRB) self-quenching assay. K-peptide functionalized SUVs were filled with SRB (20 mM) and mixed with buffer filled SUVs displaying E-peptides. At time $t = 0$ Ca^{2+} ions were added ($C_{\text{final}} = 8$ mM). Markers are identical to those used in A. 90

FIGURE VII.1 Schematic drawing of the envisioned lateral lipopeptide clustering on SSM, which partially dissolve upon coiled-coil heterodimerization. 94

FIGURE VII.2 Results from fluorescence recovery after photobleaching (FRAP) experiments related to lateral mobility of lipid matrix. POPC/MCCDOPE/BODIPY 89:10:1 was spread on glass in PB 6.8 and functionalized with lipopeptides followed by successive coiled-coil formation to determine diffusion coefficient D (green bars) and mobile fraction F_{mob} (black circles). Plain SSM (POPC*) was used as reference which was compared to lipopeptide decorated SSM (LP-X) and SSM with complete coiled-coil structures (LP-X + Y). 95

FIGURE VII.3 Results from fluorescence recovery after photobleaching (FRAP) experiments related to determine lateral mobility of coiled-coil complexes in lipid matrix. POPC/MCCDOPE 90:10 was spread on glass in PB 6.8 and functionalized with lipopeptides followed by successive coiled-coil formation. (A) Added peptides were afterwards labeled with Oregon Green 488 maleimide (OG488, green star). (B) Determined diffusion coefficients D (green bars) and mobile fractions F_{mob} (black circles) for tested $LP-X + Y-OG488$ combinations..... 96

FIGURE VII.4 Typical FRAP fluorescence micrographs. Images were collected shortly after bleaching pulse. All pictures are $(30 \times 30) \mu\text{m}^2$. First column: plain SSM made of POPC/MCCDOPE/BODIPY 89:10:1 ($POPC^*$) Second column: $POPC^*$ functionalized with lipopeptides and with complete coiled-coil structures (third column). Fourth column: SSM made of POPC/MCCDOPE 90:10 functionalized with complete coiled-coil structures which were subsequently labeled *in situ* with OG488..... 98

FIGURE VII.5 Topographical AFM images of E-lipopeptides embedded in DPPC/MCCDPPE 97:3 spread on mica (black in images) in PB 6.8. Clustering of lipopeptides is indicated with arrows (upper row); (second row) images were collected after corresponding coiled-coil forming peptides were added. Height profiles shown below the images were collected along scattered white lines. Scale bars: 400 nm, height of all images is set to 10 nm. (A) LP-E3Cys, (B) LP-E3Cys + K3Cys, (C) LP-*i*-E3Cys, (D) LP-*i*-E3Cys + *i*-K3Cys, (E) LP-*i*-E3PEG, (F) LP-*i*-E3PEG + *i*-K3PEG..... 100

FIGURE VII.6 Topographical AFM images of K-lipopeptides embedded in DPPC/MCCDPPE 97:3 spread on mica (black in images) in PB 6.8. Clustering of lipopeptides is indicated with arrows (upper row); (second row) images were collected after corresponding coiled-coil forming peptides were added. Height profiles shown below the images were collected along scattered white lines. Scale bars: 400 nm, height of all images is set to 10 nm. (A) LP-K3Cys, (B) LP-K3Cys + E3Cys, (C) LP-*i*-K3Cys, (D) LP-*i*-K3Cys + *i*-E3Cys, (E) LP-*i*-K3PEG, (F) LP-*i*-K3PEG + *i*-E3PEG..... 101

FIGURE VII.7 AFM images of K-lipopeptides attached to POPC/MCCDOPE 97:3 spread on mica (black in images) in PB 6.8. Height profiles (right next to the images) were collected along scattered white lines. Scale bars: 300 nm. (A) LP-K3Cys, (B) LP-*i*-K3Cys..... 102

FIGURE VII.8 Schematic explanation of grain analysis. (A) AFM image of DPPC/MCCDPPE 97:3 functionalized with *i*-K3Cys on mica in PB 6.8. Grain analysis was carried out using a height threshold; grains are marked red in image. (B) Estimation of dimensional size of peptides. Size could be determined to be 2.7 nm in height and 1.6 nm in width. Grey blocks indicate a repulsion based on the debye length λ_D , between peptides. (C) Schematic drawing of cluster (orange-red). Peptides inside are considered inactive, peptides in contact area (black) are considered active. 103

FIGURE VII.9 Coiled-coil formation on lipopeptide containing lipid bilayers monitored with time-resolved ellipsometry. All SSM were made of DOPC/MCCDOPE 97:3, experiments were carried out on silica in PB 6.8. Green marked area displays amount of fast initial binding within time constant τ_1 (peptides referred to as "active"), grey marked area displays subsequent binding until full coverage within slow time constant τ_2 (peptides referred to as "inactive"). (A) Addition of *i*-E3Cys to LP-*i*-K3Cys. (B) Addition of *i*-K3Cys to LP-*i*-E3Cys. 105

FIGURE VII.10 Coiled-coil interactions lead to increased membrane-membrane adhesion. (A) Schematic drawing of the experimental setup for the analysis of membrane interactions mediated by *i*-K3Cys/*i*-E3Cys coiled-coil formation. (B) Force-distance curves (retraction) as recorded for two neat POPC membranes (grey) and interactions between POPC membranes decorated with 3 mol% *i*-K3Cys and *i*-E3Cys peptides (red). Forces of ≈ 250 pN act on the membrane probe upon peptide interaction..... 107

FIGURE VII.11 Variation of peptide concentration and interaction time for *i*-K3Cys/*i*-E3Cys-mediated membrane interaction forces. (A) Increased peptide surface concentration leads to enhanced interaction forces at a dwell time of 1 s. The median of membrane interaction force values varies between ≈ 80 pN at 0.1 mol% and ≈ 550 pN at 10 mol% lipopeptides in POPC membrane. (B) Increased membrane interaction time (dwell time t_{dwell}) leads to enhanced interaction forces (3 mol% MCCDOPE). The median of interaction forces ranges from ≈ 40 pN with no additional dwell time to ≈ 200 pN with $t_{\text{dwell}} = 5$ s. (C) Most probable interaction forces between *i*-K3Cys and *i*-E3Cys decorated membranes are ≈ 100 pN, ≈ 190 pN, ≈ 330 pN, and ≈ 480 pN (3 mol% MCCDOPE). Multiple force peaks can be interpreted in terms of the formation of several *i*-K3Cys/*i*-E3Cys interaction clusters. Kernel density estimation (bright red) shows maximum forces at 100 pN, 196 pN, 342 pN, 475 pN, and 560 pN..... 108

FIGURE VII.12 AFM images of POPC/MCCDOPE 97:3 decorated with *i*-K3Cys (A) and *i*-E3Cys (B). Both images were collected in PB 6.8 on mica substrates. Contact area estimated for MPS measurements is depicted as a white circle ($\varnothing \approx 120$ nm). (C) Membrane interaction scenario involving *i*-K3Cys/*i*-E3Cys peptides and spatial reduction of contact area. In combination with the contact zone defined by the probe geometry (indicated by black ring), coiled-coil formation (red dots) is only possible in intersection points of contact zone and clusters (green), with ≈ 100 pN force detection per cluster and between freely moving lipopeptides. 109

FIGURE VII.13 Force-distance curve (retraction) for interactions between POPC/MCCDOPE 99.9:0.1 membranes decorated with *i*-K3Cys and *i*-E3Cys peptides. Curve displays a single worm-like chain unbinding event at $F_{\text{interaction}} \approx 25$ pN. 110

List of Tables

TABLE III.1 Abbreviated lipid names, chemical names, saturation of fatty acid chains and the phase transition temperature T_m of lipids used in this work. *) [(number of carbons in fatty acid chain):(number of double bonds)] ratio is given for alkyl chains at position 1 and 2.....	11
TABLE III.2 Schematic drawings, names and primary sequences of peptides. N-terminus is acetylated, C-terminus amidated.....	20
TABLE III.3 Linear polarity gradients used in RP-HPLC for peptide purification. First line names the peptides the gradient was applied to. Amounts of RP-A (H ₂ O / AcCN / TFA 99:1:0.1) and RP-B (H ₂ O / AcCN / TFA 10:90:0.05) are given in volume percentage. 0-20 min: linear polarity gradient; 21-30 min: cleaning of stationary phase; 31-39 min: preparation of stationary phase.....	22
TABLE III.4 Retention times t_R and determined purity from analytical RP-HPLC (20-80 % RP-B, 20 min; * for <i>i</i> -K3PEG: 30-45 % RP-B, 20 min), m/z ratio for $[M+H]^+$ ion determined from ESI-MS (HR-MS), and calculated molar weight of synthesized peptides.....	23
TABLE III.5 Name, composition, pH and application of employed working solutions.....	29
TABLE IV.1 Summarized absorbance maxima λ_{max} and corresponding extinction coefficients ϵ for chromophores used in this thesis (60, 71).	37
TABLE IV.2 Angles of polarizer, $\lambda/4$ -plate, and analyzer for “Null” adjusting and their dependencies to determined del and psi	46
TABLE V.1 Distribution of secondary structure fractions of peptides before and after formation of coiled-coil assemblies obtained from CD measurements in solution. All measurements were carried out in PB 6.8 with an overall peptide concentration of $c = 0.1$ mM. Percentages were obtained from <i>DichroWeb</i> online analysis software (72, 73).....	62
TABLE V.2 Distribution of secondary structure fractions of peptides after antiparallel coiled-coil formation obtained from CD spectroscopy measurements in solution (PB 6.8; $c_{peptide} = 0.1$ mM). Percentages were obtained from <i>DichroWeb</i> online analysis software (72, 73).....	65
TABLE V.3 Mean determined heights for spreaded bilayers consisting of 100 % unsaturated PC-lipids (h_{PC}) and PC/chol 71:29 ($h_{PC/chol}$), respectively. The last row gives the ratio of height increase.	67
TABLE V.4 Absolute height changes for <i>in situ</i> coupling reaction (Δh_{LP}), coiled-coil formation (Δh_{cc}), final rinsing (Δh_{rinse}) and total layer thickness of fully build-up coiled-coil structure (Δh_{total}) on a SSM consisting of DOPC/MCCDOPE 90:10. Mean values with their standard deviations are given determined from at least 2 measurements. *) No statistic could be determined due to slow binding kinetics of E-peptides to maleimide lipids.....	69
TABLE V.5 Quantitative characterization of coiled-coil formation on DOPC/MCCDOPE 90:10 via double exponential fit (upper panel) with time constants τ_1 and τ_2 and corresponding height increases A . Off-rate k_{off} is calculated from τ determined via an exponential fit function to dissociation phase. *) DOPC/MCCDOPE 94:6 was used as SSM.....	71

TABLE VI.1 Thermodynamic constants determined from SPR: Double-exponential fit to association phase provides τ_a and k_{on} , exponential fit to dissociation phase provides k_{off} . Therefore, resulting dissociation constant K_D can be derived. 83

TABLE VI.2 Dissociation constants K_D and corresponding free enthalpies ΔG° for coiled-coil formation determined by solution sensitive methods (CD spectroscopy; first row), within hydrogels (SPR spectroscopy; second row), and at the membrane interface (ellipsometry (Langmuir isotherm); last row). *) Ellipsometry data was fitted with Bragg-Williams isotherm. . 87

TABLE VII.1 Determined diffusion coefficients D and mobile fractions F_{mob} from FRAP experiments. Lateral mobility of matrix (index *SSM*, column 2-3) was specified by adding 1 mol% BODIPY to the *SSM*, mobility of coiled-coil complex (index *cc*, column 4-5) by labeling coiled-coil forming peptide with OG488. All experiments were carried out with 10 mol% MCCDOPE present in *SSM*. 97

TABLE VII.2 Fraction of area occupied by peptide clusters on *SSM* made of fluid phase lipids (A_{POPC}) and of gel phase lipids (A_{DPPC}); for POPC bilayers, only data for LP-K3Cys, LP-*i*-K3Cys and LP-*i*-E3Cys was collected. 103

TABLE VII.3 Grain analysis for fluid and gel phase membranes. Assuming an area of 5 nm^2 for a single lipopeptide, ratio of active peptides in outer ring of cluster can be calculated ($N_{active \text{ peptides}}$). 104

Lebenslauf

Name	Gesa Pähler
Geburtsdatum und -ort	12. August 1983 in Berlin
Staatsangehörigkeit	deutsch
Familienstand	ledig
Dissertation	
März 2009 - dato	Promotionsstudium als wissenschaftliche Mitarbeiterin am Institut für Physikalische Chemie der Georg-August-Universität Göttingen; Betreuer: Prof. Dr. Andreas Janshoff
Mai 2011	Auslandsaufenthalt am IISER (<i>Indian Institute of Science Education and Research</i>) in Pune, Maharashtra, Indien, in der Arbeitsgruppe von Hosahudya N. Gopi
Studium	
Okt 2003 - Jan 2009	Studium der biomedizinischen Chemie an der Johannes-Gutenberg-Universität in Mainz
Januar 2009	Abschluss des Studiums als Diplomchemikerin
Apr 2008 - Jan 2009	Anfertigung der Diplomarbeit unter der Leitung von Prof. Dr. Andreas Janshoff am Institut für Physikalische Chemie der Johannes-Gutenberg-Universität Mainz
Apr - Aug 2007	Auslandsaufenthalt an der Cardiff University, Wales, UK, in der Arbeitsgruppe von Prof. Dr. Thomas Wirth
November 2005	Vordiplom im Fach biomedizinischer Chemie
Schule	
Juni 2003	Erlangen der allgemeinen Hochschulreife
1994 - 2003	Elly-Heuss-Knapp-Gymnasium in Heilbronn-Böckingen
1990 - 1994	Grundschule in Heilbronn-Frankenbach